Betzler, C., Eberli, G.P., Alvarez Zarikian, C.A., and the Expedition 359 Scientists
Proceedings of the International Ocean Discovery Program Volume 359
publications.iodp.org

doi:10.14379/iodp.proc.359.106.2017

Site U1468[1]

C. Betzler, G.P. Eberli, C.A. Alvarez Zarikian, M. Alonso-García, O.M. Bialik, C.L. Blättler, J.A. Guo, S. Haffen, S. Horozal, M. Inoue, L. Jovane, D. Kroon, L. Lanci, J.C. Laya, A. Ling Hui Mee, T. Lüdmann, M. Nakakuni, B.N. Nath, K. Niino, L.M. Petruny, S.D. Pratiwi, J.J.G. Reijmer, J. Reolid, A.L. Slagle, C.R. Sloss, X. Su, P.K. Swart, J.D. Wright, Z. Yao, and J.R. Young[2]

Keywords: International Ocean Discovery Program, IODP, *JOIDES Resolution*, Expedition 359, Site U1468, Maldives, Kardiva Channel, Goidhoo atoll, Indian Ocean paleoceanography, Oligocene, Miocene, Pliocene, Pleistocene, carbonate platform, carbonate platform drowning, celestine, dolomite, drift deposits, large benthic foraminifers, monsoon, sea level, sequence stratigraphy

Contents

Background and objectives

Site U1468 (proposed Site MAL-03A) is at the eastern end of the northern transect drilled in the Inner Sea of the Maldives during International Ocean Discovery Program (IODP) Expedition 359. It is located at 4°55.98′N and 73°4.28′E (Figure **F1**) at a water depth of 521.5 m, 4.8 km east of Site U1466. The site lies in the western part of the Kardiva Channel, which connects the Inner Sea of the Maldives with the Indian Ocean. Site U1468 is located approximately 6.4 km east of the edge of the youngest growth packages of the Kar-

Figure F1. Location map of Site U1468, located near the deepest and oldest gateway of the Maldives, the northeastern Kardiva Channel.

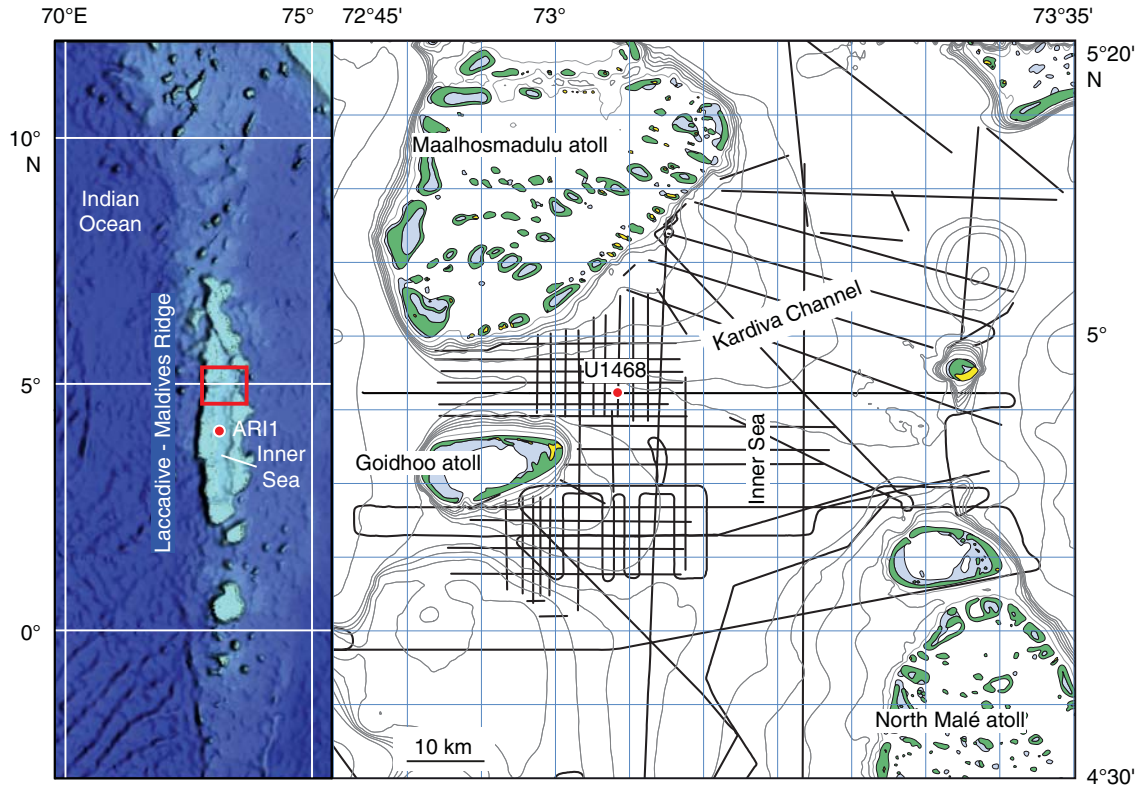

[1] Betzler, C., Eberli, G.P., Alvarez Zarikian, C.A., Alonso-García, M., Bialik, O.M., Blättler, C.L., Guo, J.A., Haffen, S., Horozal, S., Inoue, M., Jovane, L., Kroon, D., Lanci, L., Laya, J.C., Ling Hui Mee, A., Lüdmann, T., Nakakuni, M., Nath, B.N., Niino, K., Petruny, L.M., Pratiwi, S.D., Reijmer, J.J.G., Reolid, J., Slagle, A.L., Sloss, C.R., Su, X., Swart, P.K., Wright, J.D., Yao, Z., and Young, J.R., 2017. Site U1468. *In* Betzler, C., Eberli, G.P., Alvarez Zarikian, C.A., and the Expedition 359 Scientists, *Maldives Monsoon and Sea Level*. Proceedings of the International Ocean Discovery Program, 359: College Station, TX (International Ocean Discovery Program). http://dx.doi.org/10.14379/iodp.proc.359.106.2017

[2] **Expedition 359 Scientists' addresses.**

MS 359-106: Published 4 May 2017MS 3xx-2xx: Received 31 September 2012 · Accepted 31 October 2012 · Published 31 October 2012

diva platform, which is capped by a drowning unconformity (see Figure **F2** in the Site U1465 chapter [Betzler et al, 2017c]). It was chosen for three reasons. First, seismic horizon O/M (Belopolsky and Droxler, 2004), which was predicted to represent the Oligocene/Miocene boundary (Betzler et al., 2013a), is at the shallowest position in the coring area at this location. The target depth was placed below this horizon to retrieve the sedimentary record from the upper Oligocene into the lowest Miocene succession of the shallow Inner Sea. Second, Site U1468 cores contain the complete Miocene evolution of the Kardiva platform from its distal slope deposits. During the early Miocene, the marginal platforms, such as the Kardiva platform, aggraded. They then prograded in the middle Miocene and ultimately drowned. The position of Site U1468 on slightly inclined seismic lines of the distal slope records the timing of platform progradation and drowning in a basinal position. Site U1468 cores therefore have the potential to retrieve a hemipelagic sequence of sediments containing planktonic foraminifers and calcareous nannoplankton suitable for biostratigraphic analysis. Third, platform-related sediments at Site U1468 are overlain by a 426 ms two-way traveltime (TWT) thick succession of current-controlled deposits that allows for dating the age of the onset of drift related to the onset of the Indian monsoon. Drift sequence (DS) DS1 is most expanded at this location, with DS2 reduced in thickness and capped by amalgamated DS3–DS8 (Figure **F49**).

The objectives at this site were (1) to analyze the cyclostratigraphy of drift deposits, therefore providing reconstructions of changes in the current regime and monsoon cyclicity; (2) to provide a detailed reconstruction of the predrowning, drowning, and postdrowning evolution of the carbonate bank by linking the seismic stratigraphic record to the sedimentary record; (3) to constrain the timing of this evolution, thus allowing age assignments of unconformities, sedimentary interruptions, sedimentary turnovers, and onset of drift deposition; and (4) to reconstruct and date bank to drift turnover. In view of the coring results at Sites U1466 and U1467, permission was requested to deepen the hole from 532 to 1000 meters below seafloor (mbsf). With this approved request, we wanted to reach the Oligocene/Miocene boundary and to acquire cores to reconstruct environmental changes into and throughout the Neogene.

Based on the age model from Belopolsky and Droxler (2004), the base of the drift sequences is in the middle Miocene, which was verified at Site U1466. With coring at a more distal position within the drift, refinement of the onset of current-dominated deposition was expected. Likewise, the ages of the sea level–controlled platform sequences that are conformable seismic reflections below the drift sequences are embedded within the datable succession. The target was seismic horizon O/M, which was defined by Belopolsky and Droxler (2004) and traced into the northern transect by Betzler et al. (2013a, 2013b).

Operations

Transit to Site U1468

The 13.6 nmi transit from Site U1467 to Site U1468 required only 1.5 h, and by 0232 h on 7 November 2015, the ship arrived over the site coordinates and switched to the dynamic positioning system. Soon after, the rig crew began assembling the advanced piston corer (APC)/extended core barrel (XCB) bottom-hole assembly (BHA). A positioning beacon was deployed, and the drill string was lowered to the seafloor.

Hole U1468A

For Site U1468, we obtained an extension from the Environmental Protection and Safety Panel to extend the total approved penetration depth to 1000 mbsf to ensure the achievement of the site's main scientific objective of coring thorough the Oligocene/Miocene boundary. Ultimately, coring with the XCB system terminated with Core 359-U1468A-111X at a total depth of 874.7 mbsf when the biostratigraphers confirmed the Oligocene age of the recovered core (see Figure **F1** in the Expedition 359 summary chapter [Betzler et al, 2017b]).

Hole U1468A was spudded at 0830 h on 7 November 2015, establishing a seafloor depth of 521.5 m. Nonoriented APC coring continued through Core 13H to 112.6 mbsf. Coring using the half-length APC (HLAPC) followed until APC refusal on Core 38F at 225.6 mbsf. Coring with the XCB coring system continued. Hole stability was maintained throughout by circulating 20 bbl high-viscosity mud sweeps every other core. This process resulted in little or no fill on connections, normal drilling torque, and no overpull or drag with the drill string. After laying out the final core barrel, the bit was raised to 795.5 mbsf and the top drive was set back. The drill string was pulled out of the hole, clearing the seafloor at 2215 h, and the bit arrived on the rig floor at 2400 h on 11 November. Total core recovered in Hole U1468A was 458.7 m (53%). Of the 110 cores recovered, 14 were APC cores, 31 were HLAPC cores, and 65 were XCB cores (Table **T1**).

Hole U1468B

We offset the ship 20 m east of Hole U1468A and started assembling the tricone drill bit with a mechanical bit release to drill the dedicated logging hole. An extra stand of 8¼ inch drill collars was added to the existing drilling BHA to place the bit at ~130 mbsf or slightly deeper to allow the end of the pipe to extend below a potentially problematic sand package. We lowered the bit to the seafloor and started drilling without coring in Hole U1468B at 0810 h on 12 November 2015. During the course of drilling the dedicated logging hole, the driller noted elevated drilling torque and hole cleaning problems at 131.7 mbsf. At 1345 h, we spent nearly 2 h conducting a wiper trip by raising the bit to 43.5 mbsf and then running it back to the bottom of the hole. At 1530 h, drilling resumed and continued without incident until the bit reached a total depth of 874.7 mbsf at 2030 h on 12 November. We circulated a high-viscosity mud sweep, released the bit in the bottom of the hole, and at 0115 h on 13 November the end of the pipe had been positioned at 140.5 mbsf in preparation for wireline logging. We rigged up the triple combo tool string and ran it into Hole U1468B at 0240 h. The tool string reached ~835 mbsf, where it tagged bottom, indicating ~40 m of infill in the hole. A short pass logged from the bottom of the hole up to ~735 mbsf showed reasonable hole diameter. The tool string was run back to total depth, and the main pass started at 835 mbsf, recording gamma radiation, density, porosity, electrical resistivity, and magnetic susceptibility. Borehole diameter varied smoothly, ranging from ~17 to 12 inches, until a narrow section (<6 inches) was encountered at ~465 mbsf. Significant overpull was required to continue pulling the tool string up to ~290 mbsf, suggesting the borehole had deteriorated in this interval. Above ~290 mbsf, hole diameter increased, and the main pass continued up to the base of the drill pipe at 140 mbsf. Logging data were recorded continually throughout the main pass with the triple combo tool string, but further logging operations could not be carried out because of the state of the borehole. The tool string was returned to the rig floor and

rigged down, and logging operations in Hole U1468B were completed by 0915 h on 13 November. After rigging down from wireline logging, the pipe was pulled out of the hole, clearing the seafloor at 0935 h. Hole U1468B ended when the bit arrived back on the rig floor at 1125 h.

Table T1. Site U1468 core summary. DRF = drilling depth below rig floor, DSF = drilling depth below seafloor, CSF = core depth below seafloor. H = advanced piston corer, F = half-length advanced piston corer, X = extended core barrel, R = rotary core barrel, numeric core type = drilled interval. (Continued on next two pages.) **Download table in .csv format.**

Hole U1468A
Latitude: 4°55.9832′N
Longitude: 073°4.2780′E
Water depth (m): 521.5
Date started (UTC): 0345 h, 7 November 2015
Date finished (UTC): 1300 h, 10 November 2015
Time on hole (days): 3.91
Seafloor depth DRF (m): 532.5
Rig floor to sea level (m): 11
Penetration DSF (m): 874.7
Cored interval (m): 873.7
Recovered length (m): 458.7
Recovery (%): 52
Drilled interval (m): 1
Drilled interval (no.): 1
Total cores (no.): 110
APC cores (no.): 14
HLAPC cores (no.): 31
XCB cores (no.): 65

Hole U1468B
Latitude: 4°55.9823′N
Longitude: 073°4.2888′E
Water depth (m): 521.45
Date started (UTC): 1520 h, 11 November 2015
Date finished (UTC): 1520 h, 11 November 2015
Time on hole (days): 2.48
Seafloor depth DRF (m): 532.5
Rig floor to sea level (m): 11.05
Penetration DSF (m):
Cored interval (m):
Recovered length (m):
Recovery (%): 0
Drilled interval (m): 874.7
Drilled interval (no.): 1
Total cores (no.): 0

Core	Top of cored interval DSF (m)	Bottom of cored interval DSF (m)	Interval advanced (m)	Recovered length (m)	Curated length (m)	Recovery (%)	Top of recovered core CSF-A (m)	Bottom of recovered core CSF-A (m)	Date (2015)	Time UTC (h)
359-U1468A-										
1H	0.0	3.4	3.4	3.35	3.35	99	0.0	3.35	7 Nov	0345
2H	3.4	12.9	9.5	5.43	5.43	57	3.4	8.83	7 Nov	0415
3H	12.9	22.4	9.5	8.70	8.70	92	12.9	21.60	7 Nov	0445
4H	22.4	31.9	9.5	8.84	8.84	93	22.4	31.24	7 Nov	0505
5H	31.9	41.4	9.5	8.69	8.69	91	31.9	40.59	7 Nov	0525
6H	41.4	50.9	9.5	8.66	8.66	91	41.4	50.06	7 Nov	0550
7H	50.9	60.4	9.5	8.48	8.48	89	50.9	59.38	7 Nov	0615
8H	60.4	69.9	9.5	8.61	8.61	91	60.4	69.01	7 Nov	0645
9H	69.9	79.4	9.5	5.76	5.76	61	69.9	75.66	7 Nov	0720
10H	79.4	88.9	9.5	8.38	8.38	88	79.4	87.78	7 Nov	0750
11H	88.9	98.4	9.5	7.58	7.58	80	88.9	96.48	7 Nov	0825
12H	98.4	106.4	8.0	7.84	7.84	98	98.4	106.24	7 Nov	0900
13H	106.4	112.6	6.2	6.23	6.23	100	106.4	112.63	7 Nov	0945
14F	112.6	117.3	4.7	4.19	4.19	89	112.6	116.79	7 Nov	1015
15F	117.3	122.0	4.7	3.34	3.34	71	117.3	120.64	7 Nov	1040
16F	122.0	126.7	4.7	3.93	3.93	84	122.0	125.93	7 Nov	1120
17F	126.7	128.7	2.0	1.81	1.81	91	126.7	128.51	7 Nov	1140
18F	128.7	131.2	2.5	2.53	2.53	101	128.7	131.23	7 Nov	1225
19F	131.2	135.9	4.7	3.94	3.94	84	131.2	135.14	7 Nov	1255
20F	135.9	140.6	4.7	2.83	2.83	60	135.9	138.73	7 Nov	1320
21F	140.6	145.3	4.7	3.82	3.82	81	140.6	144.42	7 Nov	1440
22F	145.3	150.0	4.7	4.06	4.06	86	145.3	149.36	7 Nov	1520
23F	150.0	154.7	4.7	4.38	4.38	93	150.0	154.38	7 Nov	1540
24F	154.7	159.4	4.7	4.25	4.25	90	154.7	158.95	7 Nov	1600
25F	159.4	164.1	4.7	4.50	4.50	96	159.4	163.90	7 Nov	1620
26F	164.1	168.8	4.7	4.10	4.10	87	164.1	168.20	7 Nov	1640
27H	168.8	178.3	9.5	3.10	3.10	33	168.8	171.90	7 Nov	1720
28F	178.3	183.0	4.7	3.36	3.36	71	178.3	181.66	7 Nov	1755
29F	183.0	187.7	4.7	4.49	4.49	96	183.0	187.49	7 Nov	1815
30F	187.7	192.4	4.7	4.53	4.53	96	187.7	192.23	7 Nov	1835
31F	192.4	197.1	4.7	4.82	4.82	103	192.4	197.22	7 Nov	1910
32F	197.1	201.8	4.7	4.61	4.61	98	197.1	201.71	7 Nov	1930
33F	201.8	206.5	4.7	4.01	4.01	85	201.8	205.81	7 Nov	2005
34F	206.5	211.2	4.7	3.72	3.72	79	206.5	210.22	7 Nov	2030
35F	211.2	215.9	4.7	4.73	4.73	101	211.2	215.93	7 Nov	2110
36F	215.9	216.2	0.3	0.19	0.19	63	215.9	216.09	7 Nov	2135
37F	216.2	220.9	4.7	3.58	3.58	76	216.2	219.78	7 Nov	2210
38F	220.9	225.6	4.7	4.02	4.02	86	220.9	224.92	7 Nov	2240

Table T1 (continued). (Continued on next page.)

Core	Top of cored interval DSF (m)	Bottom of cored interval DSF (m)	Interval advanced (m)	Recovered length (m)	Curated length (m)	Recovery (%)	Top of recovered core CSF-A (m)	Bottom of recovered core CSF-A (m)	Date (2015)	Time UTC (h)
39X	225.6	233.4	7.8	3.00	3.00	38	225.6	228.60	8 Nov	0000
40X	233.4	243.1	9.7	1.81	1.81	19	233.4	235.21	8 Nov	0050
41X	243.1	252.8	9.7	0.50	0.50	5	243.1	243.60	8 Nov	0140
42X	252.8	262.5	9.7	0.22	0.22	2	252.8	253.02	8 Nov	0210
43X	262.5	272.2	9.7	2.61	2.61	27	262.5	265.11	8 Nov	0250
44X	272.2	281.9	9.7	2.70	2.70	28	272.2	274.90	8 Nov	0315
45X	281.9	291.6	9.7	1.46	1.46	15	281.9	283.36	8 Nov	0355
46F	291.6	296.4	4.8	4.33	4.33	90	291.6	295.93	8 Nov	0420
47F	296.4	301.1	4.7	4.82	4.82	103	296.4	301.22	8 Nov	0505
48F	301.1	305.8	4.7	2.14	2.14	46	301.1	303.24	8 Nov	0535
49F	305.8	310.5	4.7	4.66	4.66	99	305.8	310.46	8 Nov	0615
50F	310.5	315.2	4.7	1.23	1.23	26	310.5	311.73	8 Nov	0640
51F	315.2	319.9	4.7	4.35	4.35	93	315.2	319.55	8 Nov	0715
52F	319.9	324.6	4.7	0.35	0.35	7	319.9	320.25	8 Nov	0745
53X	324.6	330.6	6.0	5.13	5.13	86	324.6	329.73	8 Nov	0930
54X	330.6	340.3	9.7	0.66	0.66	7	330.6	331.26	8 Nov	1020
55X	340.3	345.0	4.7	2.08	2.08	44	340.3	342.38	8 Nov	1113
561	345.0	346.0		*****Drilled from 345.0 to 346.0 mbsf*****					8 Nov	1200
57X	346.0	350.0	4.0	0.15	0.15	4	346.0	346.15	8 Nov	1230
58X	350.0	359.7	9.7	2.80	2.80	29	350.0	352.80	8 Nov	1300
59X	359.7	369.5	9.8	8.57	8.57	87	359.7	368.27	8 Nov	1400
60X	369.5	379.2	9.7	0.78	0.78	8	369.5	370.28	8 Nov	1440
61X	379.2	388.9	9.7	9.81	9.81	101	379.2	389.01	8 Nov	1520
62X	388.9	398.6	9.7	0.21	0.21	2	388.9	389.11	8 Nov	1555
63X	398.6	408.3	9.7	4.65	4.65	48	398.6	403.25	8 Nov	1645
64X	408.3	418.0	9.7	3.74	3.74	39	408.3	412.04	8 Nov	1800
65X	418.0	427.7	9.7	1.53	1.53	16	418.0	419.53	8 Nov	1855
66X	427.7	437.5	9.8	1.30	1.30	13	427.7	429.00	8 Nov	1955
67X	437.5	447.2	9.7	9.82	9.82	101	437.5	447.32	8 Nov	2050
68X	447.2	456.9	9.7	4.68	4.68	48	447.2	451.88	8 Nov	2135
69X	456.9	466.6	9.7	9.71	9.71	100	456.9	466.61	8 Nov	2230
70X	466.6	476.3	9.7	8.24	8.24	85	466.6	474.84	8 Nov	2325
71X	476.3	486.0	9.7	2.44	2.44	25	476.3	478.74	9 Nov	0015
72X	486.0	495.7	9.7	1.09	1.09	11	486.0	487.09	9 Nov	0100
73X	495.7	505.5	9.8	10.07	10.07	103	495.7	505.77	9 Nov	0150
74X	505.5	515.2	9.7	6.64	6.64	68	505.5	512.14	9 Nov	0230
75X	515.2	524.9	9.7	10.04	10.04	104	515.2	525.24	9 Nov	0315
76X	524.9	534.6	9.7	10.03	10.03	103	524.9	534.93	9 Nov	0400
77X	534.6	544.3	9.7	0.63	0.63	6	534.6	535.23	9 Nov	0445
78X	544.3	554.0	9.7	6.90	6.90	71	544.3	551.20	9 Nov	0530
79X	554.0	563.7	9.7	7.59	7.59	78	554.0	561.59	9 Nov	0615
80X	563.7	573.4	9.7	2.54	2.54	26	563.7	566.24	9 Nov	0655
81X	573.4	583.1	9.7	6.60	6.60	68	573.4	580.00	9 Nov	0745
82X	583.1	592.8	9.7	7.00	7.00	72	583.1	590.10	9 Nov	0825
83X	592.8	602.5	9.7	2.44	2.44	25	592.8	595.24	9 Nov	0910
84X	602.5	612.2	9.7	6.28	6.28	65	602.5	608.78	9 Nov	0950
85X	612.2	621.9	9.7	2.28	2.28	24	612.2	614.48	9 Nov	1035
86X	621.9	631.6	9.7	2.76	2.76	28	621.9	624.66	9 Nov	1120
87X	631.6	641.3	9.7	0.76	0.76	8	631.6	632.36	9 Nov	1205
88X	641.3	651.0	9.7	3.52	3.52	36	641.3	644.82	9 Nov	1300
89X	651.0	660.7	9.7	3.90	3.90	40	651.0	654.90	9 Nov	1350
90X	660.7	670.4	9.7	0.54	0.54	6	660.7	661.24	9 Nov	1435
91X	670.4	680.1	9.7	0.59	0.59	6	670.4	670.99	9 Nov	1530
92X	680.1	689.8	9.7	1.85	1.85	19	680.1	681.95	9 Nov	1625
93X	689.8	699.5	9.7	5.21	5.21	54	689.8	695.01	9 Nov	1720
94X	699.5	709.2	9.7	2.92	2.92	30	699.5	702.42	9 Nov	1805
95X	709.2	718.9	9.7	2.20	2.20	23	709.2	711.40	9 Nov	1855
96X	718.9	728.6	9.7	5.72	5.72	59	718.9	724.62	9 Nov	1955
97X	728.6	738.3	9.7	3.36	3.36	35	728.6	731.96	9 Nov	2110
98X	738.3	748.0	9.7	2.96	2.96	31	738.3	741.26	9 Nov	2200
99X	748.0	757.7	9.7	3.17	3.17	33	748.0	751.17	10 Nov	0010
100X	757.7	767.4	9.7	2.67	2.67	28	757.7	760.37	10 Nov	0110
101X	767.4	777.1	9.7	2.34	2.34	24	767.4	769.74	10 Nov	0210
102X	777.1	786.8	9.7	2.47	2.47	25	777.1	779.57	10 Nov	0305
103X	786.8	796.5	9.7	4.59	4.59	47	786.8	791.39	10 Nov	0405
104X	796.5	806.2	9.7	4.02	4.02	41	796.5	800.52	10 Nov	0500
105X	806.2	815.9	9.7	9.32	9.32	96	806.2	815.52	10 Nov	0555

Table T1 (continued).

Core	Top of cored interval DSF (m)	Bottom of cored interval DSF (m)	Interval advanced (m)	Recovered length (m)	Curated length (m)	Recovery (%)	Top of recovered core CSF-A (m)	Bottom of recovered core CSF-A (m)	Date (2015)	Time UTC (h)
106X	815.9	825.6	9.7	4.50	4.50	46	815.9	820.40	10 Nov	0655
107X	825.6	835.3	9.7	1.80	1.80	19	825.6	827.40	10 Nov	0810
108X	835.3	845.0	9.7	5.42	5.42	56	835.3	840.72	10 Nov	0930
109X	845.0	854.7	9.7	2.02	2.02	21	845.0	847.02	10 Nov	1030
110X	854.7	865.0	10.3	0.07	0.07	1	854.7	854.77	10 Nov	1135
111X	865.0	874.7	9.7	0.02	0.02	0	865.0	865.02	10 Nov	1300
	Hole U1468A totals:		874.7	458.70	458.70					
359-U1468B-11	0.0	874.7	*****Drilled from 0.0 to 874.7 mbsf*****						11 Nov	1520

Lithostratigraphy

Site U1468 was drilled through a series of drift deposits into the distal bottomsets of the Miocene Kardiva platform and bottomed out in an Oligocene shallow-water platform, as shown on seismic profiles (Figure **F2**). The scientific objectives at this site were to analyze the cyclostratigraphy of drift deposits by providing reconstructions of changes in the current regime and monsoon cyclicity and to constrain the timing of unconformities and sedimentary interruptions. One hole was cored at this site, and eight lithostratigraphic units were identified (Figure **F3**). The drift package at Site U1468 comprises Units I–IV, and the distal slope of the Miocene Kardiva platform consists of Unit V. Lithologies of a restricted basin environment define Unit VI, and those of a shallow-water basin environment are grouped into Unit VII. The last unit, Unit VIII, is the Oligocene shallow-water platform.

Lithostratigraphic units

Unit I

Interval: 359-U1468A-1H-1, 0 cm, to 6H-3, 126 cm
Depth: 0–45.67 mbsf

Unit I consists of unlithified to partially lithified light brownish gray to light gray and pale yellow/white packstone to grainstone (Figure **F4A**) and two thin unlithified wackestone intervals no thicker than 55 cm between 17.4–17.95 and 22.72–23.2 mbsf. The main components of Unit I are abundant planktonic foraminifers; benthic foraminifers; pteropods, *Halimeda* plates, and mollusk fragments; echinoid fragments and spines; otoliths; fish remains; and very rare bryozoans. In general, bioclasts are well preserved. Aggregate grains, organic matter, yellow- to brown-stained lithoclasts, and bioclasts occur throughout the entire unit. The fine fraction contains aragonite needles (<5 µm), calcite crystals (5–10 µm), and calcareous nannofossils (coccoliths). Carbonate texture varies between wackestone, packstone, and grainstone between 17.4 mbsf and the lower unit boundary at 45.67 mbsf, with interbedding thicknesses ranging from centimeters to meters.

Unit II

Interval: 359-U1468A-6H-3, 126 cm, to 30F, 0 cm
Depth: 45.67–192.46 mbsf

The boundary between lithostratigraphic Units I and II is placed at the top of an interval with abundant large benthic foraminifers at 45.67 mbsf (Figure **F4B**). The texture in Unit II varies from grainstone and rudstone at the top of the unit to mudstone and packstone at the base. Bioclasts within this unit are abraded and overgrown with calcite crystals (Figure **F5**). The 146.79 m thick Unit II contains intercalations of fining- and coarsening-upward intervals that allow the definition of three subunits. Subunit IIA has a coarsening-upward trend from 125.93 to 45.67 mbsf; Subunit IIB coarsens upward from 149.36 to 126.7 mbsf; Subunit IIC fines upward from 192.18 to 178.3 mbsf, followed by a coarsening-upward trend from 178.3 to 150 mbsf. The matrix throughout the entire unit contains abundant calcite crystals and very rare dolomite rhombs and calcareous nannofossils. Throughout this unit, large benthic foraminifers decrease in size downcore from 3 mm at the top to <1 mm at the boundary with Unit III.

Subunit IIA

Interval: 359-U1468A-6H-3, 126 cm, through 16F-CC
Depth: 45.67–126.7 mbsf

From 45.67 to 87.78 mbsf, Subunit IIA is dominated by a massive coarse- to granular-grained rudstone succession, occasionally intercalated by thin intervals of fine- to coarse-grained wackestone, packstone, and grainstone that range in thickness from 1 to 50 cm.

The packstone texture is also present as burrow infill, which also contains organic matter. The subunit consists of a granule-grained rudstone for the upper 60 m and is characterized by coarsening-upward fine- to granule-grained large benthic foraminiferal sand within the bottom 20 m. The main components of this unit are large benthic foraminifers (*Amphistegina* sp., *Lepidocyclina* sp., *Miogypsinoides* sp., *Heterostegina* sp., *Operculina* sp., and *Sphaerogypsina globulus*). Echinoid spines, red algae, mollusk fragments, branching and encrusting bryozoans, *Halimeda* plates, and aggregate grains are also present. A few dolomite rhombs are found in smear slides. Dogtooth, syntaxial overgrowth, and granular calcite cement are present around most of the bioclasts (Figure **F6**).

Subunit IIB

Interval: 359-U1468A-17F-1, 0 cm, through 22F-CC
Depth: 126.7–150 mbsf

The major characteristic of Subunit IIB is the cyclic fining-upward successions with sharp basal contacts and grading from fine-grained packstone to medium-grained grainstone between 131.2 and 150 mbsf (Figure **F7**). The main large benthic foraminifers are *S. globulus*, *Lepidocyclina* sp., and *Amphistegina* sp. Echinoid spines, red algae, mollusk fragments, branching and encrusting bryozoans, and aggregate grains are common. This subunit also marks the start of the downhole size reduction of large benthic foraminifers from

Figure F2. Seismic Line P65 with location and final penetration depths at Sites U1465, U1466, and U1468. A high-amplitude reflection marks the Oligocene/Miocene (O/M) boundary (Belopolsky and Droxler, 2004; Betzler et al., 2013b). The overlying flat reflections image the deposits of the early Inner Sea; the higher, slightly inclined reflections are the distal lobes of the prograding Kardiva platform to the west. Reflections above the green seismic horizon are current-controlled drift deposits with a moat between Sites U1465 and U1466. The mounded drift is capped by a sheeted drift package that reaches the seafloor. CDP = common depth point.

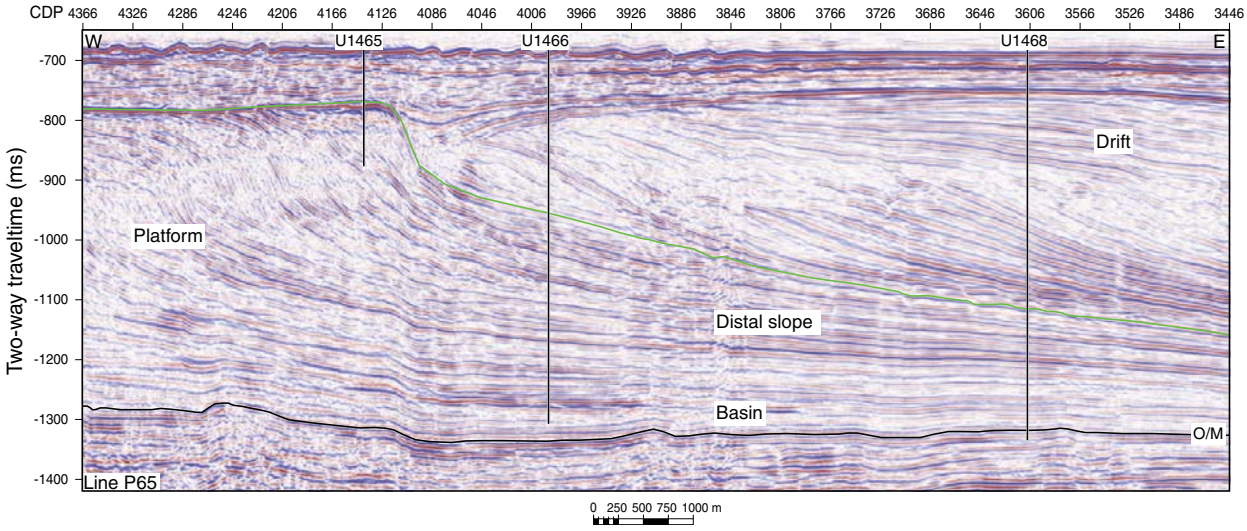

interval 23F-1, 0 cm, at 150 mbsf to 192.46 mbsf. Within the matrix, a few dolomite rhombs are observed.

Subunit IIC

Interval: 359-U1468A-22F-CC, to 31F-1, 6 cm
Depth: 150–192.46 mbsf

Subunit IIC is characterized by two contrasting grain size trends:

1. An overall coarsening-upward trend from 150 to 178.5 mbsf that ends with a granular-grained rudstone at the top of the unit, and
2. A distinctive overall fining-upward trend from medium- to fine-grained packstone from 178.5 to 190.6 mbsf.

The main components are large benthic foraminifers (*S. globulus*, *Lepidocyclina* sp., *Amphistegina* sp., *Operculina* sp., *Cycloclypeus annulatus*, *Miogypsinoides* sp., and *Heterostegina* sp.) with common echinoid spines, mollusk fragments, bryozoans, and minor *Halimeda* plates and red algae. Some bioclasts are coated by a dense micritic crust, probably of microbial origin. Bioclasts locally show fragmentation and contain various cements, including dogtooth and granular calcite that fill intraparticle pore spaces. Dolomite rhombs occur adjacent to calcite crystals. The top of this subunit lacks dolomite rhombs in smear slides, but small amounts are observed at 170.38 mbsf. Dolomite rhombs eventually increase to a common appearance within the matrix at 191.62 mbsf.

Unit III

Interval: 359-U1468A-31F-1, 6 cm, through 47F-CC
Depth: 192.46–296.4 mbsf

Unit III is a very fine- to medium-grained wackestone package with two packstone to rudstone intervals up to 5 m thick at 192.46–197.22 and 215.95–216.28 mbsf and two mudstone intervals at 217.7–219.68 and 223.43–223.57 mbsf. Colors include light brownish gray to light gray, pale yellow, and white, irrespective of carbonate texture. In this unit, planktonic foraminifers reappear and large benthic foraminifers are absent. Most bioclasts are heavily overgrown with dogtooth calcite crystals. The matrix contains abundant calcite crystals (Figure **F8A**). Sponge spicules are rare and appear mostly as aggregate grains and/or intraclasts (Figure **F8B**). Calcareous nannofossils (coccoliths) are extremely rare to absent (see **Biostratigraphy**). Dolomite rhombs and aragonite needles occur at different depths within the unit. Dolomite decreases from 199.82 to 233.95 mbsf but increases at 262.72 mbsf to the base of the unit. In contrast, aragonite needles increase from 199.82 to 214.76 mbsf and decrease at 262.72 mbsf to the base of the unit. Organic matter is common, especially in burrow infills.

Unit IV

Interval: 359-U1468A-48F-1, 0 cm, through 65X-CC
Depth: 296.4–427.7 mbsf

Unit IV consists of lithified packstone intercalated with three wackestone packages up to 3 m thick (301.1–303.24, 327.45–328.62, and 369.5–370.22 mbsf). The upper unit boundary is marked by a change in degree of lithification into a more competent layer without color or grain size change. Components include bioclasts and planktonic and benthic foraminifers severely overgrown by sparry calcite. Bioclastic components sometimes display oriented flattening and wispy seams resulting from burial compaction (Figure **F9**). The degree of bioturbation in this unit allows identification of several ichnotaxa, including *Thalassinoides*, *Palaeophycus*, *Planolites*, and *Chondrites*. Occasionally, chert nodules occur (Figure **F10**). Smear slide analyses of the fine fraction show an abundance of calcite crystals and dolomite rhombs, common sponge spicules, calcareous nannofossils and glauconite, and few aragonite needles.

Unit V

Interval: 359-U1468A-66X-1, 0 cm, through 96X-CC
Depth: 427.7–728.6 mbsf

Figure F3. Lithostratigraphic summary, Site U1468.

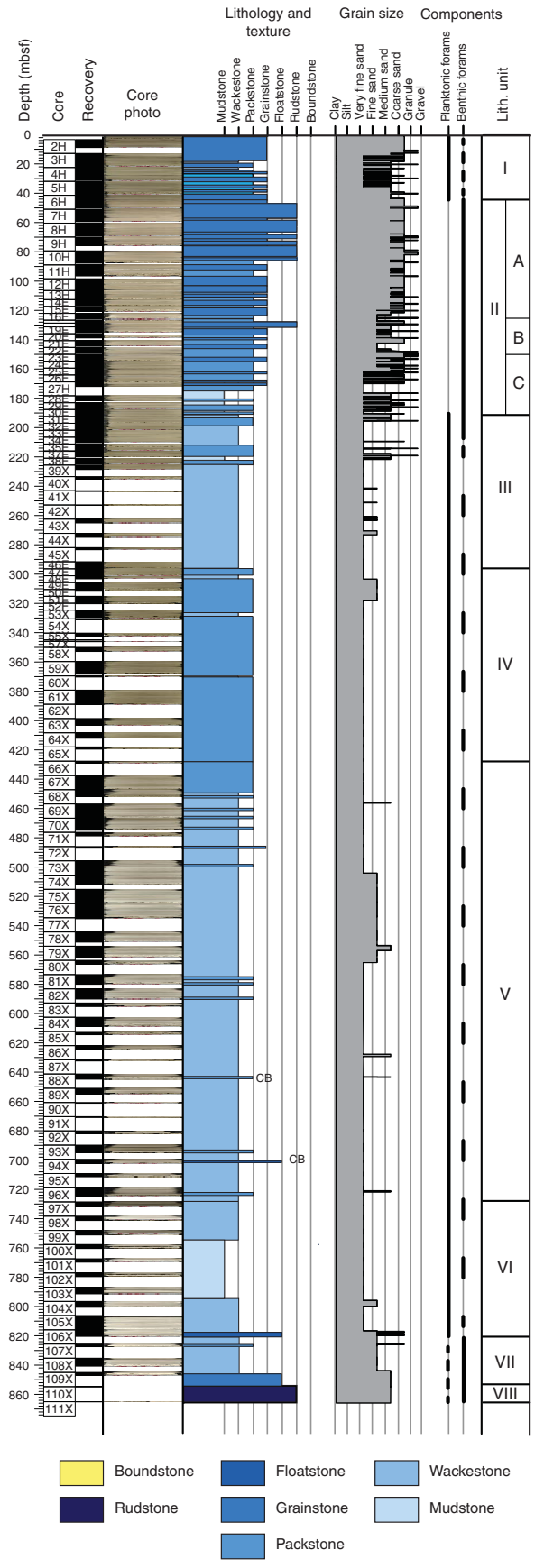

Figure F4. Units I and II, Hole U1468A. A. Centimeter-thick layer with a packstone texture (arrows) within the unlithified grainstone, Unit I (4H-5A, 100–130 cm). B. Contact between unlithified grainstone and unlithified rudstone (arrow) is the Unit I/II boundary (6H-3A, 110–140 cm).

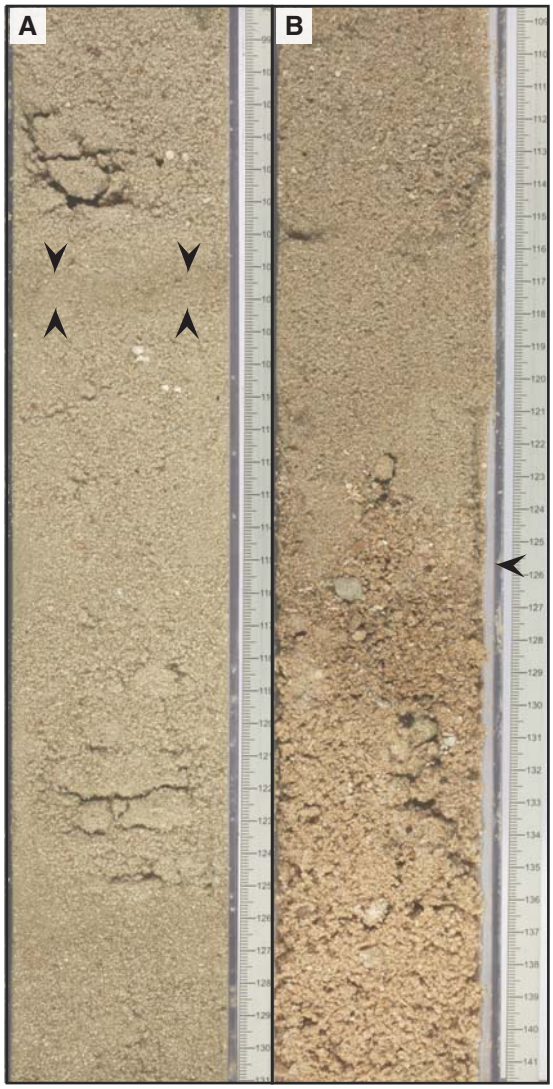

Unit V is characterized by lithified wackestone intercalated with packstone intervals <2 m thick with large benthic foraminifers, for example, from 427.7 to 448.59 mbsf. Throughout the unit, light and dark intervals alternate. The upper boundary of Unit V is placed at the uppermost white layer observed in the cores (Figure **F11**). Thirty-eight light-dark couplet intervals were counted. The light portion thickens from less than 1 m to 15 m downhole, whereas the thickness of the dark layers is never more than 5 m. The dark intervals contain abundant organic material and apatite. The color of the dark intervals changes gradationally from light olive-gray at the top of the unit to dark grayish brown at the bottom. The colors of the light intervals range from pale yellow to white throughout the unit, as they lack organic material and contain microcrystalline spar that welds the components together.

The main components in this unit are planktonic foraminifers, benthic foraminifers, and mollusk fragments, and bioclast fragments are common. Most components are overgrown by sparry calcite, and original aragonite tests are no longer preserved. Well-

Figure F5. Sieved residue (>250 µm) showing the degree of preservation of Unit I and II components, Hole U1468A. A. Pristine preservation of Unit I skeletal components including planktonic foraminifers, benthic foraminifers, and pteropod fragments (1H-CC). Nonskeletal components are stained lithoclasts and organic material. B. Unit II large benthic foraminifers and aggregate grains (arrow) overgrown with calcite (14F-2).

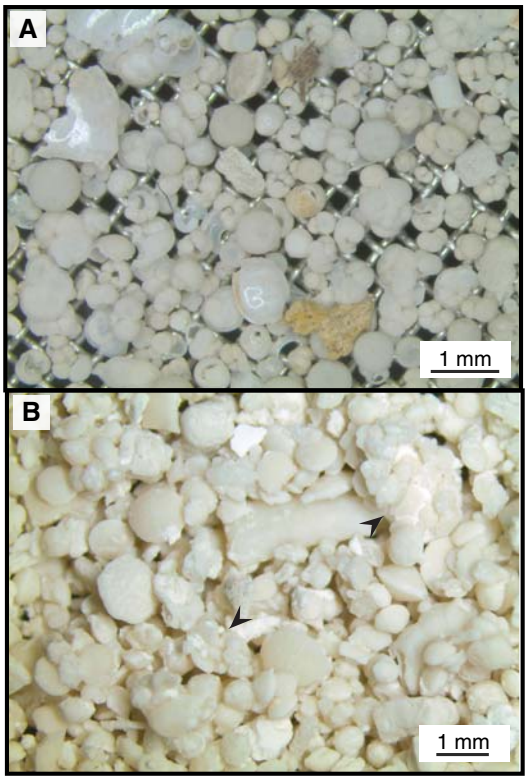

preserved ichnotaxa within this unit include *Thalassinoides*, *Teichichnus*, *Asterosoma*, *Phycosiphon*, *Zoophycos*, *Palaeophycus*, *Planolites*, and *Chondrites*. Bioturbation is pervasive, and often several generations of burrowing are observed that are occasionally infilled with glauconite or pyrite crystals. The matrix from smear slide analyses shows an abundance of calcareous nannofossils, aragonite needles, and microcrystalline calcite.

Two completely dolomitized intervals occur in this unit. The first is in Core 72X between 486 and 487.09 mbsf, where the few recovered rocks consist of dolomitized grainstone. Samples from the second interval (Core 77X; 534.6–535.23 mbsf) consist of completely dolomitized wackestone. Two convoluted beds were found in this unit at 88X-1, 0–46 cm (641.3–641.76 mbsf), and 94X-1, 72–106 cm (700.22–700.56 mbsf).

Unit VI

Interval: 359-U1468A-97X-1, 0 cm, to 106X-2, 15 cm
Depth: 728.6–817.55 mbsf

Unit VI consists of lithified wackestone to packstone. The upper unit boundary is placed at a distinctive color change in the darker intervals, from dark grayish brown in Unit V to black in Unit VI at 728.6 mbsf (Figure **F12**). A total of 41 black-white couplets are found in this unit. Dark intervals range in thickness from 1 to 25 cm. Very fine laminations are visible in well-preserved sections. The dark intervals include abundant organic matter and small ichnotaxa such as *Chondrites*, *Planolites*, and *Phycosiphon* (Figure **F13A**).

Figure F6. *Amphistegina* sp. grainstone (359-U1468A-7H-2, 48–50 cm): 1 = *Amphistegina* sp., 2 = red algal debris. Fossils and clasts are cemented together by sparry cements. A. Plane-polarized light [PPL]. B. Cross-polarized light [XPL].

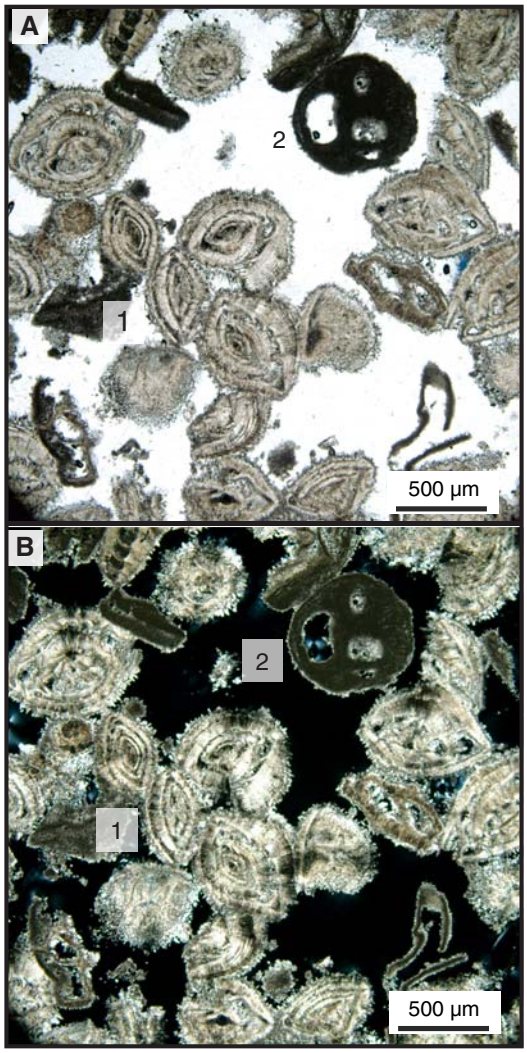

Light intervals have a restricted color range from pale gray to white. The light intervals in this subunit are generally less than 2 m thick and contain large ichnotaxa such as *Teichichnus*, *Zoophycos*, and *Asterosoma* (Figure **F13B**). Occasionally, pyrite and organic matter are present within the burrows (Figure **F14A**). Planktonic foraminifers are abundant, and benthic foraminifers are present. The matrix contains numerous calcareous nannofossils (Figure **F14B**) and calcite crystals. Dolomite rhombs are rare.

Unit VII

Interval: 359-U1468A-106X-2, 15 cm, through 109X-CC
Depth: 817.55–854.7 mbsf

This unit comprises medium-grained wackestone (Figure **F15A–F15C**) with coarse- to very coarse grained floatstone intervals that mark the top and bottom of the unit at 817.55–820.4 and 845–847.02 mbsf and a very coarse grained packstone interval in the middle from 825.9 to 827.4 mbsf. The Unit VII boundary marks the reappearance of large benthic foraminifers that are mostly frag-

Figure F7. Unit II, Hole U1468A. A. Fining-upward layers from very coarse grained rudstone to fine-grained packstone with an erosional surface at each layer (17F-1, 47–68 cm). The top of this section is the Subunit IIA/IIB boundary. B. Close-up of very coarse grained rudstone (17F-1, 56–65 cm; red line in A) showing large components (≈1 cm) such as rip-up clasts (arrow), large benthic foraminifers, echinoid spines, and extraclasts.

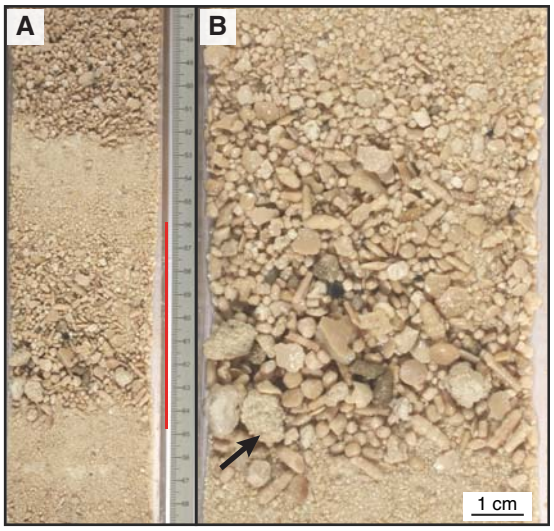

Figure F8. Unit III, Hole U1468A. A. Planktonic foraminifer heavily overgrown with calcite crystals (33F-1, 46 cm). B. Clast dominated by sponge commonly found spicules (37F-2A).

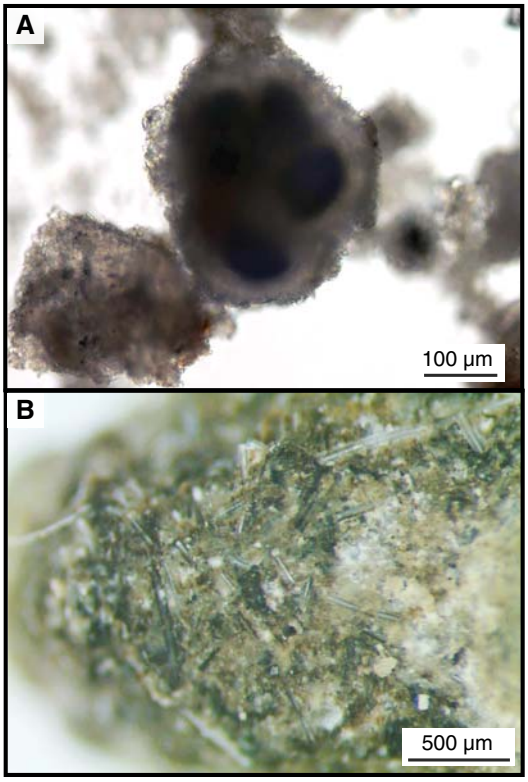

mented, sometimes with glauconite precipitate (Figure **F14C**), and occur with yellow-stained lithoclasts and bioclasts. Floatstone and packstone intervals are usually made up of large benthic foraminifers (Figure **F15D–F15F**) such as *Nummulites* sp., *Amphistegina* sp., *Lepidocyclina* sp., *Cycloclypeus* sp., and *Miogypsina* sp. and occur with planktonic foraminifers and red algae (Figure **F16**). Skeletal components are held together by a micritic matrix, whereas intraparticle pores are mainly filled with microcrystalline spar. Ichnotaxa include *Planolites* and *Phycosiphon*, both of which are usually preserved in very fine to fine-grained wackestone. Some burrows have glauconite and pyrite infill.

Figure F9. A. Wispy seams of organic material (arrow) from burial compaction (359-U1468A-54X-1, 4–7 cm). B. Close-up of A.

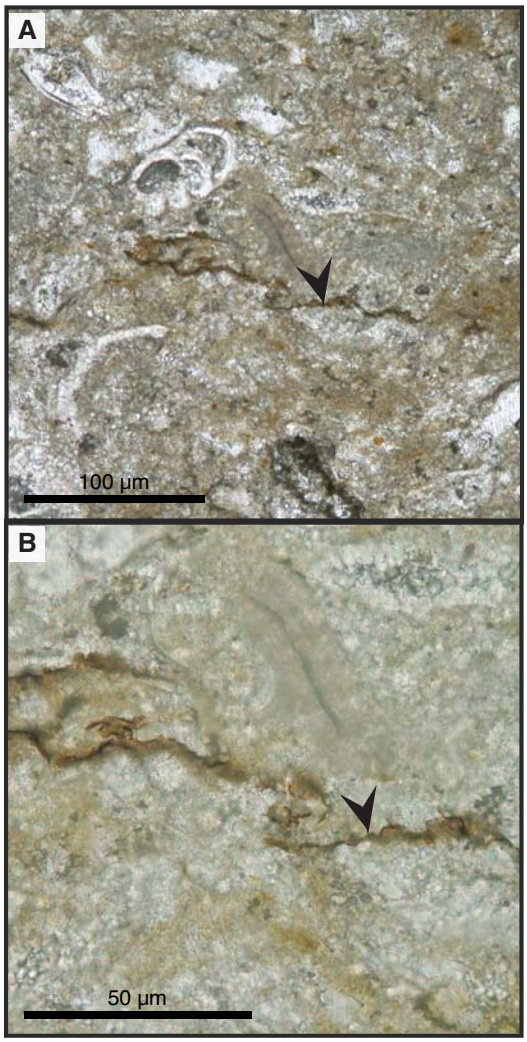

Unit VIII

Interval: 359-U1468A-110X-1, 0 cm, to 111X-1, 2 cm
Depth: 854.7–865.02 mbsf

Unit VIII is limestone characterized by the appearance of reef biota. Two different rock textures were observed:

1. Fine- to medium-grained light brownish gray rudstone that contains large coral fragments and small and large benthic foraminifers. Small benthic foraminifers are miliolids, and large benthic foraminifers comprise *Operculina* sp., *Amphistegina* sp., *Heterostegina* sp., *Lepidocyclina* sp., and *Alveolina* sp.

Figure F10. Chert nodules, Hole U1468A. A. Chert nodule (arrow) in lithified packstone from Unit III (47F-1, 58–68 cm). B. Chert nodule (arrow) with silicified burrows from Unit IV (59X-1, 90–110 cm).

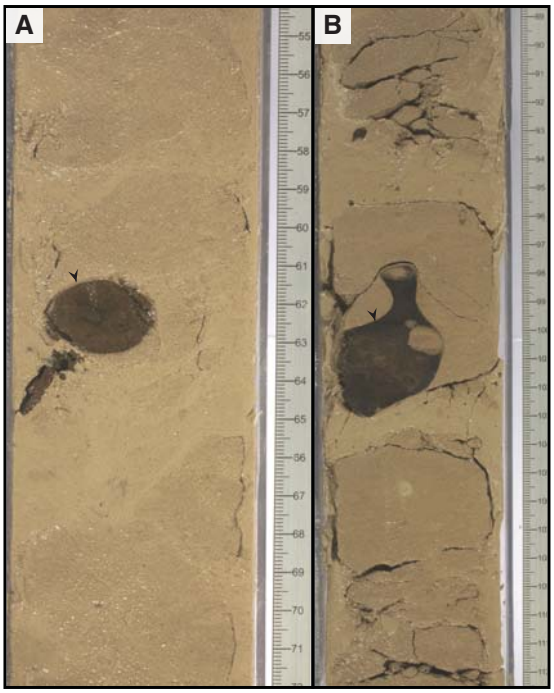

2. Medium-grained pale yellow floatstone consisting of fragmented large benthic foraminifers such as *Heterostegina* sp. and *Amphistegina* sp. and common *Halimeda* plates, bivalve fragments, coral fragments, bryozoan fragments, red algae, echinoid fragments, and echinoid spines in a packstone matrix.

One red algae retained its original hooked structure (Figure **F17**). Occasionally, pyrite and glauconite are found within the chambers of the foraminifers. Planktonic foraminifers were not observed within the light brownish gray rock from 854.7 to 865 mbsf but are present below 865 mbsf within the pale yellow rock. A few molds have geopetal infill (Figure **F18**). Other components are preserved as molds or are micritized. Moldic pores are infilled with dogtooth or blocky calcite crystals (Figure **F19**). Small burrows are filled with pellets cemented with drusy cements (Figure **F20**).

Discussion

The Site U1468 lithostratigraphy clearly reflects the sedimentological evolution of the Kardiva platform and drift as shown on seismic sections (see **Seismic stratigraphy**). Unit I represents the youngest of the unconsolidated drift deposits (Lüdmann et al., 2013) and consists of a mixture of pelagic and neritic components and a basinal (background) sediment input dominated by pteropods, otoliths, and planktonic foraminifers. The presence of currents is indicated by the occurrence of yellow- to brown-stained grains from reworking of sediments by bottom currents and by the lack of fine sediments that was removed by currents.

The Unit I/II boundary is defined by a sharp contact (Figure **F4**) that separates the above-mentioned sediments from Unit II sediments, which consist of large benthic foraminiferal rudstones. Unit II has a general coarsening-upward trend, indicating that current

Figure F11. L* and NGR values at the transition from Unit IV (359-U1468A-63X-1) to Unit V (67X-1). Core photos show distinct color change downhole to brighter tones, quantified by a shift to higher L* values (gray/black line) and a redder hue (a*) (brown/red line). This change coincides with an increase in both total NGR and the amplitude of NGR counts.

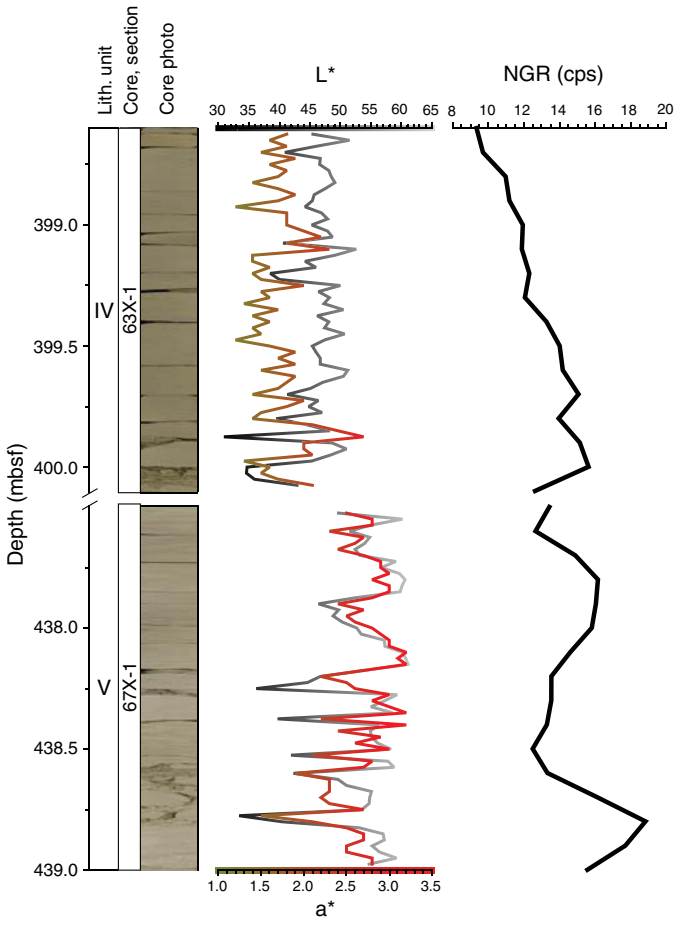

strength increased through the deposition of the unit and/or productivity of large benthic foraminifers increased. Current velocities through the Kardiva Channel could vary for two reasons: sea level fluctuations or monsoonal changes. In the narrow Kardiva Channel, a lower sea level could result in stronger current velocities causing an increase in erosion in the channel and the winnowing of fines. A wide channel during sea level highstands would result in lower current velocities allowing for the deposition of fine-grained components. The variability of grain sizes in this drift package supports the interpretation that Unit II drift deposits were associated with contourite fans (Betzler et al., 2015). Distinct changes in grain sizes in Unit II show variability in current strength that could be induced by seasonal monsoonal changes and intensities (Betzler et al., 2009; Lüdmann et al., 2013). The increase in size of large benthic foraminifers is also an indicator that the environment was becoming shallower (Renema and Troelstra, 2001). The lack of nannofossils and planktonic foraminifers further supports the scenario of fairly strong currents, strong winnowing, and a fairly shallow environment.

Units III and IV are defined by planktonic foraminifers and fine-grained, well-sorted sediments. The currents sweeping across the

Figure F12. L* and NGR values at the transition from Unit V (359-U1468A-96X-1 through 96X-3) to Unit VI (97X-1 through 97X-2). Core photos show distinct color change from brighter and relatively uniform tones to generally darker tones with distinct brighter horizons. This transition corresponds to a shift to lower values of L* and an increase in the L* amplitude between darker and brighter layers (~20% in Unit V; up to ~50% in Unit VI). Gap between 96X-3 and 97X-1 is the Unit V/VI boundary. A. Unit V bioturbated light interval with low NGR values <30 counts/s. B. Unit VI bioturbated dark interval with high NGR values >30 counts/s.

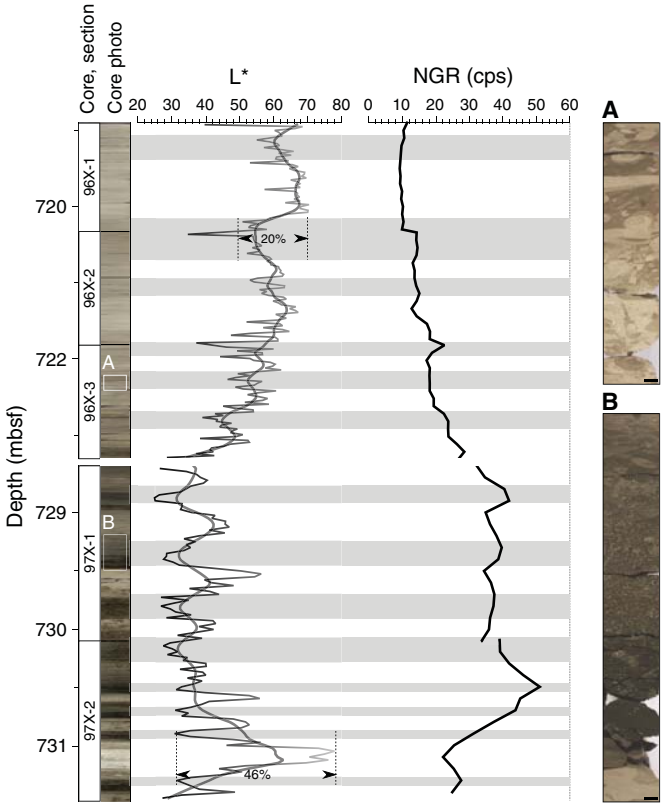

Figure F13. Examples of burrows in a black and white layer alternation from Unit VI, Hole U1468A. A. Black interval. 1 = small *Chondrites* burrow (97X-1, 68–84 cm). B. White interval with larger burrows (105X-1, 18–31 cm): 2 = *Zoophycos*, 3 = *Teichichnus*, 4 = *Thalassinoides*.

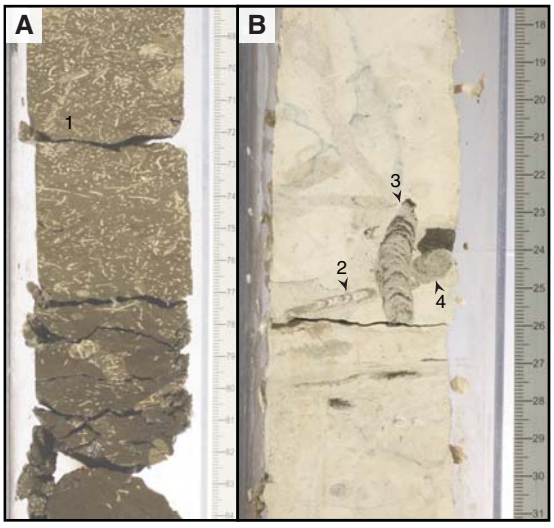

Figure F14. Lithostratigraphic Units VI and VII, Hole U1468A. A. Pyrite crystals (75X-1, 57–59 cm). B. Sediment matrix showing the abundance of calcareous nannofossils (98X-2). C. Benthic foraminifers with glauconite fill in chambers (109X-CC, 2 cm).

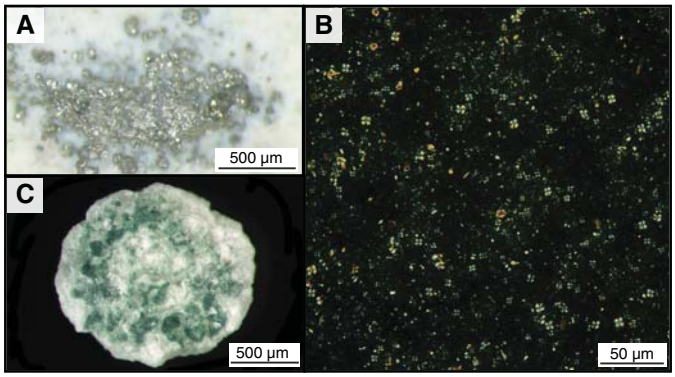

former Kardiva platform were strong enough to transport fine-grained sediments deeper into the receiving basin. The thick sediment packages of Units III and IV indicate that sedimentation rates increased significantly compared to the underlying deposits (see **Biostratigraphy**). The transported sediments quickly filled the accommodation space at the former distal slope. In the later developmental stage of this unit, the water depth was probably shallow enough to allow the establishment of a large benthic foraminiferal carbonate factory.

Unit V's upper boundary is marked by dark and light intervals interpreted as the distal slope of the prograding Kardiva platform. The convolute bedding observed at the distal slope is interpreted as slumps (731.61–731.97 and 750.87–752.19 mbsf) and could be the lateral equivalent of the slump deposits at Site U1466. Completely dolomitized grainstone and wackestone (Cores 72X and 77X) coincide with high-amplitude reflections on the seismic sections (see **Seismic stratigraphy**) that record complete sea level cycles, each with high- and low-amplitude reflections. Weak-amplitude reflection packages are interpreted as sea level highstands, and strong-amplitude reflection packages are interpreted as sea level lowstands (Belopolsky and Droxler, 2004).

Variations in seafloor oxygenation levels associated with fluctuations in productivity most likely controlled variations in benthic faunal assemblages and bioturbation patterns, preservation of organic matter, and the absence of platform-derived fine-grained sediments for Units V and VI. Darker intervals represent periods of higher productivity resulting in a low-oxygen depositional environment. Similar changes in oxygenation of the water column were previously identified by Boersma et al. (1990) at Ocean Drilling Program (ODP) Leg 115 Site 714 in the north central Indian Ocean. At ODP Site 715, dark intervals were characterized by the presence of bolivinids, which characterize oxygen minima (Douglas and Heitman, 1979; Poag and Low, 1985). This description is also consistent with results described in **Biostratigraphy**.

Unit VII sediments were deposited in a shallow-water basin in which a mixture of large benthic foraminifers and fine-grained sediments were deposited. However, the large benthic foraminifers are mostly fragmented and occur together with yellow-stained lithoclasts that suggest reworking of material or transport from a platform top. Based on seismic stratigraphy (see **Seismic stratigraphy**), an Oligocene–Miocene platform existed at the western margin of the Maldives platform at that time, and offbank transport could

Figure F15. A. Section 359-U1468A-107X-1, 50–90 cm. B–F. Various stages across the transition from fine-grained wackestone (top) to coarse-grained packstone (bottom). Background matrix: 1 = large benthic foraminifers, 2 = burrow intermixing with finer grained material.

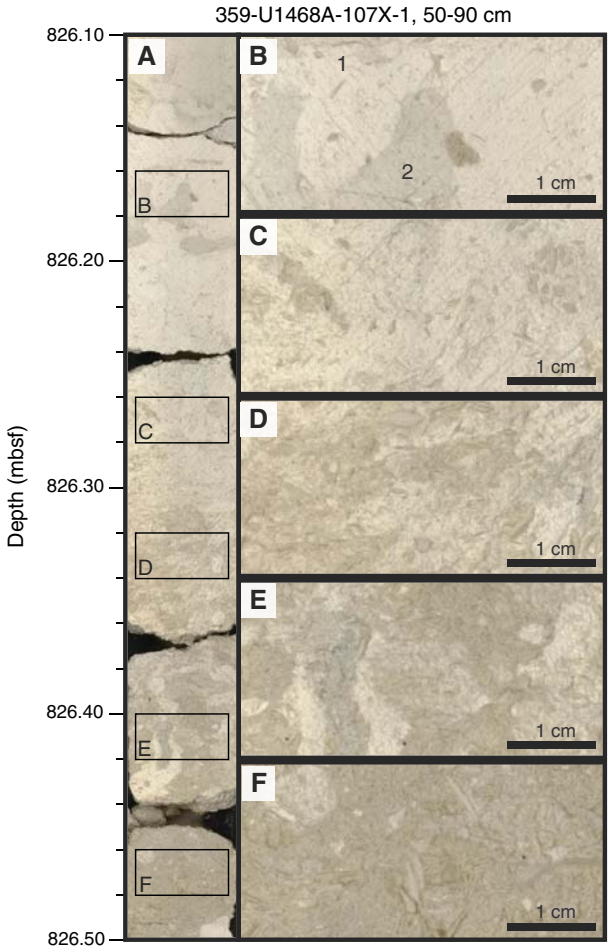

have brought material from the platform into the adjacent shallow basin.

The Unit VII/VIII boundary was placed at the top of the Oligocene shallow-water platform. At the time, the shallow-water platform at Site U1468 most likely was a protected lagoon where the growth of seagrass was possible. This interpretation is based on the presence of hooked shapes in the red algae (Figure F17). These shapes are a result of epiphytic growth over seagrass leaves and stems (Sola et al., 2013). The shift from a shallow-water platform to a shallow-water basin represents a sea level rise that forced the shallow-water platform to reduce in size, aggrade, and eventually give way to deeper water deposits, ultimately forming the Inner Sea "bucket." This shift could explain the deposition of very fine grained Unit VI and VII sediments within this restricted depositional environment (Belopolsky and Droxler, 2004; Lüdmann et al., 2013).

In summary, an Oligocene shallow-water platform (Unit VIII) recovered at the base was subjected to a marine transgression. The fast marginal aggradation of the platform produced a bucket that allowed fine sediments to accumulate in a shallow-water basin setting with the deposition of large benthic foraminiferal sediments (Unit VII). The shallow-water basin then evolved into a basin setting in which nannofossil chalk and black organic-rich sediments were deposited (Unit VI). Ultimately, the western portion of the carbonate platform caught up with the relative sea level rise and prograded into the Inner Sea as indicated by the deposition of distal slope sediments and the white-dark brownish gray–olive gray alternating intervals (Unit V). The transition to current-dominated sedimentation coincides with the drowning of the Kardiva platform. The very high sedimentation rates of the drift sediments (Units IV and III) that fill the deep basin next to the former platform also indicate that prolific sediment production continued away from the platform. The relatively fast infill of the basin resulted in the creation of a shallow-water environment suitable to produce large amounts of large benthic foraminifers (Unit II). The last episode in the evolution of the Kardiva Channel is an open-marine environment in which currents continuously remobilize the sediments (Unit I).

Figure F16. Large benthic foraminifers (359-U1468A-107X-1, 86–89 cm; PPL). General overview of large benthic foraminiferal rudstone: A, C, D. Yellow arrows = *Heterostegina* sp., white arrows = *Amphistegina* sp. B. *Sphaerogypsina* sp. E. *Amphistegina* sp. F. *Sphaerogypsina* sp.

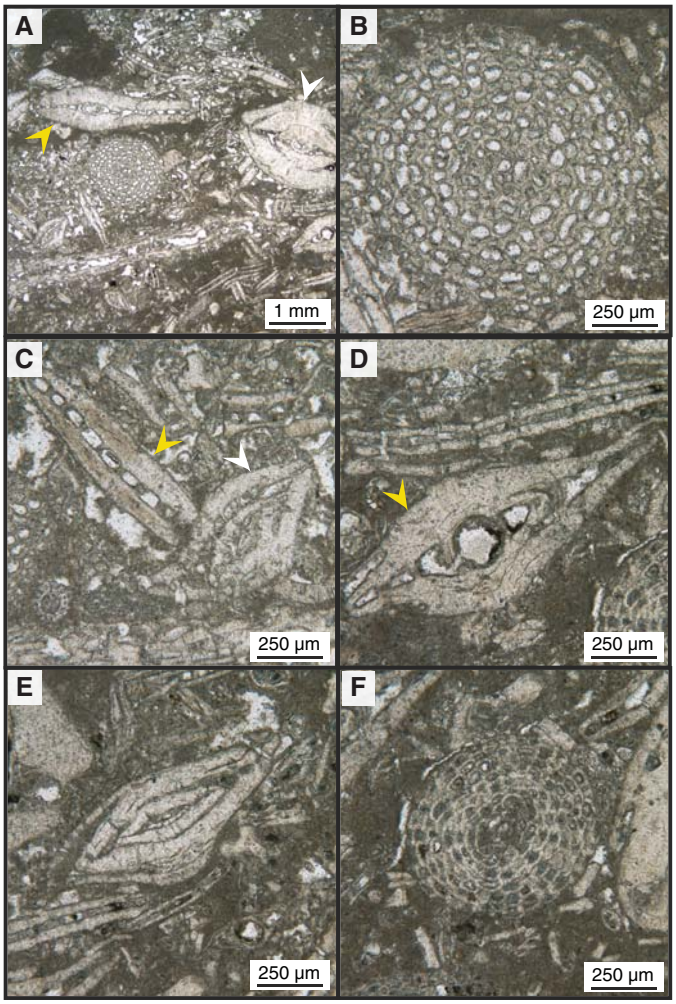

Figure F17. Oligocene limestone (359-U1468A-111X-CC, 0–2 cm; PPL). A. 1 = hooked shaped red algae, 2 = *Halimeda*, 3 = *Heterostegina* sp., 4 = echinoid fragment, 5 = gastropod fragment. B. Close-up of red algal thallus.

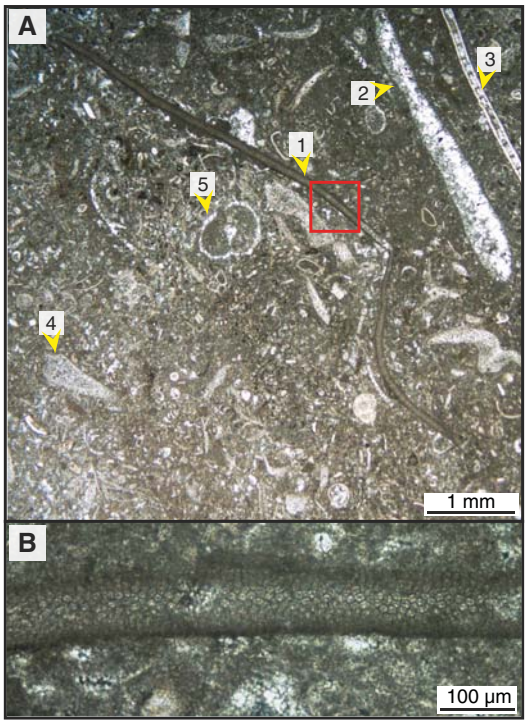

Figure F18. Geopetal infill in Oligocene limestone (359-U1468A-111X-CC, 0–2 cm; PPL). A. Geopetal filling in a *Halimeda* mold. B. Close-up showing cement on top of geopetal infilling. C. Boundary between micrite and micritized fine sediment infill overgrown (white arrow) with blocky calcite crystals (black arrow).

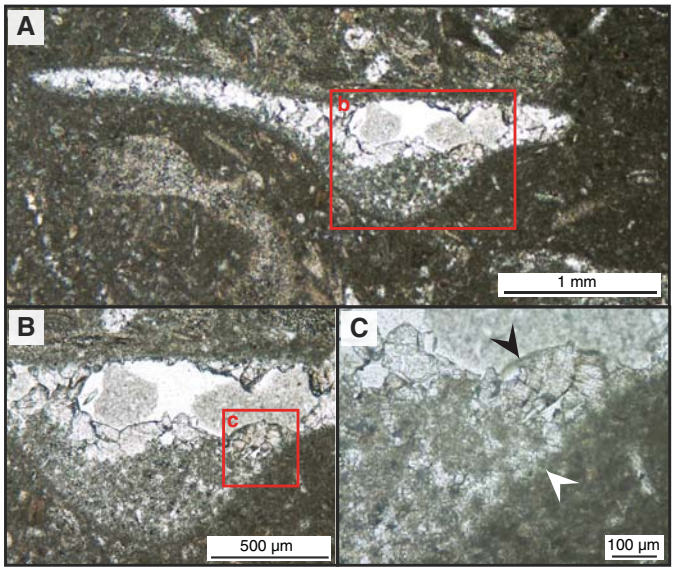

Figure F19. *Halimeda* plate molds and void-filling blocky calcite (359-U1468A-111X-CC, 0–2 cm; XPL). A. White arrows = leached *Halimeda* plate filled with blocky calcite crystals showing colorful interference. B. Close-up of blocky calcite crystals.

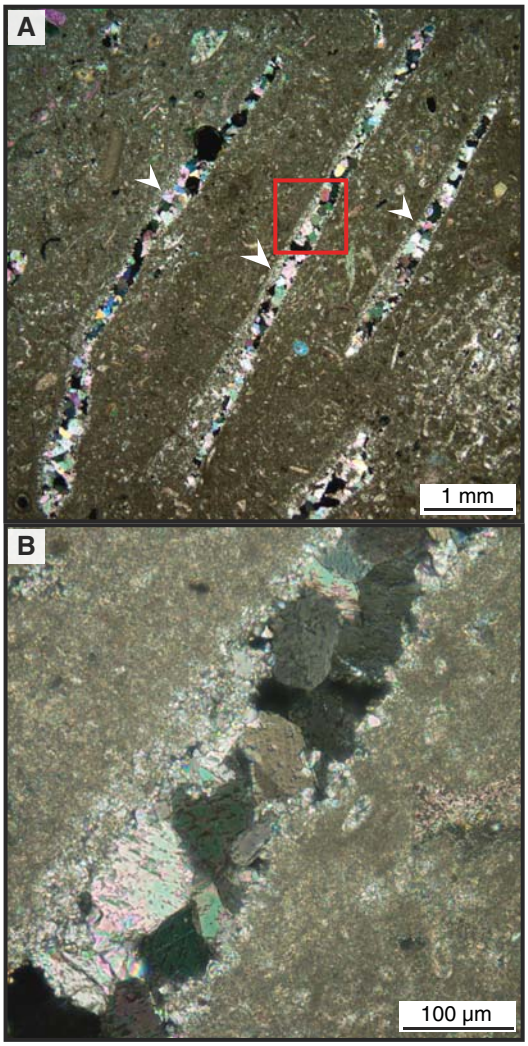

Figure F20. Pellets in burrow cemented by sparry calcite from the Oligocene shallow-water platform (359-U1468A-111X-CC, 0–2 cm; XPL). A. Burrow with pellets. B. Black arrow = sparry cements between pellets. C. White arrow = gastropod preserved in a pellet, black arrow = bridging sparry cements.

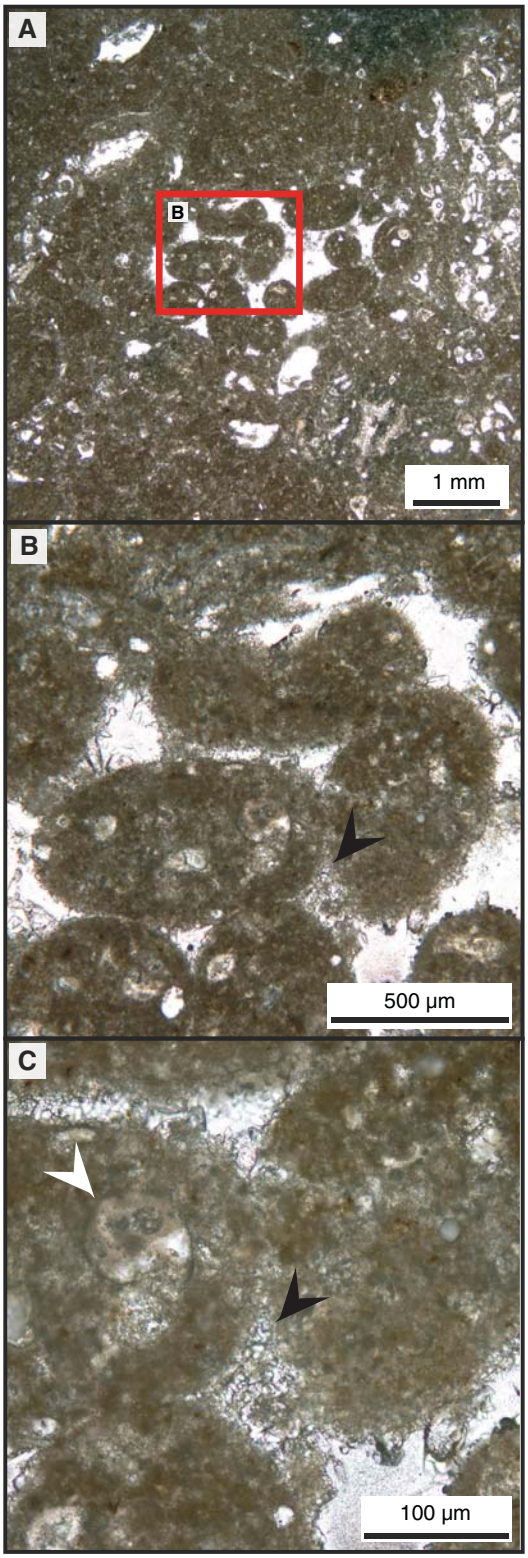

Biostratigraphy

An ~865 m thick succession was recovered at Site U1468 that ranges in age from the Late Pleistocene to late Oligocene. A major hiatus separates Miocene from Pliocene–Pleistocene sediments. All core catcher samples from Hole U1468A were examined by the shipboard paleontologists. The sequence is divided into four intervals (A–D) based on abundance and preservation of calcareous microfossils (Figure **F21**).

Interval A was recovered in Cores 359-U1468A-1H through 5H and extends from the surface to ~45 mbsf. This part of the sequence ranges in age from late Pliocene to Quaternary. The lower part of the Pliocene is missing. Nannofossils are generally sparse, with the

Figure F21. Biostratigraphic and paleoenvironmental summary, Site U1468. Calcareous nannofossil and planktonic foraminifer biozonation is shown with paleoenvironmental information provided by benthic foraminifers and ostracods.

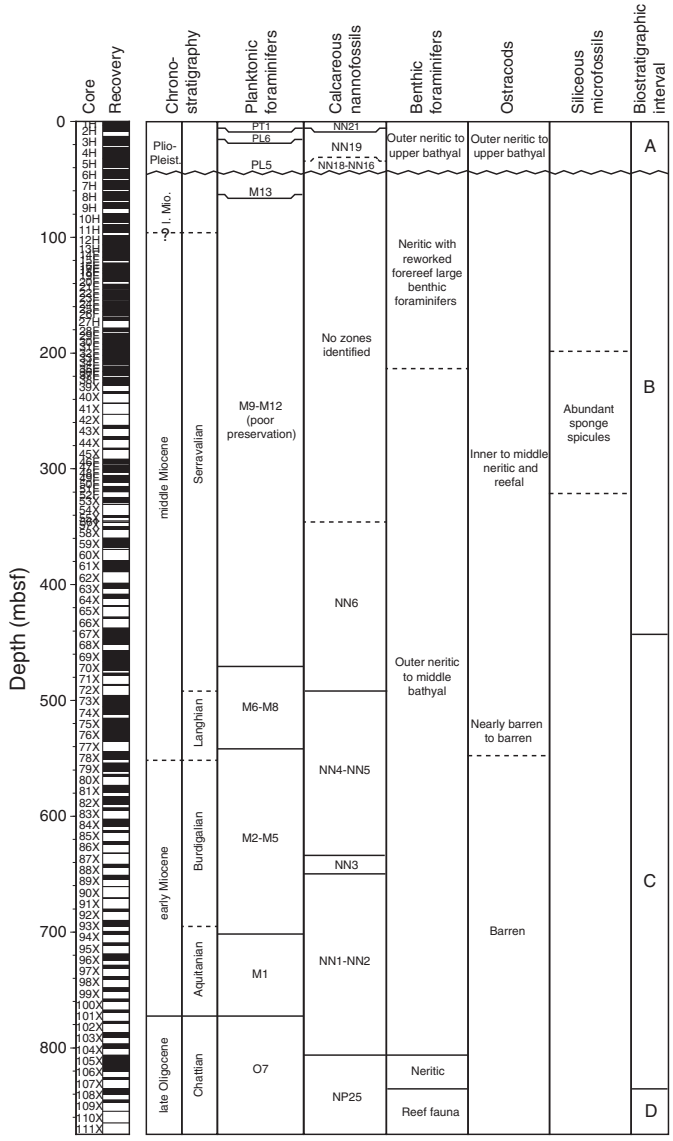

exception of well-preserved coccoliths in the uppermost Sample 1H-CC. Planktonic and benthic foraminifers are moderately abundant in this interval. Ostracods are present but in even lower abundances. The benthic foraminiferal and ostracod assemblage suggests an outer neritic to upper bathyal depositional environment.

Interval B was recovered in Cores 6H–66X. This thick section extends from about 45 to 429 mbsf. It comprises middle Miocene to late Miocene calcareous microfossils, which are generally sparse and poorly preserved throughout the succession. Sample 6H-CC contains a few late Miocene to Pliocene–Pleistocene specimens of planktonic foraminifers mixed with abundant poorly preserved large benthic foraminifers with signs of abrasion and calcite overgrowth. Samples 6H-CC to 30F-CC contain high to moderate amounts of large benthic foraminifers derived from a neritic origin. Siliceous sponge spicules are abundant in Samples 32F-CC to 52F-CC. The base of interval B most likely corresponds to the base of the drift sequence as determined by lithology and seismic facies changes (see **Lithostratigraphy** and **Seismic stratigraphy**).

Interval C (Cores 67X–107X) ranges in age from the middle Miocene to late Oligocene. Calcareous microfossils are abundant and show moderate to good preservation.

Interval D (Cores 108X–111X) contains mainly large benthic foraminifers derived from a fore-reef environment.

Age model

The biostratigraphic events recognized at this site are listed in Table **T2**. Figure **F21** summarizes the biostratigraphic zonal assignments of the intervals previously described and the paleoenvironmental interpretation. Biostratigraphic events are also shown in the age-depth plot given in Figure **F22**, which allows direct comparison of the data and calculation of implied sedimentation rates.

The age model for interval A is poorly constrained because most nannofossil zonal markers are missing. Planktonic foraminiferal events indicate a sedimentation rate of less than 1 cm/ky above the hiatus, and therefore the Pliocene–Quaternary section at this site is thinner than it was at previous sites.

In interval B, very few bioevents were recognized because the calcareous assemblages from both the nannofossils and planktonic foraminifers are very poorly preserved and/or diluted throughout, hampering assignment of zonal boundaries and/or reliable datum levels. Allocation of reliable datum levels is further compounded by the possibility of reworking, given that this interval represents a drift deposit (see **Lithostratigraphy** and **Seismic stratigraphy**). Nevertheless, a few datum levels were tentatively assigned. Sparse specimens of zonal markers *Neogloboquadrina acostaensis* (first occurrence [FO] dated at 9.83 Ma) and *Paragloborotalia mayeri* (last

Table T2. Biostratigraphic events, Site U1468. FO = first occurrence, LO = last occurrence, LCO = last common occurrence. FO *E. huxleyi* is not very well constrained. Unambiguous *P. lacunosa* occur. Only rare overgrown specimens of *D. brouweri* were seen, so confidence in the LO is low. LO *C. nitescens* has very large error bars because assemblages are very poor until Sample 359-U1468A-66X-CC. LCO *C. floridanus* is uncertain because single common occurrence in Sample 70-CC may be unreliable. LO and FO *S. heteromorphus* are very clear and well constrained. LO *S. belemnos* is poorly constrained because of poor recovery and preservation. FO *Sphenolithus belemnos* is quite well constrained; the absence of *S. pseudoheteromorphus* is surprising, especially when compared to Site U1467. LO *S. ciperoensis* is clear and well constrained; absence of *S. delphix* is anomalous, especially when compared to Site U1467, but might be resolved by additional sampling. *S. distentus* does not occur in the last sample from which a reasonable nannofossil assemblage was recovered (>20 specimens of *S. ciperoensis* were observed in this sample). PF = planktonic foraminifer, N = nannofossil. See Raffi et al. (2006) for a review of nannofossil events and original sources for correlations to magnetostratigraphic timescales. NA = not available. **Download table in .csv format.**

Event	Abbreviation	Fossil group	Age (Ma)	Age reference	Core, section, interval (cm) last sample above event	Core, section, interval (cm) first sample below event	Top depth (mbsf)	Bottom depth (mbsf)	Midpoint depth (mbsf)
					359-U1468A-	359-U1468A-			
LO *Globigerinoides ruber* pink	L *G.rp*	PF	0.12	Thompson et al. (1979)	1H-1- mudline	1H-CC	0.05	3.35	1.7
FO *Emiliania huxleyi*	F *E.h*	N	0.29	Hilgen et al. (2012)	1H-CC	2H-CC	3.4	8.8	6.1
LO *Pseudoemiliania lacunosa*	L *P.l*	N	0.44	Hilgen et al. (2012)	1H-CC	2H-CC	3.4	8.8	6.1
LO *Globigerinoides fistulosus*	L *G.f*	PF	1.88	Lourens et al. (2004)	1H-CC	2H-CC	3.4	8.8	6.1
LO *Discoaster brouweri*	L *D.b*	N	1.93	Hilgen et al. (2012)	4H-CC	5H-CC	31.2	40.5	35.9
LO *Globorotalia limbata*	L *G.l*	PF	2.39	Lourens et al. (2004)	2H-CC	3H-CC	8.8	21.6	15.2
FO *Globigerinoides fistulosus*	F *G.f*	PF	3.33	Berggren et al. (1995)	5H-CC	6H-CC	40.6	50.1	45.3
FO *Sphaeroidinella dehiscens*	F *S.d*	PF	5.53	Lourens et al. (2004)	6H-CC	7H-CC	50.1	59.4	54.7
FO *Neogloboquadrina acostaensis*	F *N.a*	PF	9.83	Lourens et al. (2004)	7H-CC	8H-CC	59.4	69.0	64.2
LO *Paragloborotalia mayeri*	L *P.m*	PF	10.46	Lourens et al. (2004)	8H-CC	9H-CC	69.0	75.7	72.3
LO *Coronocyclus nitescens*	L *C.n*	N	12.12	Young (1998)	65H-CC	66X-CC	419.2	429.0	424.1
LCO *Cyclicargolithus floridanus*	L *C.f*	N	13.28	Hilgen et al. (2012)	70X-5, 71	73X-2, 75	473.3	497.9	485.6
FO *Fohsella fohsi*	F *F.f*	PF	13.41	Lourens et al. (2004)	69X-CC	70X-CC	466.6	474.8	470.7
LO *Sphenolithus heteromorphus*	L *S.h*	N	13.53	Hilgen et al. (2012)	72X-CC	73X-2, 75	486.9	497.9	492.4
FO *Orbulina suturalis*	F *O.s*	PF	15.1	Berggren et al. (1995)	76X-CC	78X-CC	534.6	551.2	542.9
FO *Sphenolithus heteromorphus*	F *S.h*	N	17.71	Hilgen et al. (2012)	86X-2, 63	86X-CC	624.0	624.7	624.3
LO *Sphenolithus belemnos*	L *S.b*	N	17.95	Hilgen et al. (2012)	86X-CC	88X-3, 13	624.7	643.7	634.2
FO *Sphenolithus belemnos*	F *S.b*	N	19.03	Hilgen et al. (2012)	88X-CC	89X-3, 14	644.7	653.7	649.2
LO *Paragloborotalia kugleri*	L *P.k*	PF	21.12	Lourens et al. (2004)	93X-CC	95X-CC	694.7	711.1	702.9
FO *Paragloborotalia kugleri*	F *P.k*	PF	22.96	Lourens et al. (2004)	101X-CC	102X-CC	769.7	779.4	774.6
LO *Sphenolithus ciperoensis*	L *S.c*	N	24.04	Hilgen et al. (2012)	105X-1, 20	105X-1, 110	806.4	807.3	806.9
LO *Sphenolithus distentus*	L *S.d*	N	27.27	Hilgen et al. (2012)	109X-2, 22	NA	846.7	>846.7	>846.7

Figure F22. Age-depth plot, Site U1468. Details of each event plotted are given in Table **T2**.

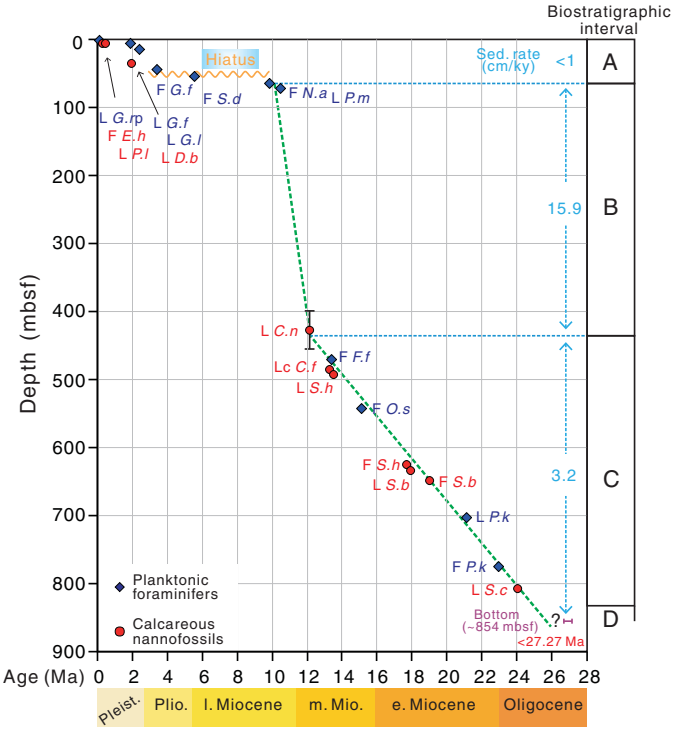

occurrence [LO] dated at 10.46 Ma) were found almost at the top of interval B in Samples 7H-CC and 9H-CC, respectively. The presence of *N. acostaensis* and *P. mayeri* in close samples suggests a maximum age of ~10 Ma for the top part of interval B. Interestingly, Sample 6H-CC contains a few younger Pliocene–Pleistocene microfossils, most likely a consequence of mixing after sedimentation resumed.

The age of the bottom of interval B was inferred from calcareous microfossils in the sample directly below the interval. Preservation and abundance of planktonic microfossils rather abruptly increase between Cores 66X and 67X, the boundary between intervals B and C. Because the assemblages above and below are broadly similar, it is likely the contact is conformable, as also suggested by the seismic data (see **Seismic stratigraphy**); hence, we can use the age of the underlying sediments to constrain the age of the base. The age model suggests an age of ~12 Ma for the boundary between intervals B and C and implies an average sedimentation rate of 15.9 cm/ky for interval B.

In interval C, preservation and abundance of planktonic calcareous microfossils is variable, but many samples yielded well-developed assemblages. Therefore, several reliable events were placed with a high degree of certainty (Table **T2**; Figure **F22**). These events lie neatly along a single line of correlation, implying an average sedimentation rate of approximately 3.2 cm/ky. This sedimentation rate suggests that sediments from this interval are hemipelagic in nature because the rate is still relatively high for a true pelagic deposit. Among the reliable events, we include the FO of *Paragloborotalia kugleri*, which indicates the Oligocene/Miocene boundary, and the LO of the late Oligocene species *Sphenolithus ciperoensis*, which indicates unambiguously that the base of the section is late Oligocene in age. By extrapolating the linear trend of the

Table T3. Nannofossil range chart, Hole U1468A. **Download table in .csv format.**

average sedimentation rate to the base of the interval, we suggest an age of ~26 Ma for the bottom of the interval. Interval D comprises limestones rich in large benthic foraminifers that indicate a fore-reef depositional environment. This limestone cannot be directly dated because of the absence of planktonic microfossils.

Calcareous nannofossils

Interval A: Quaternary to late Pliocene (Cores 359-U1468A-1H through 5H)

Nannofossils are abundant and well preserved in the first core catcher sample (1H-CC), but both preservation and abundance rapidly deteriorate downhole. Sample 1H-CC contains *Emiliania huxleyi* and is clearly from Zone NN21. The presence of *Pseudoemiliania lacunosa* and absence of *Sphenolithus* spp. (apart from very rare likely reworked specimens) in this interval suggest it is Quaternary to late Pliocene in age, but events are not well marked. The FO of *Discoaster brouweri* appears to occur between Samples 4H-CC and 5H-CC, which indicates that the entire interval is Quaternary (sensu Gradstein et al., 2012); however, planktonic foraminifers indicate an older age.

Interval B: middle to late Miocene (Cores 359-U1468A-6H through 66X)

Nannofossils occur in most samples from interval B, but they are usually present in very low abundances. Only long-ranging forms were observed (Table **T3**), such as *Reticulofenestra* spp., *Umbilicosphaera jafari*, *Sphenolithus abies*, and *Coccolithus pelagicus*. Abundances and diversity increase slightly downhole. The absence of *Cyclicargolithus*, *Pseudoemiliania*, and *Gephyrocapsa* indicates an age of Zones NN6 to NN15, but we could not identify the biozone boundaries. *Coronocyclus nitescens* is present in several samples from the lower part of the interval, and a tentative LO between Samples 65H-CC and 66X-CC is indicated in Figure **F22**, although the uncertainty for this event is large.

Interval C: middle Miocene to late Oligocene (Cores 359-U1468A-67X through 107X)

Nannofossils are generally abundant and moderately well preserved throughout interval C, and the most reliable marker events were readily placed. These included, in particular, the FO and LO of *Sphenolithus heteromorphus* and the LO of *S. ciperoensis*. Those events were better constrained by analyzing additional samples from sections above and below the core catcher samples in which they were first determined. The LO of *S. ciperoensis* and the FO of *S. heteromorphus* were well constrained within intervals of 0.9 and 2.7 m, respectively, but the LO of *S. heteromorphus* fell in an area of poor core recovery and could only be constrained within an interval of 11 m.

Unambiguous specimens of *Sphenolithus belemnos* occur in a couple of samples, but the FO and LO were not well constrained because of poor core recovery. *Sphenolithus pseudoheteromorphus*, which is stratigraphically immediately below *S. belemnos* in this region (Fornaciari et al., 1990; Fornaciari and Agnini, 2009), was not observed in the studied samples. In contrast, at Site U1466 *S. belemnos* was absent and *S. pseudoheteromorphus* was conspicuous. This difference is probably the result of discontinuous recovery in both holes. *Sphenolithus calyculus* and *Sphenolithus delphix* are also absent at Site U1468 but present at Site U1466. *S. delphix* has a very

short range, ~0.3 Ma (Backman et al., 2012) and could fall within a single core. The restriction of *S. calyculus* to Site U1466 is harder to explain.

Helicosphaera ampliaperta is frequent and well preserved in Sample 82X-3, 60 cm, but was not found in other samples, indicating that the species is only sporadically present and therefore unsuitable as a zonal marker in this area. Rio et al. (1990) also report *H. ampliaperta* as being only sporadically present in most sites drilled during ODP Leg 115 in the northwest Indian Ocean. Samples from the base of the section, especially the last sample with frequent *S. ciperoensis* (Sample 109X-2, 22 cm), were carefully checked for the possible presence of *S. distentus*. No specimens of *S. distentus* were found; hence, it is reasonable to conclude that the base of Interval C is above the LO of *S. distentus* (i.e., younger than 27.27 Ma).

Interval D: Oligocene (Cores 359-U1468A-108X through 111X)

Samples were taken from the hard white limestones of this unit, but no nannofossils were found in the smear slides.

Planktonic foraminifers

Planktonic foraminifers were examined in all core catcher samples from Hole U1468A (110 samples). The mudline sample from this hole was also examined. The distribution of selected species is given in Table **T4**. The planktonic foraminiferal biozonation is given in Figure **F21**. A significant hiatus was recognized between Samples 5H-CC and 7H-CC based on the absence of Zones PL1–PL4 and M14. Foraminifer preservation is moderate to good in interval A. Preservation of planktonic foraminifers is very poor and abundances are extremely low in interval B, making age assignments difficult. Planktonic foraminifers are moderately abundant and moderately preserved in interval C, allowing confident age assignments in this part of the sequence. The absence of planktonic foraminifer shells in interval D prevents age assignment for the bottom of the borehole.

Interval A: Quaternary to late Pliocene (Cores 359-U1468A-1H through 5H)

Planktonic foraminifers are abundant and show moderate to good preservation. Three successive Pleistocene bioevents were identified: the LO of *Globigerinoides ruber* pink (0.12 Ma) was found in Sample 1H-CC, followed by the LO of *Globigerinoides fistulosus* (1.88 Ma) in Sample 2H-CC and the LO of *Globorotalia limbata* (2.39 Ma) in Sample 3H-CC. The Pliocene is partially or even completely missing from this interval. Sample 5H-CC yields *G. fistulosus* specimens, implying an age younger than 3.33 Ma.

Interval B: middle to late Miocene (Cores 359-U1468A-6H through 66X)

The abundance of planktonic foraminifers is low in interval B, and preservation ranges from moderate to very poor. Many core catcher samples are barren in this thick expanded sequence with a high sedimentation rate (Figure **F22**; Table **T4**). A significant hiatus was identified between Samples 5H-CC and 7H-CC based on *P. mayeri* and *N. acostaensis* assemblages below the hiatus and late Pliocene to Pleistocene assemblages above. Sample 6H-CC is problematic because it yields a few specimens of late Miocene to Pleistocene age within an assemblage of reworked large benthic foraminifers. We interpret this sample as a mixture of reworked material.

Interval C: middle Miocene to late Oligocene (Cores 359-U1468A-67X through 107X)

The abundance and preservation of planktonic foraminifers increases in this interval, with preservation ranging from good to poor. We identified the following events: the FO of *Fohsella fohsi* (13.41 Ma) between Samples 69X-CC and 70X-CC, the FO of *Orbulina suturalis* (15.1 Ma) between Samples 76X-CC and 78X-CC, the LO of *P. kugleri* (21.12 Ma) between Samples 93X-CC and 95X-CC, and the FO of *P. kugleri* (22.96 Ma) between Samples 101X-CC and 102X-CC. The FO of *P. kugleri* is a good indicator of the Oligocene/Miocene boundary.

Interval D: Oligocene (Cores 359-U1468A-108X through 111X)

Planktonic foraminifers are absent in this interval. Therefore, we cannot assign an age to this interval based on planktonic foraminifer biostratigraphy.

Benthic foraminifers

Site U1468 provides a late Oligocene to Quaternary record of neritic to middle bathyal benthic foraminiferal assemblages. Preservation of benthic foraminifers ranges from very good to poor throughout this succession. Four intervals (A–D) were determined for this site based on planktonic foraminifers and nannofossil biostratigraphy (Figure **F21**). Benthic foraminifer specimens in interval A are well preserved and indicate a neritic to outer bathyal environment. Interval B is dominated by the presence of large benthic foraminifers of the fore-reef environment. Interval C is mainly composed of poorly preserved benthic foraminifers of the outer neritic to middle bathyal environment. Interval D contains moderately preserved large fore-reef benthic foraminifers from the Oligocene platform (Table **T5**).

Interval A: Quaternary to Pliocene (Cores 359-U1468A-1H through 5H)

Seven samples were investigated from interval A spanning the Pleistocene and late Pliocene. Samples 1H-CC through 5H-CC contain neritic to outer bathyal benthic foraminifers with very good to good preservation. Samples from this interval include abundant specimens of *Cibicides* sp., *Lenticulina* sp., *Sigmoilopsis* sp., and *Planulina* sp.

Interval B: middle to late Miocene (Cores 359-U1468A-6H through 66X)

In interval B, 24 late to middle Miocene samples were investigated. Late Miocene samples are poorly preserved, and there is an abrupt change in benthic fauna in Samples 6H-CC and 7H-CC. This interval is dominated by large benthic foraminifers from the fore-reef depositional environment. Overgrowth is present in all benthic specimens, and overall these samples have moderate preservation (broken tests), indicating reworking of this material (Figure **F23**). The large benthic foraminiferal assemblage is dominated by *Lepidocyclina* sp., *Sphaerogypsina* sp., *Baculogypsina* sp., *Nummulites* sp., and *Amphistegina* sp. Middle Miocene sediments are characterized by alternations of light and dark sediments, and the abundance of

Table T4. Planktonic foraminifer range chart, Hole U1468A. **Download table in .csv format.**

Table T5. Benthic foraminifer range chart, Hole U1468A. **Download table in .csv format.**

benthic foraminifer genus *Bolivina* increases in Sample 66X-CC and decreases downhole, becoming rare in Sample 75X-CC (Figure F24).

Figure F23. Foraminifer preservation plates, Hole U1468A. A, B. Foraminiferal assemblages with calcite overgrowth (6H-CC and 15H-CC). C. Early Miocene light layers (102X-CC). D. Early Miocene dark layers (103X-CC). Scale bars = 1 mm.

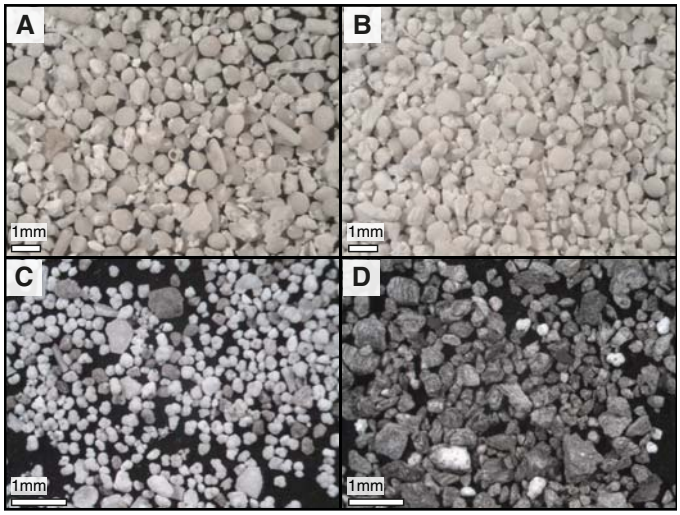

Interval C: middle Miocene to late Oligocene (Cores 359-U1468A-67X through 107X)

Interval C spans the late Oligocene to early Miocene. Thirteen samples were investigated. Overall, preservation of benthic foraminifer specimens ranges from moderate to poor. The presence of *Uvigerina* sp., *Cibicides* sp., *Planulina* sp., *Lenticulina* sp., and *Siphonina pozonensis* indicates an outer neritic to middle bathyal environment.

Interval D: Oligocene (Cores 359-U1468A-108X through 111X)

Interval D spans the late Oligocene. Four core catcher samples from limestones were examined from this interval. The abundance of large fore-reef benthic foraminiferal fauna indicates that these samples originate from the platform environment. Most common benthic foraminifers in this interval belong to *Amphistegina* sp., *Lepidocyclina* sp., and *Operculina* sp., and they are moderately preserved. An increase in abundance of the genus *Bolivina* was identified in this interval in Samples 107X-CC and 108X-CC, indicating low-oxygen waters or bottom conditions. Specimens of *Lepidocyclina* have chambers infilled with glauconite (Figure F24). Glauconite is abundant throughout this interval, and many benthics are partially infilled.

Ostracods

A preliminary study of the ostracods was conducted during examination of Hole U1468A core catcher samples for benthic foraminifers (Table T6). Ostracods were present only in Pleistocene

Figure F24. Plate of middle to late Miocene large benthic foraminifers, Hole U1468A. 1. *Nummulites* sp. (9H-CC). 2, 3. *Cycloclypeus* sp. (9H-CC). 4. *Discogypsina* sp. (10H-CC). 5. *Baculogypsina sphaerulata* (10H-CC). 6. *Amphistegina* sp. (13H-CC). 7. *Operculina ammonoides* (15H-CC). 8. Unidentified fish tooth (10H-CC). 9. *Polymorphina* sp. (15H-CC). 10. *Sphaerogypsina* sp. (15H-CC). 11. Larger benthic foraminifer from Oligocene platform interval with glauconite-filled chambers, *Lepidocyclina* sp. (109X-CC). Scale bars = 100 µm.

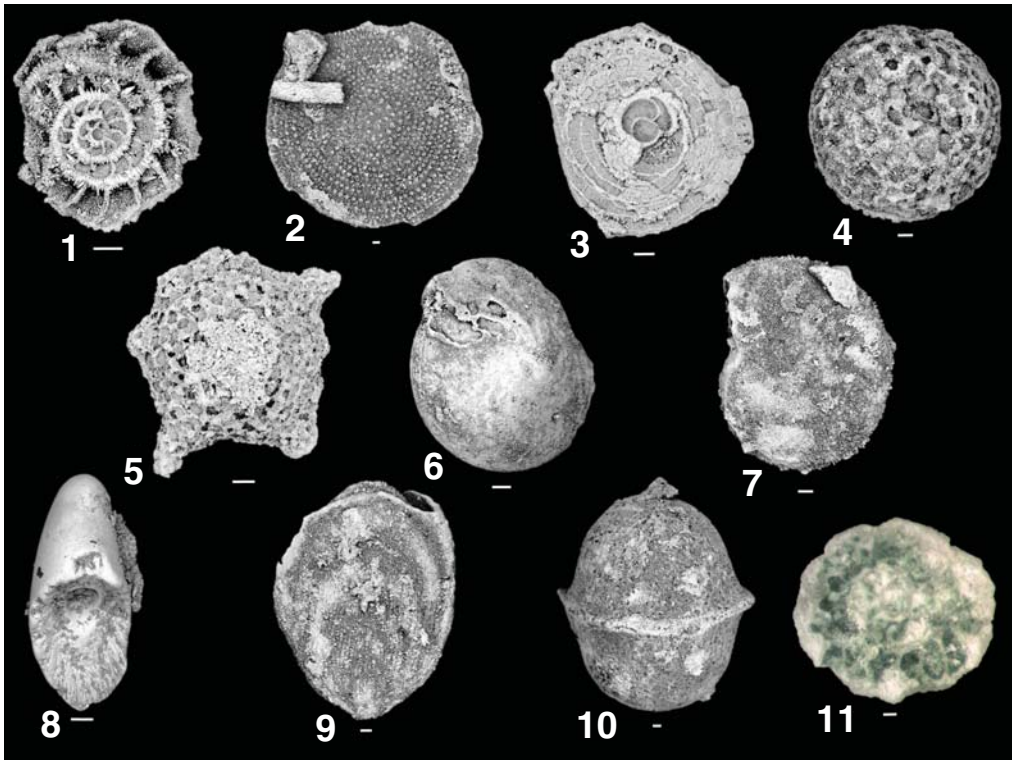

Table T6. Ostracod range chart, Hole U1468A. **Download table in .csv format.**

Samples 1H-CC to 4H-CC and middle Miocene Samples 20F-CC, 30F-CC, 35F-CC, 39X-CC, 40X-CC, 50F-CC, 55X-CC, 61X-CC, and 66X-CC.

Pleistocene ostracod fauna

Ostracods are most abundant and better preserved in the Pleistocene samples. The assemblage is composed of the genera *Bradleya*, *Loxoconcha*, *Mutilus*, and *Xestoleberis*, as well as several genera from the Bairdiidae, which provide a paleoenvironmental interpretation of outer neritic to upper bathyal depths.

Middle Miocene ostracod fauna

Ostracods are rare in the middle Miocene section and show moderate to poor preservation. This assemblage is composed of species of *Aurila*, Bairdiids, *Loxoconcha*, *Leptocythere*, *Loxocorniculum*, and *Mutilus*. This assemblage is interpreted to represent inner to middle neritic and reefal environments.

Radiolarians

A total of 39 core catcher samples from Hole U1468A were prepared for radiolarian analysis, but no radiolarians were found. Siliceous microfossils such as sponge spicules and diatoms increase in abundance from Sample 32F-CC (201.66 m CSF-A), peak in Sample 39H-CC (228.55 m CSF-A), and disappear in Sample 53H-CC (329.68 m CSF-A).

Geochemistry

Interstitial water chemistry

Interstitial water (IW) samples were taken from Hole U1468A by squeezing samples at a rate of one per core (recovery permitting). Concentrations of all species measured are presented in Table T7. For Site U1468 and subsequent Expedition 359 sites, we modified the procedure for measuring the pH of the IW samples (see **Geochemistry** in the Expedition 359 methods chapter [Betzler et al, 2017a]), and therefore the values obtained are considered to be more realistic for the in situ conditions. For Site U1468, the data obtained for the major elements (Na^+, K^+, Ca^{2+}, and Mg^{2+}) using ion chromatography (IC) was of considerably better quality than that from inductively coupled plasma–atomic emission spectroscopy (ICP-AES), and therefore the IC data are used in this section. All data are included in Table T7. The correlation between the determination of Cl^- using IC and that obtained from titration is reasonably good (in contrast to data obtained at Sites U1466 and U1465), although not quite what might be expected (R^2 = 0.73). As at previous sites, data from titration is used except when comparing data analyzed using the IC.

Chloride, bromide, and salinity

Concentrations of Cl^- steadily increases from seawater values of ~550 mM at the seawater/sediment interface to between 580 and 585 mM at ~90 mbsf (Figure F25; Table T7), approximately coincident with the lithostratigraphic Unit II/III boundary (see **Lithostratigraphy**).

Concentrations of Br^- vary between ~420 and 520 µM and, similar to other Expedition 359 sites, exhibits a strong correlation with Cl^- (R^2 = 0.94).

Salinity ranges between 35 and 36 throughout the core.

Sodium and potassium

Concentrations of Na^+ range between ~480 and 500 mM and increase with depth, similar to Cl^- (Figure F25; Table T7). Concentrations of these two elements (R^2 = 0.93), normally considered to be conservative, are strongly correlated, in contrast to Site U1466, where they are weakly correlated.

In contrast to Na^+ and Cl^-, K^+ behaves quite differently, gradually increasing to a peak concentration at ~500 mbsf.

Alkalinity, pH, ammonium, and dissolved sulfate

The pH decreases steadily from ~7.8 in the upper portion of the core to ~7.3 at the base of the core (Figure F26; Table T7) (see **Geochemistry** in the Expedition 359 methods chapter [Betzler et al, 2017a] regarding errors associated with pH measurements).

Concentrations of SO_4^{2-} increase with depth in the upper 100 mbsf, a change attributable to the increase in salinity. To unravel changes in SO_4^{2-} as a result of changes in salinity from bacterial sulfate reduction (BSR), it is useful to normalize the concentration relative to seawater at the top of the core. The excess (or deficit) of SO_4^{2-} (or any element) relative to Cl^- can be calculated using Equation 1. For the purposes of this exercise, SO_4^{2-} and Cl^- in the mudline seawater sample are used as a reference. Sulfate minimally changes in the upper 200 mbsf, but coincident with the transition between lithostratigraphic Units II and III, the amount of SO_4^{2-} corrected for the change in Cl^- declines by about 4 to 5 mM toward the base of Hole U1468A (Figure F27):

Table T7. Interstitial water chemistry, Site U1468. **Download table in .csv format.**

Figure F25. IW Cl^-, Na^+, and K^+ concentrations, Hole U1468A.

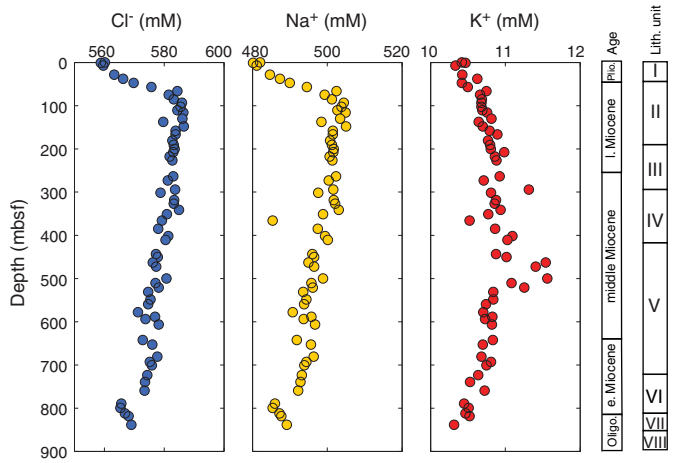

Figure F26. IW alkalinity, hydrogen (pH), SO_4^{2-}, and NH_4^+ concentrations, Hole U1468A.

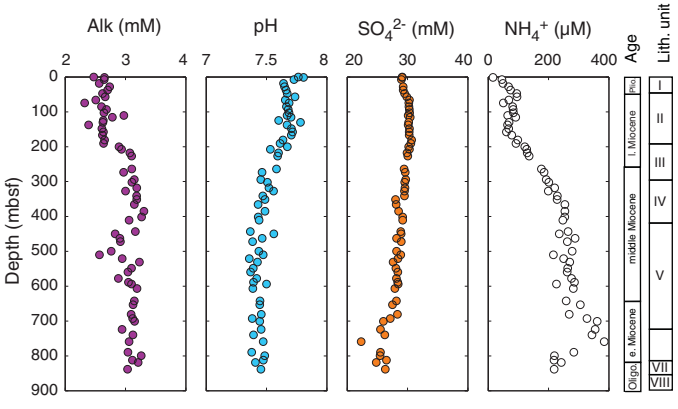

Figure F27. Excess Ca^{2+}, Mg^{2+}, SO_4^{2-}, and alkalinity in IW, Site U1468.

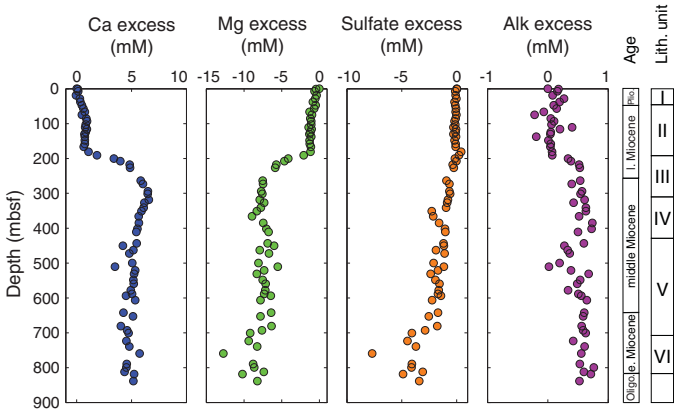

$$\text{Excess sulfate (mM)} = SO_4^{2-}{}_{\text{sample}} - SO_4^{2-}{}_{\text{seawater}} \times [Cl^-{}_{\text{sample}}/Cl^-{}_{\text{seawater}}]. \quad (1)$$

Alkalinity varies between 2.2 and 2.6 mM in the upper 200 mbsf. At 200 mbsf, coincident with the lithostratigraphic Unit II/III boundary (see **Lithostratigraphy**), alkalinity increases abruptly to values greater than 3 mM. Values remain at this concentration until the base of the cored interval, with the exception of a decrease toward seawater values between 400 and 600 mbsf. Alkalinity normalized to Cl^- increases slightly with depth. Overall, alkalinity normalized to Cl^- increases by approximately 1 mM.

Ammonium concentrations increase from ~20 µM in the uppermost core in Hole U1468A to between 50 and 100 µM between 10 and 200 mbsf. Values then increase to ~250 to 300 µM coincident with the transition between lithostratigraphic Units II and III. Peak values were measured in lithostratigraphic Unit V (400 µM).

Calcium, magnesium, strontium, and lithium

Concentrations of Ca^{2+} increase from seawater values of approximately 10.2 mM at the top of Hole U1468A to ~12.5 mM at 100 mbsf (Figure **F28**). Between 100 and 200 mbsf, Ca^{2+} remains constant at ~12.5 mM. At 200 mbsf, coincident with the lithostratigraphic Unit II/III boundary, Ca^{2+} increases very rapidly to approximately 16 mM. It remains at approximately this value to the base of Hole U1468A. The concentration of Ca^{2+} normalized to Cl^- increases approximately 5–6 mM (Figure **F27**).

Changes in Mg^{2+} mirror those seen in Cl^- over the upper 200 mbsf, but at 200 mbsf there is a substantial decrease in the normalized concentration of about 7 to 8 mM. As a consequence, the Mg^{2+}/Ca^{2+} ratio of the pore fluids (Figure **F29**) shows a substantial decrease coincident with the lithostratigraphic Unit II/III boundary.

The concentration of Sr^{2+} shows a small increase over the upper 200 mbsf (Table **T7**). Below this depth and associated with the lithostratigraphic Unit II/III boundary, Sr^{2+} increases dramatically to approximately 450–470 µM. It remains the same between 200 and 600 mbsf and then declines to ~220 µM.

Concentrations of Li^+ remain similar to that of seawater over the upper 200 mbsf. Coincident with the lithostratigraphic Unit II/III boundary, Li^+ decreases to ~20 µM.

Manganese, iron, barium, boron, and silicon

Iron concentrations are low throughout Hole U1468A (Figure **F30**; Table **T7**). Barium is approximately 0.5 µM throughout the site, and boron shows a very small but gradual increase throughout Hole U1468A, reaching more than 500 µM at the base.

Silicon remains stable for the uppermost 200 mbsf and then increases rapidly to ~ 800 µM between 200 and 500 mbsf. From 500 mbsf to the base of the core, concentrations decrease to values near seawater.

Figure F28. IW Ca^{2+}, Mg^{2+}, Sr^{2+}, and Li^+ concentrations, Hole U1468A.

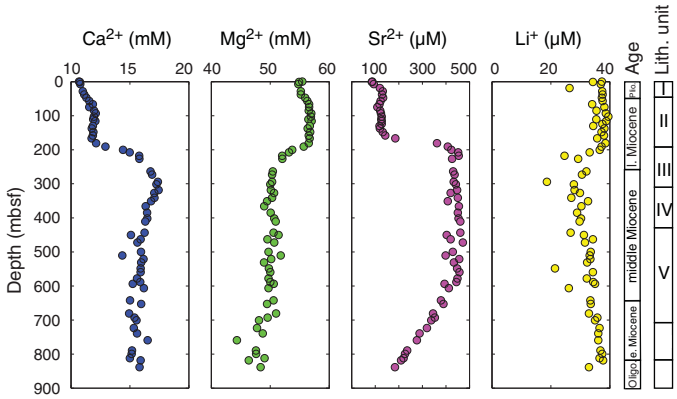

Figure F29. IW Sr^{2+}/Ca^{2+}, Mg^{2+}/Ca^{2+}, Ca^{2+}/Cl^-, and Mg^{2+}/Cl^-, Site U1468.

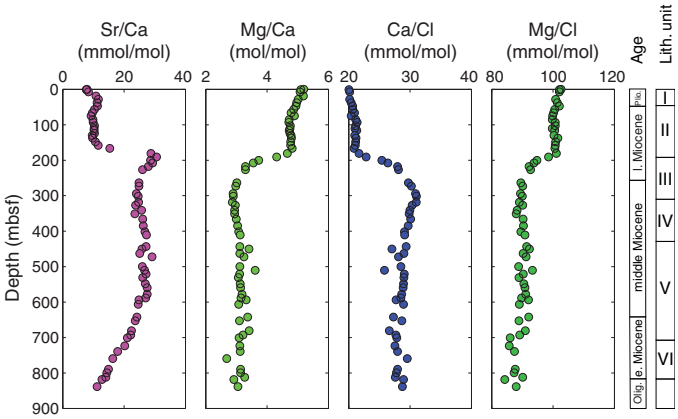

Figure F30. IW Fe, B, Ba^{2+}, and Si concentrations, Site U1468.

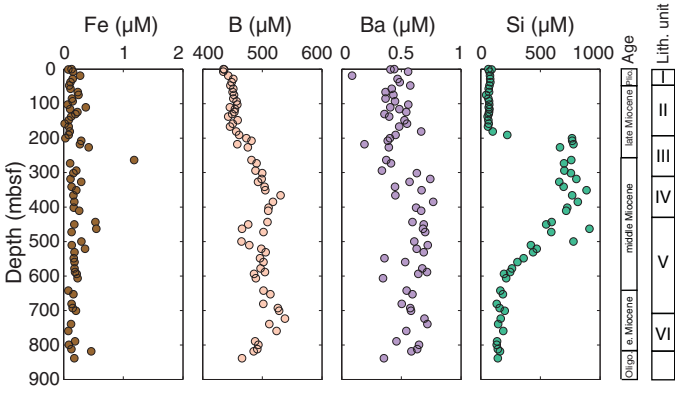

Bulk sediment geochemistry

X-ray diffraction

Mineralogy was determined at a rate of approximately one sample per core, with additional material supplied on an ad hoc basis. In

the upper ~40 mbsf, coincident with Unit I, the sediments consist of between 20% and 50% aragonite, with the remainder being composed of low-Mg calcite (LMC) (Figure **F31**; Table **T8**). Below this depth, dolomite comprises up to 15% of the sediment along with a small amount of aragonite (<5%). The remainder of the sediment is LMC. At the bottom of lithostratigraphic Unit II, dolomite concentrations decrease and aragonite increases. Dolomite disappears at the base of Unit IV and is largely absent throughout the remainder of the hole. Celestine is present in samples from 180.78 and 217.7 mbsf. Throughout this interval, the pore waters are saturated with respect to $SrSO_4$.

Calcium carbonate

Carbonate content was determined at a rate of three samples per core, and organic carbon was determined at a rate of one sample per core. In total, 193 samples were analyzed. The majority of the data lie between 85 and 99 wt% (Figure **F32**; Table **T9**). Despite relatively high carbonate contents, some lithostratigraphic units have distinctive values and some are delineated by abrupt concentration changes. Other changes in carbonate content appear to occur without any correlation to changes in the lithostratigraphic units.

Organic carbon

Total organic carbon concentrations were measured on one sample per core and range between <0.1 and 2.8 wt% (Figure **F32**; Table **T9**). Numerous samples have calculated organic concentrations of less than zero. This value is an artifact of the inadequate method of determining the amount of organic carbon in carbonate-rich sediments (see the **Expedition 359 methods** chapter [Betzler et al, 2017a]). The highest values were in lithostratigraphic Unit II, and an increase was coincident with the lithostratigraphic Unit I/II, II/III, IV/V, and V/VI boundaries.

Total nitrogen was low, averaging 0.10 wt% with a maximum of 0.13 wt%. As a result of the persistent negative percent organic carbon, no attempt was made to calculate the C:N ratio.

Major, minor, and trace element composition

Minor and trace element composition was measured on sediments from all IW squeeze cakes from Hole U1468A. The most important elements relevant to carbonate diagenesis (Sr, Mg, Fe, and Mn) are presented in Figure **F33** as molar ratios relative to calcium.

Strontium and magnesium

The Sr/Ca ratios are relatively high in the Pliocene–Pleistocene portion of the core and decrease downhole (Figure **F33**). The Mg/Ca ratios are approximately 10 mmol/mol but increase below 50 mbsf and remain elevated to ~350 mbsf. Below 400 mbsf, ratios decrease to less than 10 mmol/mol.

Manganese and iron

The Mn/Ca and Fe/Ca ratios are higher in the Pliocene–Pleistocene portion of the core (above 50 mbsf), ranging from 40 to 100 µmol/mol (Figure **F33**). The ratios decrease to between 30 and 50 µmol/mol between 50 and 400 mbsf. The Fe/Ca ratios increase between 400 and 500 mbsf, coincident with a region with a relative lower amount of carbonate and subsequently decrease to below 50 µmol/mol. The Mn/Ca ratios increase at the same interval to above 50 µmol/mol and remain elevated to the base of the cored interval.

Volatile hydrocarbons

Headspace samples for the analysis of methane, ethene, ethane, propene, and propane were taken from every Hole U1468A core, generally from the top of Section 5 when an IW sample was taken. Methane remains at concentrations between 1.5 and 5 ppmv and increases slightly with depth (Figure **F34**; Table **T10**). Ethane is only

Figure F31. Relative concentrations of LMC, high-Mg calcite (HMC), dolomite, aragonite, and quartz measured using XRD, Site U1468. Depths of dolomite peaks are indicated. Red symbols = celestine.

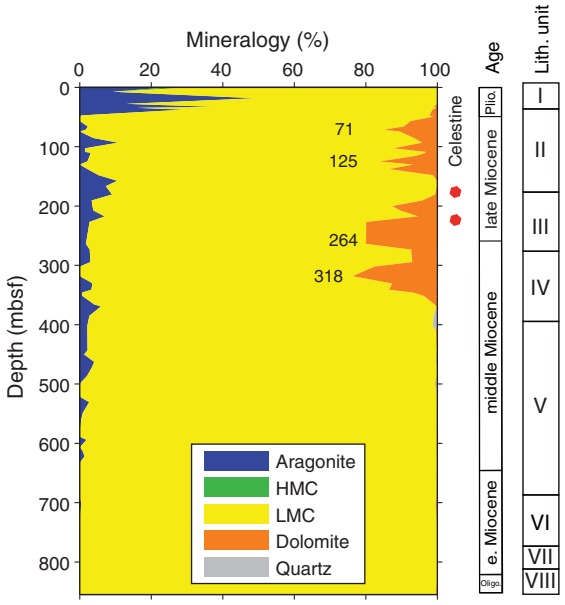

Table T8. XRD results, Site U1468. **Download table in .csv format.**

Figure F32. Carbonate and organic carbon contents, Hole U1468A.

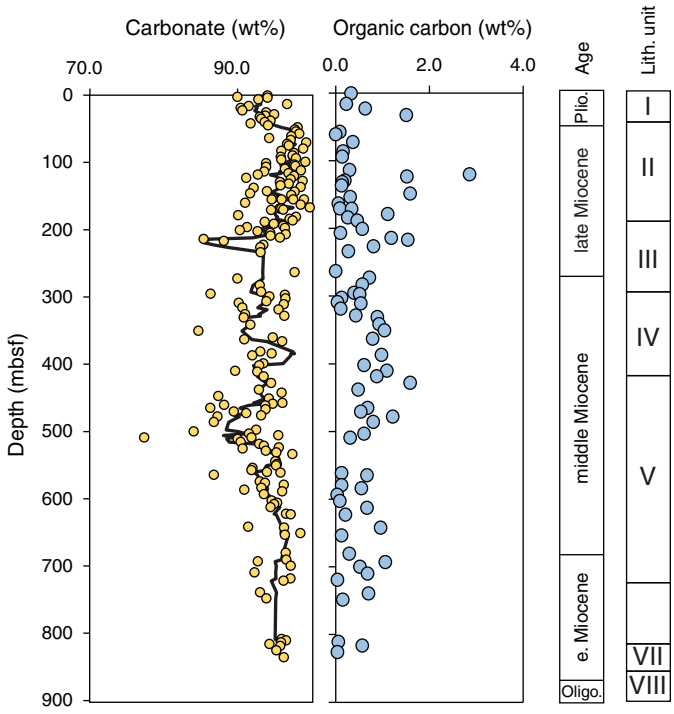

Table T9. Carbon and nitrogen, Site U1468. **Download table in .csv format.**

Figure F33. Mg/Ca, Sr/Ca, Fe/Ca, and Mn/Ca of sediments, Site U1468.

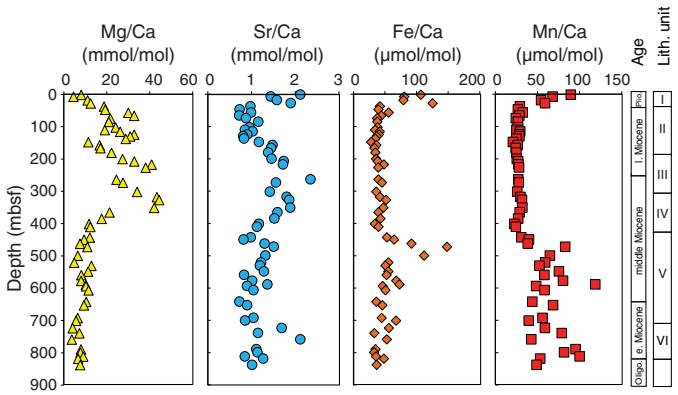

Figure F34. Headspace methane, ethane, and ethene concentrations, Hole U1468A.

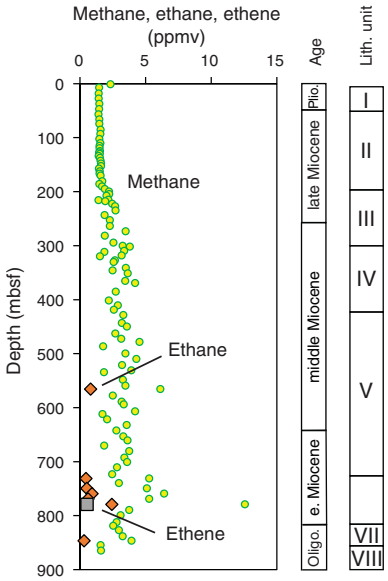

Table T10. Headspace hydrocarbons, Site U1468. **Download table in .csv format.**

present in measurable quantities in six cores. Ethene was detected in one sample.

Discussion

Interstitial pore water

The minimal changes in the SO_4^{2-}/Cl^- ratio and alkalinity of the interstitial fluids from the upper 200 mbsf of Site U1468 indicate either relatively low rates of organic matter remineralization or rates of advection by bottom seawater that are faster than the rates of decomposition of organic matter. Below 200 mbsf, a net decrease in SO_4^{2-} concentrations is caused by BSR. These changes are visible in the deficit of SO_4^{2-} and excess of alkalinity. In the absence of any other reactions involving carbonate ions, the increase in alkalinity should be two times the decrease in SO_4^{2-}. As shown in Figure **F27**, a decrease in excess SO_4^{2-} of approximately 4 mM should therefore produce an increase in alkalinity of 8 mM. However, the increase in alkalinity is only 1 mM, so 7 mM of alkalinity was consumed. Some of this loss is accounted for by the approximate 10 mM loss of Mg^{2+} and the 5 mM gain of Ca^{2+}. Changes in the concentrations of these elements occur as a result of dolomitization by the reaction shown in Equation **2**, in which Mg^{2+} is consumed and Ca^{2+} is produced. The extra Ca^{2+} produced in this reaction is then lost as LMC is precipitated (Equation **3**).

$$2CaCO_3 + Mg^{2+} = CaMg(CO_3)_2 + Ca^{2+}. \quad (2)$$

$$Ca^{2+} + HCO_3^- = CaCO_3 + H^+. \quad (3)$$

These reactions account for a further 5 mM of alkalinity, leaving only 2 mM to be reconciled. The difference might be associated with analytical uncertainty or unidentified diagenetic reactions involving clay minerals and/or organic materials.

An additional factor influencing the titration alkalinity is the abundance of NH_4^+, which should act to decrease carbonate alkalinity by 200–400 µM in the region of the core in which NH_4^+ concentrations are highest (Figure **F26**).

Aragonite concentrations remain between 20% and 40% throughout the Pleistocene (0–50 mbsf), reflecting variations in input rather than diagenetic change to LMC. Poor biostratigraphic control between the early Pleistocene and the middle Miocene makes interpretation of the diagenetic history problematic, but the sudden loss in aragonite below ~50 mbsf suggests either a period of exposure to meteoric fluids or one in which fluids caused partial dolomitization. In fact, peaks in dolomite concentration at 71, 125, 264, and 318 mbsf might suggest breaks in deposition slightly above these depths (Figure **F31**).

The rapid increase in the Sr^{2+}/Ca^{2+} ratios of pore water below 200 mbsf reflects the neomorphism of the sediments to LMC and some limited amount of dolomitization (Figure **F33**). Although dolomite formation is supported by the decline in the Mg^{2+}/Ca^{2+} ratio of the pore fluid, the present dolomite formation indicated by the pore water data is not responsible for the up to 25% dolomite found in the sediments (see **Geochemistry** in the Site U1466 chapter [Betzler et al, 2017d]). This dolomite must have formed during earlier time periods in a different fluid regime than observed at the present.

The large increase in Sr^{2+} in lithostratigraphic Unit III causes the pore fluids to attain saturation with respect to $SrSO_4$ (Figure **F35**), and although the presence of celestine was not noted in the sedimentology descriptions, it was detected using X-ray diffraction (XRD) in several of the samples analyzed from the squeezed sediments. Saturation of pore fluids relative to $SrSO_4$ was also observed at Sites U1466 and U1467.

Minor elemental chemistry

Variations in the Sr/Ca ratios reflect variations in the percentage of aragonite in the upper portion of the core, but the increase in Sr between 50 and 300 mbsf is produced by a combination of neomorphism from aragonite to calcite and some leaching of celestine (during the dissolution of the sample), which was present in several samples (Figure **F31**). Variations in Mg represent changes in the amount of dolomite in the upper 400 mbsf.

Changes in the Mn contents of pore waters and sediments are related to the redox state (see **Geochemistry** in the Site U1466 chapter [Betzler et al, 2017d]). Increases in the Mn/Ca ratios occur below 400 mbsf, coincident with the lithostratigraphic Unit IV–V transition. A similar increase was observed at Site U1466 in simi-

Figure F35. Ion activity product (IAP) of $SrSO_4$, Sites U1466–U1468.

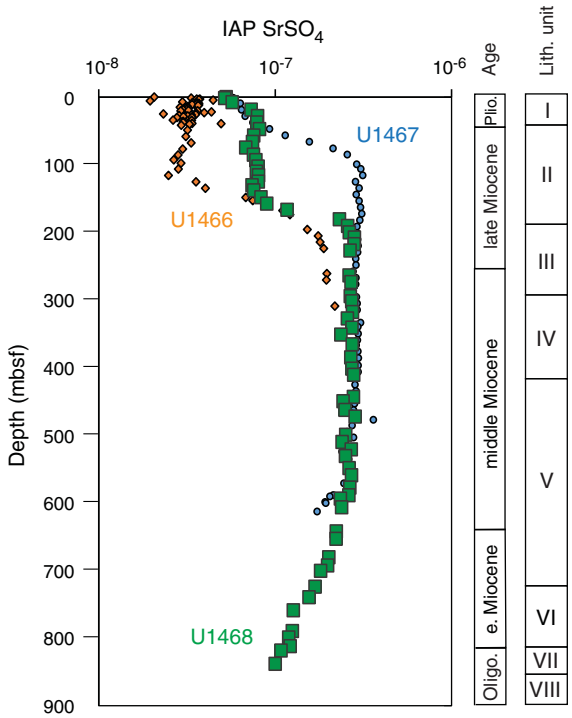

larly aged sediments and may be coincident with the development of the oxygen minimum zone (OMZ) as proposed by Dickens and Owen (1994).

Chloride, sodium, potassium, and other elements

Three contrasting types of behavior were noted in Cl^- concentrations in pore waters at the northern transect sites (U1466–U1468). At Site U1466, Cl^- concentrations initially increase rapidly, followed by a gradual increase to approximately 590 mM at the bottom of the hole. At Site U1467, concentrations initially increase rapidly to 590 mM, followed by a decline to near-seawater values throughout the remainder of the hole. At Site U1468, values increase rapidly to ~585 mM, followed by a gradual decline to the bottom of the hole (Figure **F25**). At Site U1468, it seems possible that the increase in Cl^- reflects an increase in salinity because Cl^- is strongly correlated with Na^+, another conservative element, and the ratio of these two elements is approximately what one would expect from seawater throughout the hole. At Site U1467, the increase in Cl^- might be related to the salinity increase during the last glacial period (Schrag and DePaolo, 1993), and although a similar explanation might be possible here, the difference in the nature of the decrease with increasing depth suggests that the signal is being masked by the presence of another water mass at depth, perhaps with a slightly higher salinity than at Site U1467.

As at Sites U1465 and U1466, poor correlation between elements such as K^+ and Na^+ and Cl^- results from the involvement of K^+ and Na^+ in clay mineral reactions. The presence of quartz and small amounts of clay minerals may account for the increase in Si in the pore fluids (Figure **F29**). The influence of noncarbonate components on pore water can be seen between 450 and 500 mbsf, where the carbonate content decreases to ~80 wt% (Figure **F30**). Here, the K^+ of the pore waters increases slightly (Figure **F25**). The increase in Fe and the marked increase in the Mn/Ca ratios below this depth clearly indicate the significance of this transition, which is reflected

Figure F36. NRM intensity, Hole U1468A. Typical drilling overprint is possibly removed. APC and HLAPC cores show intensity distribution skewed toward high values because of possible contamination. Note the very large range of intensities, which span six orders of magnitude. The intensity distribution for XCB cores appears less biased, suggesting less contamination.

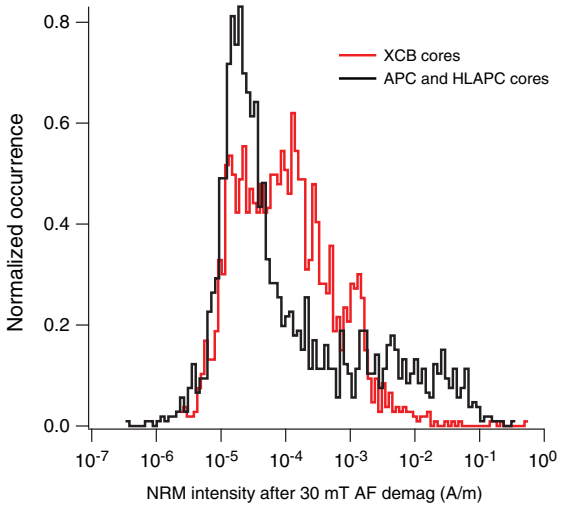

in the nature of the sediments (see **Lithostratigraphy**) and in a significant reduction in the rate of sedimentation (see **Biostratigraphy**).

Paleomagnetism

The natural remanent magnetization (NRM) from 41 APC and HLAPC cores and 56 XCB cores from Hole U1468A was routinely measured using the superconducting rock magnetometer (SRM). Cores were stepwise alternating field (AF) demagnetized up to 30 mT with two or three steps depending on core flow. The drilling overprint was removed after demagnetization at 10 or 15 mT, and "blanket" demagnetization at 30 mT was used to analyze the data. Unfortunately, core contamination with highly magnetic material persisted at Site U1468, and it is only slightly attenuated when compared to previous sites. This problem is unambiguously shown by the typical pattern of NRM intensity that decreases from the top to the bottom of each core by three or four orders of magnitude. Moreover, APC and HLAPC cores drilled in the upper part of Hole U1468A seem more affected by this problem compared to XCB cores drilled in the deepest part of the same hole, even though APC cores use nonmagnetic core barrels. A histogram of NRM intensity after demagnetization at 30 mT and the mode of NRM intensity for the two sets of core are shown in Figure **F36**.

Natural remanent magnetization and paleomagnetic results

Paleomagnetic directions from APC and HLAPC cores appear scattered, even after demagnetization at 30 mT, with very little to no consistency within each core (Figures **F37**, **F38**). None of the APC or HLAPC cores were oriented; however, the paleomagnetic directions are expected to be coherent (i.e., to have similar or antipodal inclinations and declinations) within the same core. We used this property to test the data quality and discard sections with highly dispersed directions. We proceeded by computing the Fisher (1953) mean direction in each section and evaluating the grouping by the α_{95} dispersion parameter. We discarded all sections with $\alpha_{95} > 45°$

Figure F37. NRM intensity, declination, and inclination on APC and HLAPC core sections, Hole U1468A. Circles = Fisher (1953) mean direction of each section. Inset shows magnetization intensity details, highlighting core breaks and the typical pattern of contamination that peaks at the top of each core.

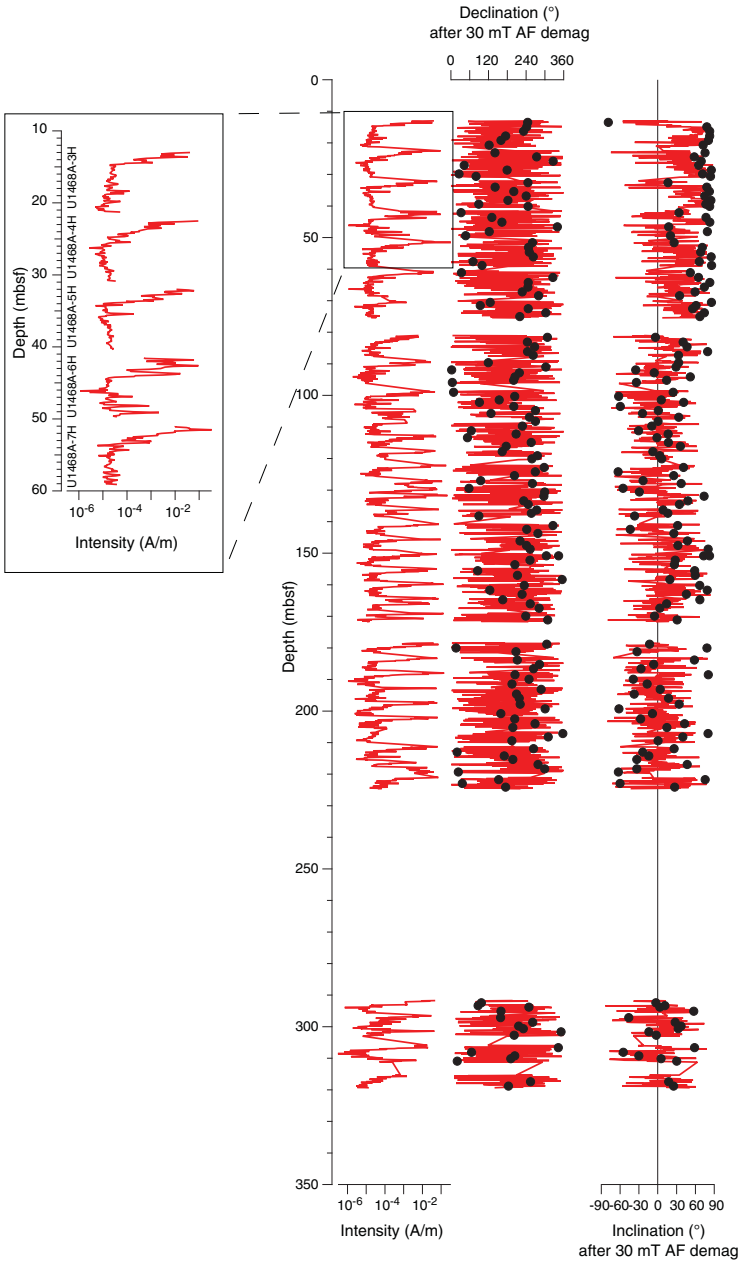

and, although this is not a stringent quality constraint, we were left with only 20 sections out of the initial 155. Most of these 20 sections showed subvertical mean directions and are not considered reliable paleomagnetic records of subequatorial Site U1468. The only four sections that had acceptable mean directions were insufficient for magnetostratigraphic purposes.

XCB cores carry no information on declination, even within the same core, since core "biscuits" (a typical core disturbance observed in XCB cores) are rotated with respect to each other, making it difficult to judge data quality. In general, however, these cores appear less affected by contamination and have nonrandom inclinations (Figures **F39**, **F40**). Our attempt to interpret the inclinations as a record of polarity was impaired by the data scatter and the subequatorial paleolatitude of this site (e.g., Torsvik et al., 2012). The distribution of inclinations, despite the large scatter, has in fact a single mode at 0°, suggesting that Site U1468 was crossing the Equator during the early Miocene.

Figure F38. A. Paleomagnetic directions after 30 mT "blanket" demagnetization for APC and HLAPC cores, Hole U1468A. By visual inspection, the direction appears scattered with no preferential orientation. B. Fisher (1953) mean paleomagnetic directions. C. Same as B after discarding those with α_{95} > 45°. Most of the remaining sections show steep downward directions that cannot be considered as a true record of geomagnetic field for this subequatorial site. The only four sections that pass this quality test (13H-2, 12H-6, 46F-1, and 15F-3) are insufficient to establish magnetostratigraphy.

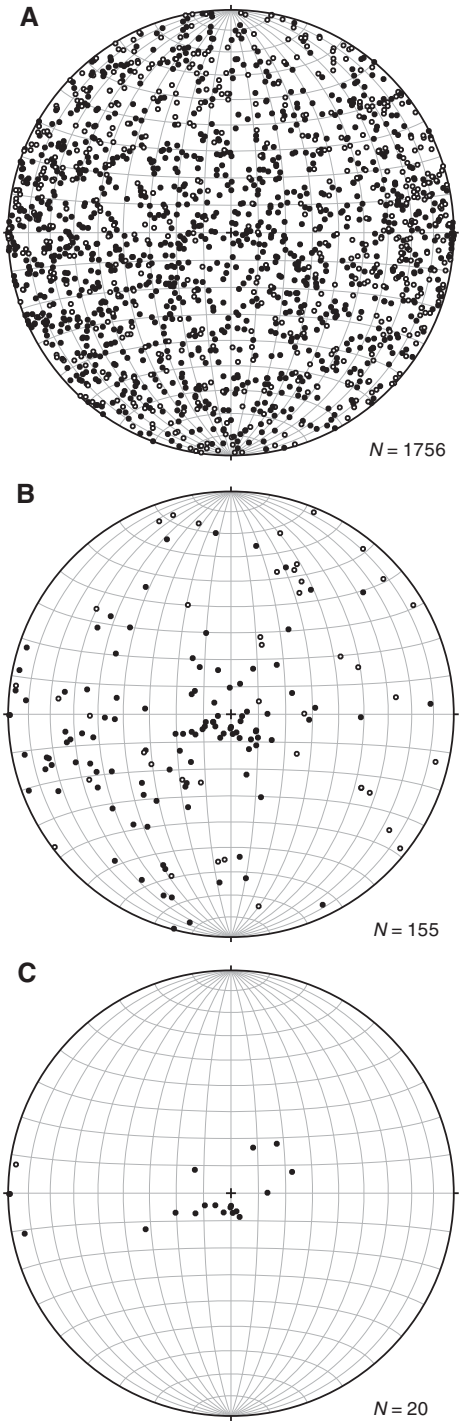

Figure F39. Paleomagnetic measurements of intensity and inclination of XCB core sections, Hole U1468A. Solid black circles = angular mean inclinations computed for each core section, open circles = angular mean values of the vertical component of the normalized directions, error bars = standard deviation.

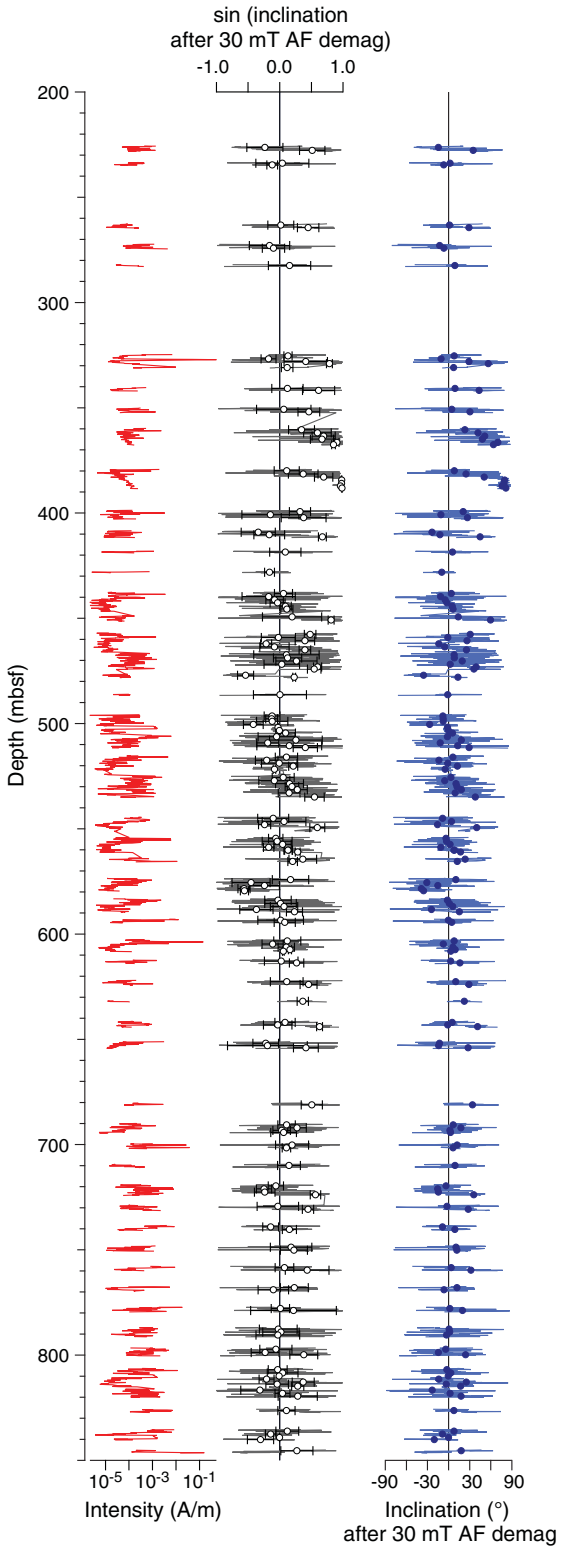

Figure F40. Inclinations of XCB cores deeper than 400 mbsf after AF demagnetization at 30 mT, Hole U1468A. Inclinations are distributed throughout the entire range, but distribution is not uniform and has a single mode at 0° as expected for this subequatorial latitude during the early Miocene. This distribution suggests that, although not usable for magnetostratigraphy, the paleomagnetic record might be partially preserved.

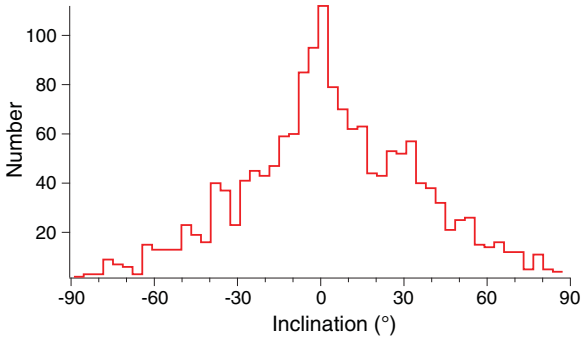

Physical properties

Physical properties measured at Site U1468 include natural gamma radiation (NGR), gamma ray attenuation (GRA) density, magnetic susceptibility (MS), color reflectance, shear strength, thermal conductivity, and *P*-wave velocity. Based on variations in physical properties, especially NGR and density, the sedimentary formation at this site is divided into five petrophysical (PP) units (Figure **F41**). Unit 1 extends from the seafloor to ~50 mbsf. Unit 2 (~50 to ~478 mbsf) includes four subunits: 2A (~50–106 mbsf), 2B (~106–216 mbsf), 2C (~216–418 mbsf), and 2D (~418–478 mbsf). Unit 3 (~478 to ~730 mbsf) consists of two subunits: 3A (~478–604 mbsf) and 3B (~604–730 mbsf). Unit 4 spans 730 to ~807 mbsf. Unit 5 is a short interval extending from ~807 mbsf to the bottom of this site at ~820 mbsf.

Natural gamma radiation

Downcore NGR variations correspond with and sometimes define the petrophysical unit boundaries at Site U1468. In Unit 1 (0 to ~50 mbsf), NGR decreases from ~70 counts/s at the top to ~10–20 counts/s at the base (Figure **F41**). The Unit 1/2 boundary at 50 mbsf is marked by an increase in NGR to ~20–30 counts/s. Within Unit 2, Subunit 2A has higher NGR, mostly varying from ~20 to 35 counts/s. A distinct decrease in NGR at 105 mbsf marks the Subunit 2A/2B boundary. Subunit 2B/2C boundary is placed at 171 mbsf where NGR records an intermediate peak. Unit and subunit boundaries below this level rely more on variability because core recovery decreased. NGR in Subunit 2D (~430–480 mbsf) shows greater variability and ranges from ~10 to 40 counts/s with no apparent trend. Subunit 3A (480–605 mbsf) NGR values remain relatively constant with low variability. Below this level, NGR variability increases throughout Subunit 3B and Unit 4. Several peaks, each with higher counts per second, occur downhole with the last and highest peak at ~807 mbsf. NGR values remain low (<20 counts/s) with no trend in Unit 5.

Density and porosity

GRA density measurements performed on whole-round cores were highly variable because incompletely filled core liners recorded the density of the water in the cores. Thus, only measurements above 1.4 g/cm^3 are displayed in Figure **F41**. Wet bulk density values determined from discrete samples basically agree with the "cleaned" GRA measurements. Bulk density in Unit 1 is low, ranging from ~1.4 to 1.6 g/cm^3. A sharp shift toward higher values (>1.8 g/cm^3) at the bottom of this interval marks the Unit 1/2 boundary, where bulk density values vary between ~1.7 and 2.0 g/cm^3 with a small increasing trend through Subunits 2A and 2B to ~215 mbsf. Further downhole, bulk density values vary between ~1.8 and 2.0 g/cm^3 to the base of Unit 5. Grain density values are constant with depth and average ~2.74 g/cm^3 except for a few relatively high (>2.9 g/cm^3) or low (<2.65 g/cm^3) values at ~80–220 mbsf. The low values might be from organic-rich sediments or cores contaminated with drilling mud. The high values might be from admixture of the mineral celestine, which has a very high density of 3.9 g/cm^3 and was found at other sites of the Inner Sea.

Porosity inversely correlates with bulk density (Figure **F41**). In Unit 1, porosity decreases rapidly from 80% to 60%. To the base of Subunit 2B (~216 mbsf), porosity values vary in a relatively wide range of ~40%–60% without a downcore trend. Below Subunit 2B, porosity gradually decreases from ~50% to 40% at the bottom of Unit 5. Low porosity (~40%) at ~360–430 mbsf coincides with the relatively high bulk density in the same interval. Porosity is relatively high (>50%) at ~480–550 and ~720–820 mbsf, the same intervals characterized by low bulk density values.

P-wave velocity

P-wave velocities for whole-round cores were measured on the Whole-Round Multisensor Logger (WRMSL); split cores and discrete samples taken for paleomagnetism were measured on the Section Half Measurement Gantry (SHMG; *P*-wave caliper [PWC]). Poor coupling between the core and the liner prevented accurate measurement of wave velocities in partly lithified and lithified successions with the WRMSL. As a result, *P*-wave velocities measured using the WRMSL are usually lower than those measured on discrete samples or split cores. *P*-wave velocity varies with depth (Figure **F41**) with greater variability above Subunit 2D (~428 mbsf) than below. Seven peaks are distinguishable by high velocity values (>2500 m/s) at 53, 166, 171, 214, 298, 328, and 428 mbsf. However, there are no corresponding changes in porosity and/or density. Except for these peaks, *P*-wave velocity slightly decreases from ~2000 m/s at ~50 mbsf to ~1700 m/s at ~200 mbsf and then increases rapidly to ~2100 m/s at ~400 mbsf followed by a more gradual increase to ~2400 m/s at ~730 mbsf. The chalk in Unit 4 has a relatively low velocity of ~1800 m/s. Unit 5 *P*-wave velocities range from ~2000 to 2200 m/s.

Color reflectance

Reflectance values of L*, a*, and b* vary moderately with depth (Figure **F42**). At ~50 mbsf, L* and a* increase. L* ranges from ~20 to 80. Parameters a* and b* show relatively narrow ranges of ~0 to 5 and approximately –10 to 5, respectively. The variation of reflectance parameter L* coincides with a* from the seafloor to ~500 mbsf but is opposite of b* from the seafloor to ~730 mbsf. From ~730 to 809 mbsf, L*, a*, and b* exhibit somewhat greater variation; for example, L* is characterized by some low (<20) and high (>80) values.

Magnetic susceptibility

Most magnetic susceptibility loop (MSL or WRMSL MS) values are very low, ranging from –4 to 2 IU, and magnetic susceptibility point (MSP or Section Half Multisensor Logger [SHMSL] MS)

Figure F41. NGR, bulk density, grain and dry density, porosity, and *P*-wave velocity, Site U1468. Erroneous low GRA density values are filtered out, and only the upper bounds of the values are displayed. PWL = *P*-wave logger.

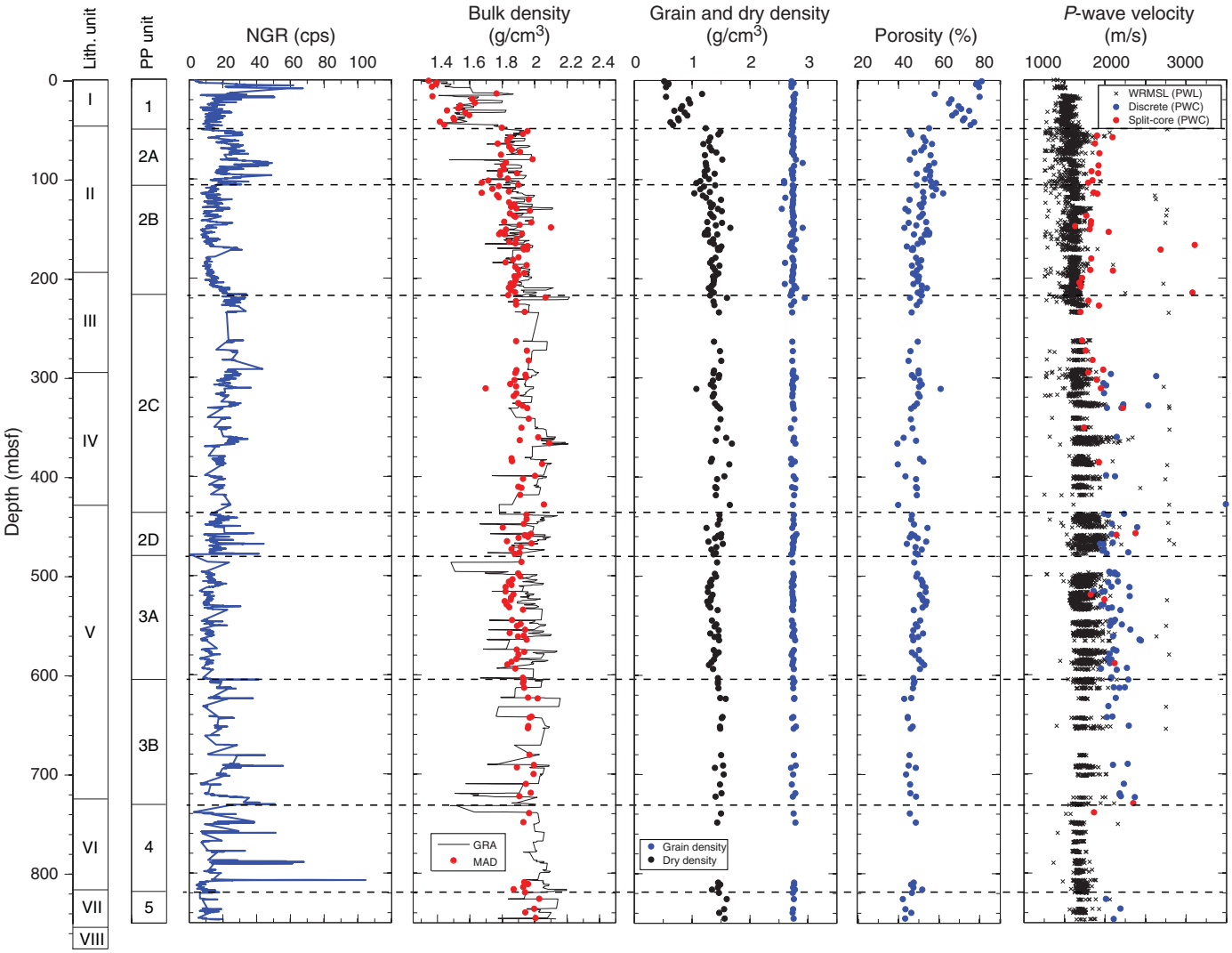

ranges from –15 to –5 (Figure **F42**). In the uppermost 50 m, both MSL and MSP generally display a slightly decreasing trend. MSL then remains constant to the bottom of the site, whereas MSP gradually shifts slightly toward higher values at ~430–480 mbsf and then remains constant downhole.

Magnetic susceptibility measurements are very similar to those from Sites U1465–U1467. As at all sites, coring-related contamination caused some peaks with very high values (>100 IU) at the top of each core in both the MSL and MSP profiles, especially below ~448 mbsf. Raw magnetic susceptibility data were therefore filtered to remove very high values.

Thermal conductivity

At Site U1468, thermal conductivity ranges between 0.926 and 1.521 W/(m·K) with a mean of 1.307 W/(m·K) and a standard deviation of 0.139 W/(m·K) (Figure **F43**; Table **T11**). In general, thermal conductivity increases rapidly from 0.9 to 1.16 W/(m·K) above ~83 mbsf and more gradually below ~83 mbsf to 1.5 W/(m·K) at the bottom of Site U1468 with many fluctuations. Fluctuation lows are found in Subunit 2C (~216–418 mbsf) and at ~35, 100–110, 480, 545–565, 644, 730–740, and 808 mbsf. Fluctuation highs were observed at ~93 and 298 mbsf. (Thermal conductivity values are reported as the average of three measurements at every measuring position. Standard deviations for the three measurements at each position vary from 0.001 to 0.388 W/[m·K].)

Shear strength

Shear strength was determined only on soft sediments with minor coring disturbance from Hole U1468A using the manual Torvane shear device. Six measurements were conducted in the upper ~300 m (Figure **F43**). Unconfined shear strength ranges from ~50 to 175 N/m^2 with higher values at depth.

Discussion

The petrophysical units at this site are well characterized by the variation of physical properties, especially NGR. Most unit and subunit boundaries are consistent with either NGR peaks or shifts toward higher values. Sediment deposition in this drilling area is greatly affected by sea level fluctuations and changes in current regime (Betzler et al., 2013b; Lüdmann et al., 2013). Therefore, the transitions from high to low NGR values might correspond to changes to low sea level or weak current during periods with a re-

Figure F42. Color reflectance and magnetic susceptibility, Site U1468.

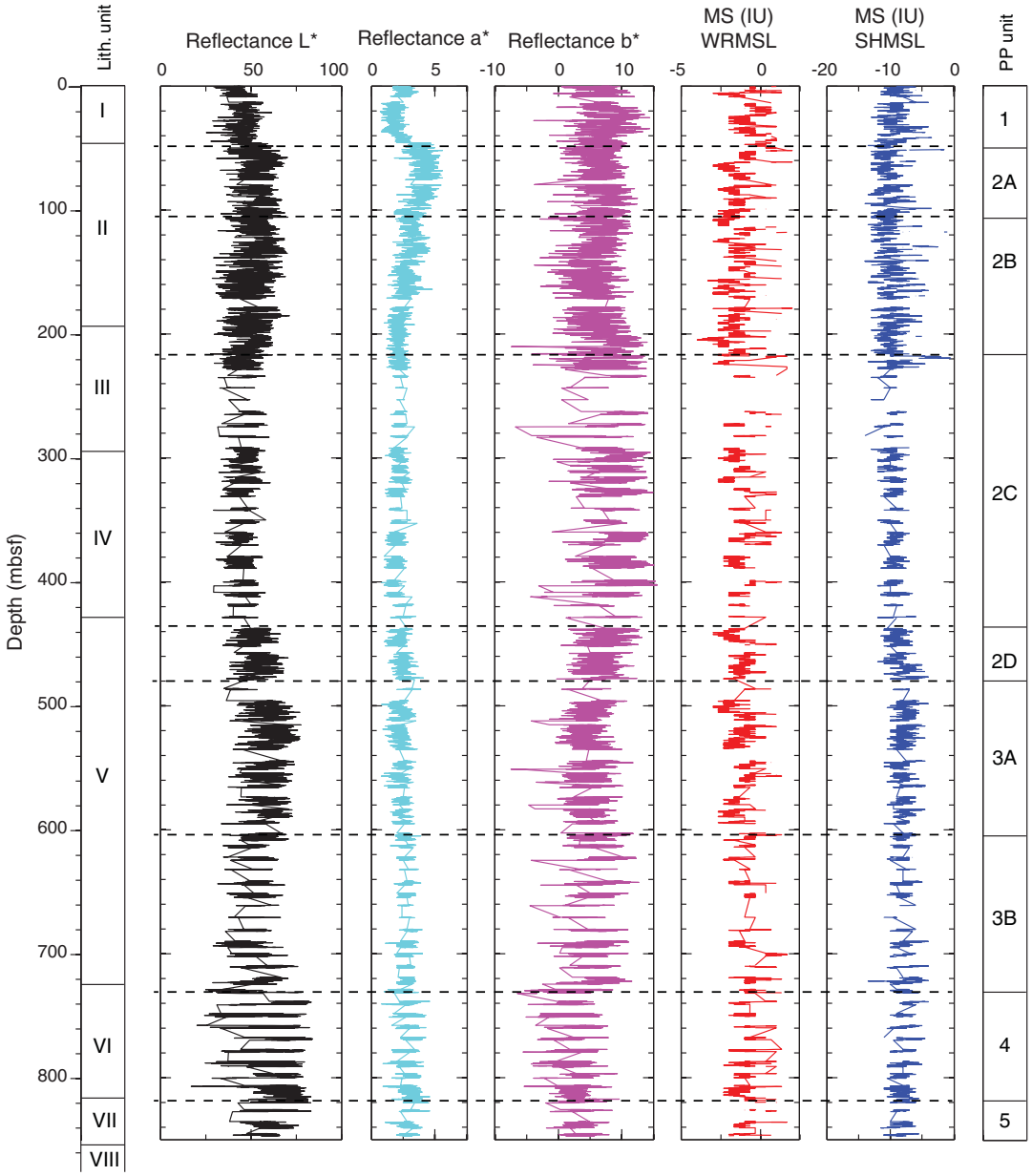

duced supply of carbonates shed from the tops of the carbonate platforms.

The variation of physical properties represents the interplay between different depositional environments and diagenetic processes. In the uppermost portion of Unit 1, sediments have high porosity and low bulk density, indicating they are unconsolidated and highly saturated with pore water. In Unit 2, *P*-wave velocity shows no correlation with bulk density and porosity at ~50–200 mbsf, strongly suggesting that sediment cementation starts in this interval. Scattered and relatively constant trends for bulk density and porosity in the upper portion (~50–200 mbsf) of Unit 2 contrast with the gradual increase or decrease in the same interval at Site U1466. High *P*-wave velocities (>2500 m/s) reflect partial lithification in the drift sediments at this site. In Unit 3, bulk density and porosity gradually increase and *P*-wave velocity slowly increases with depth. High *P*-wave velocities in Unit 2 are located close to the more lithified unit or subunit boundaries (Figure **F41**), likely related to submarine cementation during low sea level when sedimentation rate was reduced (Malone et al., 2001).

Alternating dark and light layers were recovered at the base of Sites U1466–U1468 in which dark layers are organic rich (see **Lithostratigraphy**). Downhole logging at Site U1467 indicated that the major carrier of NGR signals is uranium from organic carbon (see **Downhole measurements** in the Site U1467 chapter [Betzler et al, 2017e]). Organic carbon might also have affected the limited measurements on cores from Unit 4. In the chalky white layers, moisture and density (MAD) points and WRMSL *P*-wave velocities indicate bulk density decreases, porosity increases, and potential velocity decreases in Unit 4.

Figure F43. Thermal conductivity and sediment strength, Site U1468.

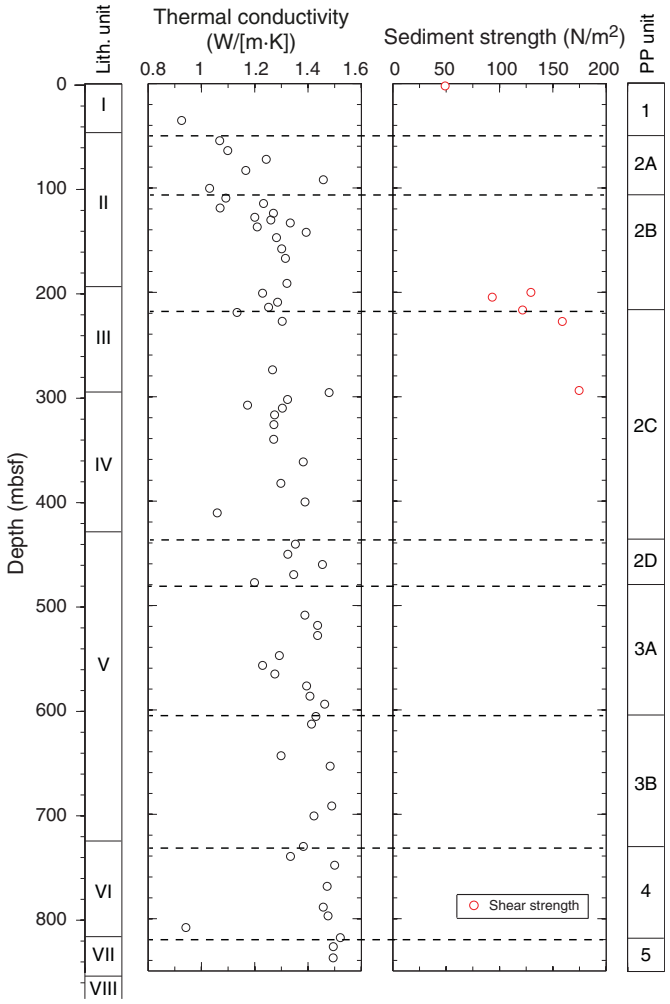

Table T11. Thermal conductivity (TC), Site U1468. NA = not applicable. (Continued on next 2 pages.) **Download table in .csv format.**

Core, section	Depth CSF-A (m)	TC measurement (W/[m·K])	TC mean (W/[m·K])	TC standard deviation (W/[m·K])	Rock type
359-U1468A-					
5H-3	35.320	0.950	0.926	0.026	Soft
5H-3	35.320	0.898			Soft
5H-3	35.320	0.929			Soft
7H-3	54.650	1.046	1.069	0.021	Soft
7H-3	54.650	1.086			Soft
7H-3	54.650	1.074			Soft
8H-3	64.150	1.099	1.099	NA	Soft
9H-3	72.520	1.246	1.243	0.004	Soft
9H-3	72.520	1.239			Soft
9H-3	72.520	1.245			Soft
10H-3	83.150	1.158	1.167	0.012	Soft
10H-3	83.150	1.175			Soft
11H-3	92.090	1.879	1.458	0.388	Soft
11H-3	92.090	1.114			Soft
11H-3	92.090	1.380			Soft
12H-2	100.340	1.022	1.031	0.009	Soft
12H-2	100.340	1.039			Soft
12H-2	100.340	1.031			Soft
13H-3	109.680	1.082	1.092	0.009	Soft
13H-3	109.680	1.093			Soft
13H-3	109.680	1.100			Soft
14F-2	114.850	1.251	1.233	0.016	Soft
14F-2	114.850	1.226			Soft
14F-2	114.850	1.222			Soft
15F-2	119.090	1.069	1.070	0.005	Soft
15F-2	119.090	1.066			Soft
15F-2	119.090	1.076			Soft
16F-2	124.250	1.357	1.270	0.076	Soft
16F-2	124.250	1.232			Soft
16F-2	124.250	1.221			Soft
17F-2	127.990	1.187	1.200	0.013	Soft
17F-2	127.990	1.212			Soft
17F-2	127.990	1.202			Soft
18F-2	130.700	1.237	1.260	0.020	Soft
18F-2	130.700	1.275			Soft
18F-2	130.700	1.269			Soft
19F-2	133.450	1.342	1.333	0.008	Soft
19F-2	133.450	1.332			Soft
19F-2	133.450	1.326			Soft
20F-2	137.300	1.209	1.210	0.001	Soft
20F-2	137.300	1.209			Soft
20F-2	137.300	1.211			Soft
21F-2	142.490	1.572	1.393	0.155	Soft
21F-2	142.490	1.302			Soft
21F-2	142.490	1.305			Soft

Table T11 (continued). (Continued on next page.)

Core, section	Depth CSF-A (m)	TC measurement (W/[m·K])	TC mean (W/[m·K])	TC standard deviation (W/[m·K])	Rock type
22F-2	147.550	1.310	1.282	0.025	Soft
22F-2	147.550	1.263			Soft
22F-2	147.550	1.272			Soft
24F-3	158.310	1.336	1.301	0.030	Soft
24F-3	158.310	1.281			Soft
24F-3	158.310	1.286			Soft
26F-3	167.430	1.326	1.315	0.010	Soft
26F-3	167.430	1.307			Soft
26F-3	167.430	1.313			Soft
30F-3	191.350	1.294	1.321	0.024	Soft
30F-3	191.350	1.337			Soft
30F-3	191.350	1.332			Soft
32F-3	200.800	1.280	1.230	0.045	Soft
32F-3	200.800	1.214			Soft
32F-3	200.800	1.195			Soft
34F-3	209.430	1.285	1.286	0.006	Soft
34F-3	209.430	1.292			Soft
34F-3	209.430	1.280			Soft
35F-3	214.230	1.247	1.252	0.005	Soft
35F-3	214.230	1.252			Soft
35F-3	214.230	1.257			Soft
37F-3	219.240	1.145	1.133	0.012	Soft
37F-3	219.240	1.122			Soft
37F-3	219.240	1.133			Soft
39X-2	227.730	1.305	1.303	0.006	Soft
39X-2	227.730	1.296			Soft
39X-2	227.730	1.308			Soft
44X-2	274.160	1.264	1.267	0.006	Soft
44X-2	274.160	1.274			Soft
44X-2	274.160	1.263			Soft
47F-2	298.650	1.587	1.483	0.148	Soft
47F-2	298.650	1.378			Soft
48F-2	302.600	1.353	1.323	0.026	Soft
48F-2	302.600	1.306			Soft
48F-2	302.600	1.310			Soft
49F-2	308.050	1.036	1.173	0.121	Soft
49F-2	308.050	1.267			Soft
49F-2	308.050	1.216			Soft
50F-1	310.900	1.298	1.304	0.008	Soft
50F-1	310.900	1.310			Soft
51F-2	317.300	1.272	1.275	0.004	Soft
51F-2	317.300	1.277			Soft
53X-2	326.710	1.269	1.272	0.013	Soft
53X-2	326.710	1.286			Soft
53X-2	326.710	1.261			Soft
55X-1	340.750	1.269	1.271	0.036	Soft
55X-1	340.750	1.236			Soft
55X-1	340.750	1.308			Soft
59X-3	362.400	1.382	1.382	NA	Soft
61X-3	382.900	1.288	1.298	0.014	Soft
61X-3	382.900	1.308			Soft
63X-2	400.800	1.388	1.389	0.001	Soft
63X-2	400.800	1.390			Soft
63X-2	400.800	1.389			Soft
64X-3	411.260	1.065	1.059	0.005	Soft
64X-3	411.260	1.057			Soft
64X-3	411.260	1.056			Soft
67X-3	441.250	1.377	1.353	0.025	Soft
67X-3	441.250	1.354			Soft
67X-3	441.250	1.327			Soft
68X-3	450.800	1.324	1.324	NA	Soft
69X-3	460.620	1.463	1.454	0.013	Soft
69X-3	460.620	1.445			Soft
70X-3	470.340	1.379	1.346	0.040	Soft
70X-3	470.340	1.302			Soft
70X-3	470.340	1.358			Soft
71X-2	478.030	1.238	1.199	0.036	Soft
71X-2	478.030	1.193			Soft
71X-2	478.030	1.167			Soft
74X-3	509.200	1.388	1.388	NA	Soft
75X-3	518.950	1.438	1.436	0.006	Soft
75X-3	518.950	1.440			Soft
75X-3	518.950	1.429			Soft
76X-3	528.680	1.433	1.436	0.003	Soft
76X-3	528.680	1.438			Soft
76X-3	528.680	1.437			Soft
78X-3	547.980	1.292	1.292	0.007	Soft
78X-3	547.980	1.286			Soft
78X-3	547.980	1.299			Soft
79X-3	557.340	1.303	1.230	0.068	Soft
79X-3	557.340	1.216			Soft
79X-3	557.340	1.170			Soft
80X-2	565.580	1.299	1.275	0.030	Soft
80X-2	565.580	1.242			Soft
80X-2	565.580	1.285			Soft
81X-3	576.970	1.405	1.395	0.009	Soft
81X-3	576.970	1.387			Soft
81X-3	576.970	1.392			Soft
82X-3	586.810	1.437	1.407	0.027	Soft
82X-3	586.810	1.401			Soft
82X-3	586.810	1.383			Soft
83X-2	594.450	1.462	1.463	0.002	Soft
83X-2	594.450	1.461			Soft
83X-2	594.450	1.465			Soft
84X-3	606.240	1.439	1.429	0.011	Soft
84X-3	606.240	1.417			Soft
84X-3	606.240	1.432			Soft
85X-2	613.600	1.410	1.413	0.003	Soft
85X-2	613.600	1.415			Soft
85X-2	613.600	1.414			Soft
88X-3	643.900	1.298	1.299	0.003	Soft
88X-3	643.900	1.302			Soft
88X-3	643.900	1.297			Soft
89X-3	653.820	1.485	1.483	0.003	Soft
89X-3	653.820				Soft
89X-3	653.820	1.481			Soft
93X-2	692.000	1.471	1.489	0.025	Soft
93X-2	692.000				Soft
93X-2	692.000	1.507			Soft
94X-2	701.500	1.399	1.422	0.021	Soft
94X-2	701.500	1.440			Soft
94X-2	701.500	1.428			Soft
97X-2	730.780	1.379	1.382	0.004	Soft
97X-2	730.780	1.381			Soft
97X-2	730.780	1.387			Soft
98X-2	740.330	1.325	1.334	0.009	Soft
98X-2	740.330	1.335			Soft
98X-2	740.330	1.342			Soft
99X-1	748.750	1.493	1.500	0.008	Soft
99X-1	748.750	1.508			Soft
99X-1	748.750	1.499			Soft
101X-2	768.900	1.447	1.472	0.021	Soft
101X-2	768.900	1.484			Soft
101X-2	768.900	1.484			Soft
103X-2	788.310	1.462	1.457	0.008	Soft
103X-2	788.310	1.448			Soft
103X-2	788.310	1.462			Soft
104X-1	797.250	1.474	1.475	0.006	Soft
104X-1	797.250	1.481			Soft
104X-1	797.250	1.470			Soft
105X-2	808.450	0.941	0.942	0.002	Soft
105X-2	808.450	0.940			Soft
105X-2	808.450	0.944			Soft
106X-2	818.150	1.526	1.521	0.007	Soft
106X-2	818.150	1.513			Soft
106X-2	818.150	1.525			Soft

Table T11 (continued).

Core, section	Depth CSF-A (m)	TC measurement (W/[m·K])	TC mean (W/[m·K])	TC standard deviation (W/[m·K])	Rock type
107X-1	826.800	1.495	1.495	NA	Soft
107X-1	826.800				Soft
107X-1	826.800				Soft
108X-2	837.500	1.491	1.494	0.009	Soft
108X-2	837.500	1.488			Soft
108X-2	837.500	1.504			Soft

Downhole measurements

Logging operations

Logging operations for Site U1468 began on 13 November 2015 after drilling logging-dedicated Hole U1468B to a total depth of 874.7 m drilling depth below seafloor (DSF). In preparation for logging, the hole was swept with 30 bbl of high-viscosity mud, and the 9⅞ inch tricone bit used for drilling was released near the bottom of the hole. The drill pipe was raised to 140.5 m DSF, somewhat deeper than at previous sites, to isolate sandy zones identified during coring in Hole U1468A. The drilling process was relatively smooth, so logging operations were carried out with seawater as the logging fluid. The sea state was calm throughout logging operations; the wireline heave compensator was not used.

The full triple combo tool string, measuring total and natural gamma ray, porosity, density, electrical resistivity, and magnetic susceptibility, was rigged up and run into the borehole at 0240 h on 13 November (Figure **F44**). A downlog was recorded from just above the seafloor, with the tool string in the pipe, to a total depth of 1368 m wireline depth below rig floor (WRF; 835 m wireline depth below seafloor, WSF). The tool string tagged solid material at that depth, approximately 40 m shallower than the total drilled depth, indicating that infill had accumulated at the bottom of the hole. A short upward pass was made over the lower 100 m of the hole to show the repeatability of tool measurements. The tool string was run back down, and the main logging pass was recorded upward from the bottom of the hole at a speed of 365 m/h. At 485 m WSF, wireline tension increased and the Hostile Environment Litho-Density Sonde (HLDS) caliper measurement indicated a very narrow borehole (<7 inches in diameter). Wireline tension continued to increase, and caliper readings indicated that the hole was significantly undergauge as the tool string was pulled upward. These measurements suggest that the borehole was collapsing through this interval or that unstable materials were falling down from a shallower section of the hole. The caliper was closed at 420 m WSF to reduce additional drag. These conditions continued to approximately 280 m WSF, at which point the wireline tension decreased to relatively normal values and the caliper could be opened again. Caliper readings indicated a variable hole diameter (6–15 inches) between 280 m WSF and the depth of the pipe, suggesting that this section of the borehole was also in the process of collapsing. The main pass was completed when the tool string was pulled up past the seafloor. As a result of the deteriorating condition of the borehole in the short time period between the downlog, during which there was no evidence of borehole collapse, and the main upward mass, it was decided that no additional logging operations could be carried out safely in Hole U1468B. The triple combo tool string was pulled up to the rig floor and rigged down by 0855 h, and logging operations were completed by 0910 h.

Figure F44. Logging operations, Hole U1468B.

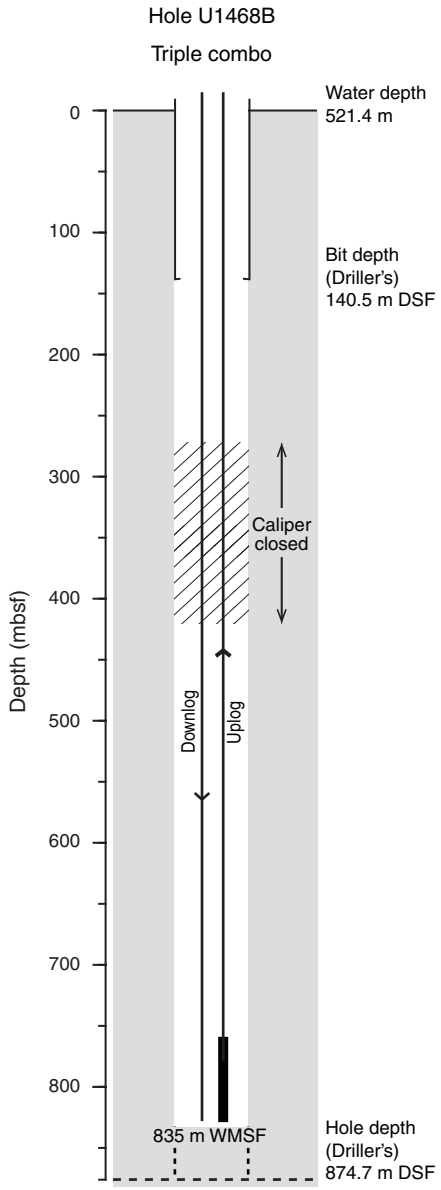

Downhole log data quality

During shore-based processing, all logging curves were depth-matched using the total gamma ray log from the downlog as a reference log and shifted to a seafloor depth reference, allowing a unified depth scale to be produced (wireline log matched depth below seafloor [WMSF]). Features in gamma ray logs from the main pass were aligned to the reference log to produce a complete depth-matched data set. Data were shifted to WMSF based on the depth of the step increase in gamma ray that indicated the seafloor during the downlog, measured at 532.5 m WRF.

In Hole U1468B, borehole conditions were variable, leading to logging data of variable quality. Borehole diameter was reasonable in the deeper section of the hole below the collapsed interval (Figure **F45**), with the exception of two washed out zones (centered at ~705 and ~772 m WMSF) and two narrow zones (at 445 and 482 m WMSF). Outside of those zones, the diameter ranged from bit size (~10 inches) to 15 inches. In the shallower section of the hole above

Figure F45. Triple combo logs, Hole U1468B. Note that downhole logs are on the logging depth scale, and NGR and magnetic susceptibility (WRMSL and MSP) core data from Hole U1466A and core recovery are on the core depth scale. HSGR = standard (total) gamma ray, GR EDTC = total gamma ray from EDTC. HRLA: R3 = medium resistivity, R5 = deepest resistivity, RT = true resistivity, modeled from all depths of investigation.

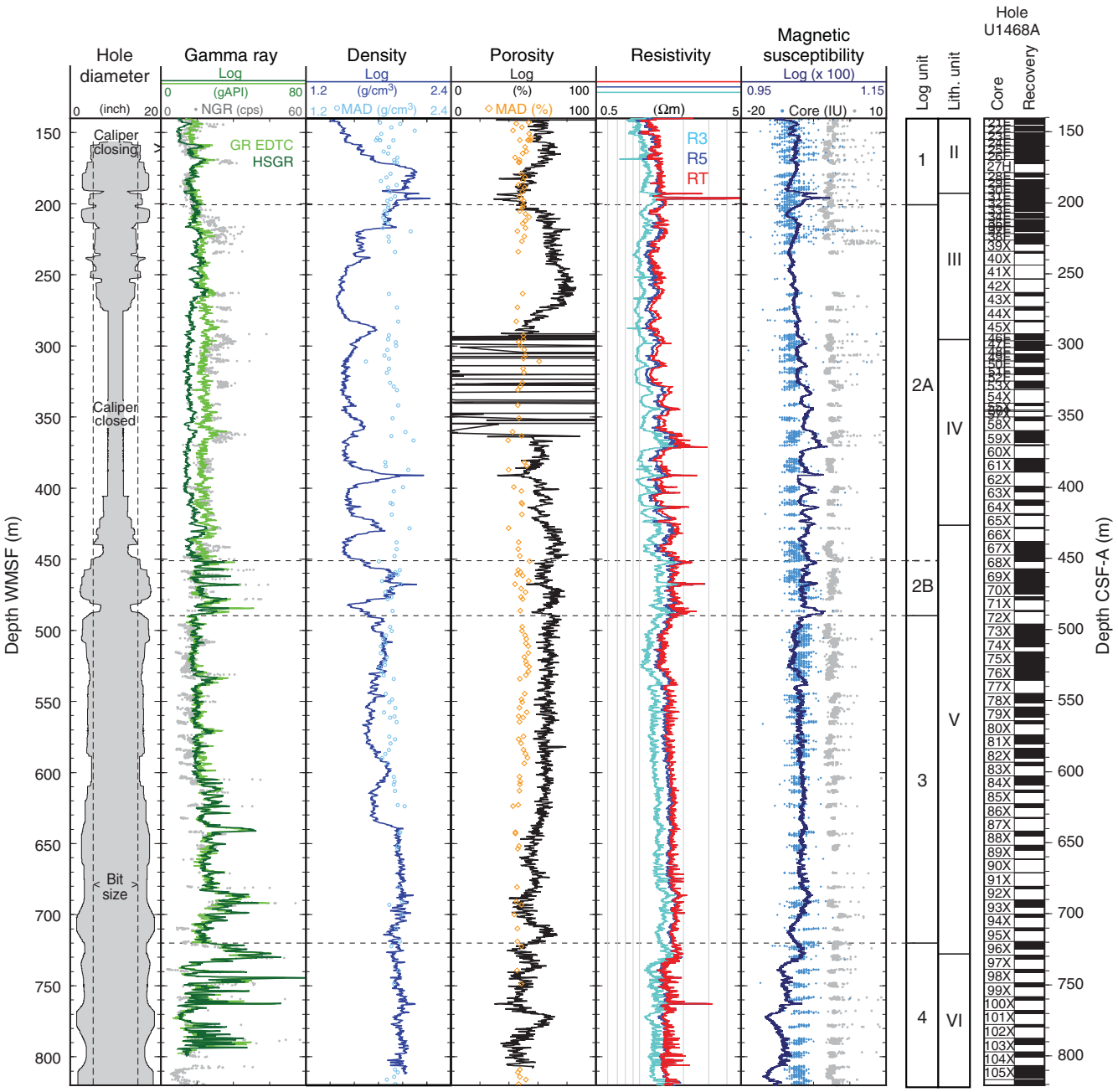

270 m WMSF, borehole diameter ranged from 5 to >17 inches over short depth intervals, likely reflecting the deterioration of the hole. Density and porosity measurements are negatively impacted by enlarged and variable borehole size, as those logging tools require decentralization and good contact with the borehole wall. Gamma ray, electrical resistivity, and magnetic susceptibility measurements are less affected by hole size. Despite the variable hole conditions, good repeatability was observed in those measurements between the downlog, repeat, and main passes with the triple combo tool string.

There is good agreement between NGR from physical properties measurements on cores and the gamma ray log from the spectral tool (Hostile Environment Natural Gamma Ray Sonde; HNGS) at 100–210 and 450–800 m WMSF (Figure F45). Although it is difficult to match specific features given the incomplete core recovery, similar trends are observed and a few distinct features can be correlated (for example, an interval of increasing gamma ray between 720 and 730 m WMSF). Within the collapsed interval, gamma ray values from downhole logs are lower than those measured on cores, although there is an indication that similar features can be observed. This offset may be due to a number of factors, including (1) an inadequate borehole size correction to the gamma ray log while the HLDS caliper was closed in this interval, (2) potentially high fluid content of the formation in the collapsed interval, leading to dilution of the gamma ray signal from the in situ sediments,

and/or (3) a gamma ray signature that reflects a mix of sources from in situ sediments and from fallen material with lower gamma radiation from shallower sections of the hole. Total gamma ray logs from the Enhanced Digital Telemetry Cartridge (EDTC; see **Downhole measurements** in the Expedition 359 methods chapter [Betzler et al, 2017a]) show good agreement with NGR data even in the collapsed interval; outside this interval, gamma ray values from the EDTC and HNGS overlay very closely. The EDTC is not a spectral tool like the HNGS but instead includes a sodium iodide scintillation detector that measures total gamma ray emissions and is more robust even in poor hole conditions.

In the depth interval through which the caliper was closed (275–420 m WMSF), the density log underestimates formation properties as a result of poor/no contact between the HLDS tool and the borehole wall. Outside that interval, there are sections of good agreement between the density log and density data from MAD measurements on cores (e.g., 200–220 and 640–810 m WMSF). There are also sections through which the HLDS tool made good contact with the borehole wall (e.g., 530–640 m WMSF) and the density log decreases but the MAD values indicate higher densities than the logging data. This difference may reflect a bias in core recovery and therefore MAD measurements, whereby only hard formation is recovered and softer lithologies are missing from the recovered section. The continuous density log records data through both the harder (recovered) and softer (perhaps unrecovered) materials, resulting in lower average density values.

The porosity log estimates higher porosity values than MAD measurements through most of the logged interval, even in sections where the porosity tool made good contact with the borehole wall (Figure **F45**). In part, this difference may be due to the porosity tool itself, which is not designed for formations with porosity >60%. If core recovery at Site U1468 is biased toward harder, likely less porous formation (see above), the true porosity of these sediments may be higher than the ~50% mean porosity value estimated from MAD data and thus beyond the accuracy rating of the porosity logging tool.

Magnetic susceptibility from downhole logging shows similar characteristics to the electrical resistivity log, which is robust even in poor to moderate borehole conditions, indicating that this deep-reading measurement may reflect true changes in formation properties.

Logging units

Four logging units were identified on the basis of characteristic features and trends, primarily in gamma ray and electrical resistivity data. Logging Unit 2 was divided into two subunits on the basis of a change in gamma ray character. These units are identified in Figures **F45** and **F46**.

Logging Unit 1 (Base of drill pipe to 201 m WMSF)

Logging Unit 1 is characterized by relatively low gamma ray and resistivity values, both of which exhibit low- to moderate-amplitude variability. Gamma ray data fluctuate around a mean value of 16 American Petroleum Institute gamma radiation units (gAPI), with two intervals of locally increased gamma radiation centered at 160 and 170 m WMSF. As at previous logged Sites U1466 and U1467, spectral gamma ray data indicate that changes in uranium dominate the total gamma ray signal, compared to the minor contributions of thorium and potassium in this environment (Figure **F46**). Resistivity increases slightly with depth in this unit, with an average value of 1.41 Ωm. Two prominent peaks in resistivity, density, porosity, and magnetic susceptibility at the base of this unit are likely related to a transition in formation texture and the appearance of several lithified and/or indurated packstone layers between 190 and 200 m WMSF at the top of lithostratigraphic Unit III (see **Lithostratigraphy**).

Logging Unit 2 (201–490 m WMSF)

Logging Unit 2 is distinguished from the overlying unit on the basis of a change in the character of the resistivity log and is separated into two subunits. Within Subunit 2A (201–451 m WMSF), the resistivity log exhibits alternations between lower and higher resistivity (from 1.12 to 2.94 Ωm) over intervals of meters to tens of meters. Boundaries between intervals are sharp in some cases (e.g., at 275, 372, and 412 m WMSF) and gradual in others (e.g., at 260–274, 355–361, and 384–391 m WMSF). Intervals of higher resistivity generally correspond to intervals of increased gamma radiation, suggesting that the more resistive layers may have higher organic content and/or lower carbonate content. This is generally consistent with carbonate/total organic carbon data from geochemical measurements through this depth interval (see **Geochemistry**) (Figure **F32**), although the resolution of geochemical data is not sufficient to correlate with individual high-resistivity/high–gamma ray intervals. The gamma ray profile in this subunit reflects similar amplitude variability and a slightly higher mean value (17 gAPI) than that found in overlying Unit 1.

Logging Subunit 2B (451–490 m WMSF) is marked by a change in the character of the gamma ray log, with multiple sharp peaks of elevated gamma ray (up to 43 gAPI). The resistivity log does not change in character compared to Subunit 2A, but values are locally elevated.

Logging Unit 3 (490–720 m WMSF)

Gamma ray values decrease at the logging Unit 2/3 boundary, although the log character is similar to that of Unit 1 and the majority of Unit 2. The profile ranges in amplitude from low- to moderate-amplitude variability, with values ranging from 16 to 54 gAPI and an increase in amplitude with depth in the unit. Features with elevated gamma ray are observed (e.g., at ~645 and 688–690 m WMSF) that may be linked with subtle changes in resistivity. Resistivity log character is similar to that of Unit 1, with low-amplitude variability around a mean value of 1.64 Ωm.

Logging Unit 4 (720–835 m WMSF; base of logged interval)

The top of logging Unit 4 is defined by a change in resistivity character from low- to moderate-amplitude variability with an increase in the resistivity range (1.33–3.18 Ωm) and a lower mean resistivity value (1.59 Ωm) compared to overlying Unit 3. At the top of Unit 4, gamma ray values increase from 720 to 731 m WMSF and then decrease to a relatively low baseline value (~9 gAPI). The gamma ray profile in this unit exhibits the greatest variability (from 8 to 86 gAPI) compared to other units. These trends in the gamma ray log are also reflected in the resistivity log, although changes in resistivity occur over a smaller range of values.

Downhole logs and lithology

Downhole logs from Hole U1468B reflect changes in sediment properties, particularly organic content and degree of lithification, in the drift sediments and underlying facies. The shallowest 192 m of sediments at Site U1468, comprising lithostratigraphic Units I and II, consist of layers and packages of sediments that range in texture from wackestone to rudstone, sometimes finely interlayered

Figure F46. NGR logs, Hole U1468B. HSGR = standard (total) gamma ray, HCGR = computed (U-free) gamma ray.

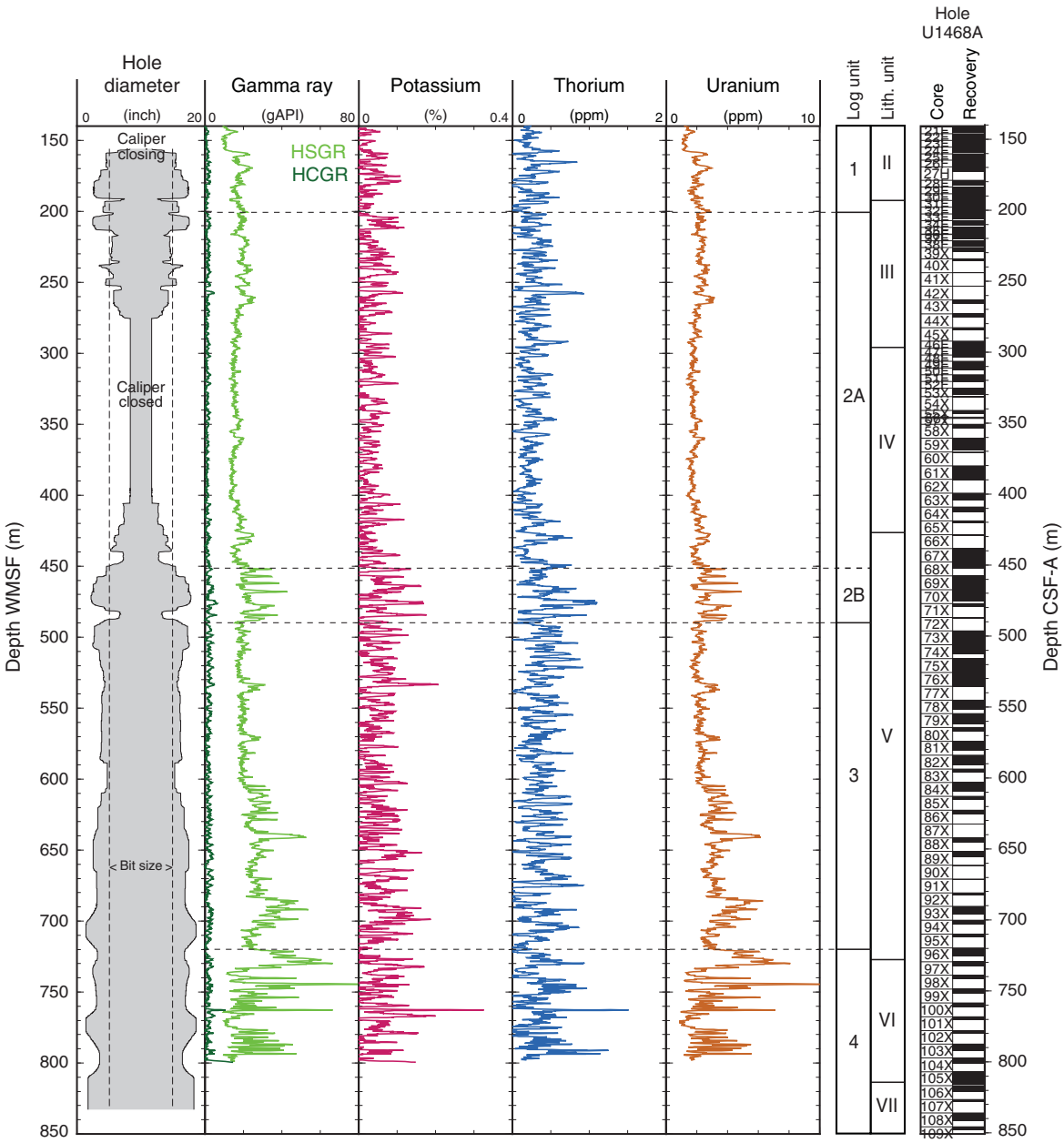

(see **Lithostratigraphy**). These layers vary from unlithified to highly lithified over the scale of submeters to meters. As observed at previously cored and logged sites (see **Downhole measurements** in the Site U1466 chapter [Betzler et al, 2017d]), partially lithified and lithified intervals have higher gamma radiation relative to the unlithified layers that separate them, reflecting higher organic content. Physical properties measurements on Hole U1468A cores can be correlated with Hole U1468B downhole logs to provide a continuous record of the more lithified intervals (Figure **F47**) with a slight (<2 m) depth offset between the two data sets.

Logging Unit 2 (Figures **F45**, **F46**) is dominated by alternating layers of more and less resistive material that reflects the increase in partially lithified and lithified layers observed in lithostratigraphic Units III and IV (see **Lithostratigraphy**). A high-resistivity feature at ~345 m WMSF most likely corresponds to a chert layer between 345 and 346 m DSF, and other high-resistivity features in this unit are likely related to chert layers in Hole U1468A. Intervals of higher amplitude gamma ray variations and corresponding resistivity variations within logging Subunit 2B (450–490 m WMSF) capture the alternation of submeter- to multiple meter–scale intervals of alternating light and dark bands in Cores 359-U1468A-68X through 71X (Figure **F48**). This distinctive interval in the downhole logs corresponds to the upper section of lithostratigraphic Unit V, where dark bands are characterized by higher resistivity and gamma ray (reflecting increased organic material) and lower color reflectance (L*).

The transition from logging Unit 3 to Unit 4 reflects a change in the gamma ray profile, primarily due to higher uranium content in Unit 4. This boundary is equivalent to the lithostratigraphic Unit V/VI boundary and the appearance of alternating black and white

Figure F47. Correction of downhole natural gamma ray for attenuation through the BHA using a multiplier of 5, Site U1468. Correlation of features in Hole U1468A cores to equivalent features in Hole U1468B log data is shown. HSGR = standard (total) gamma ray.

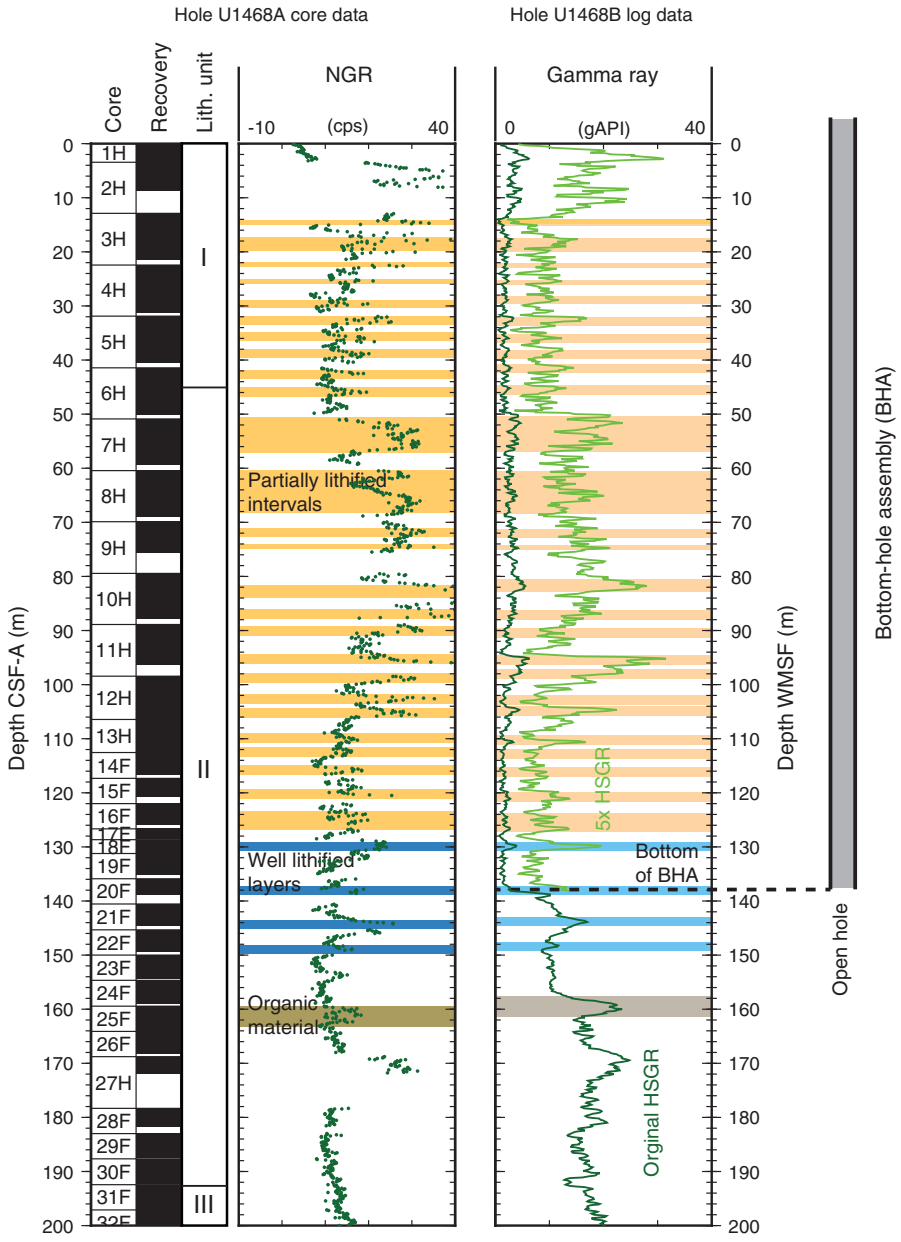

intervals of sediments in lithostratigraphic Unit VI. Black intervals with little to no bioturbation correspond to features with high gamma ray (high uranium) in the downhole logs, consistent with the interpretation of black layers as indicators of organic-rich layers deposited during periods of higher productivity in a more reducing depositional environment. A total of 41 black and white couplets were observed in the recovered core between 728.6 and 815.9 mbsf (see **Lithostratigraphy**). Intervals with high gamma ray in downhole logs in this unit appear as submeter- to meter-scale features; the vertical resolution of the gamma ray log (20–30 cm) may not be sufficient to completely resolve each interval observed in cores (1–25 cm thick). However, given the core recovery rate (~42%) and the appearance of high gamma ray features throughout the unrecovered intervals, it is likely that there are additional high-productivity periods that can be identified in this unit.

Figure F48. Correlation of physical properties from downhole logs in Hole U1468B and core measurements in Hole U1468A, highlighting alternating dark (higher organic content) and light (lower organic content) layers in core photos. Light blue bands = dark layers in cores and the corresponding low color reflectance, gamma ray, and resistivity. Dark blue bands = intervals where additional layers with high organic content may be present within gaps in core recovery. Resistivity log = true resistivity, modeled from five resistivity curves with different depths of investigation. NGR and L* were measured on cores.

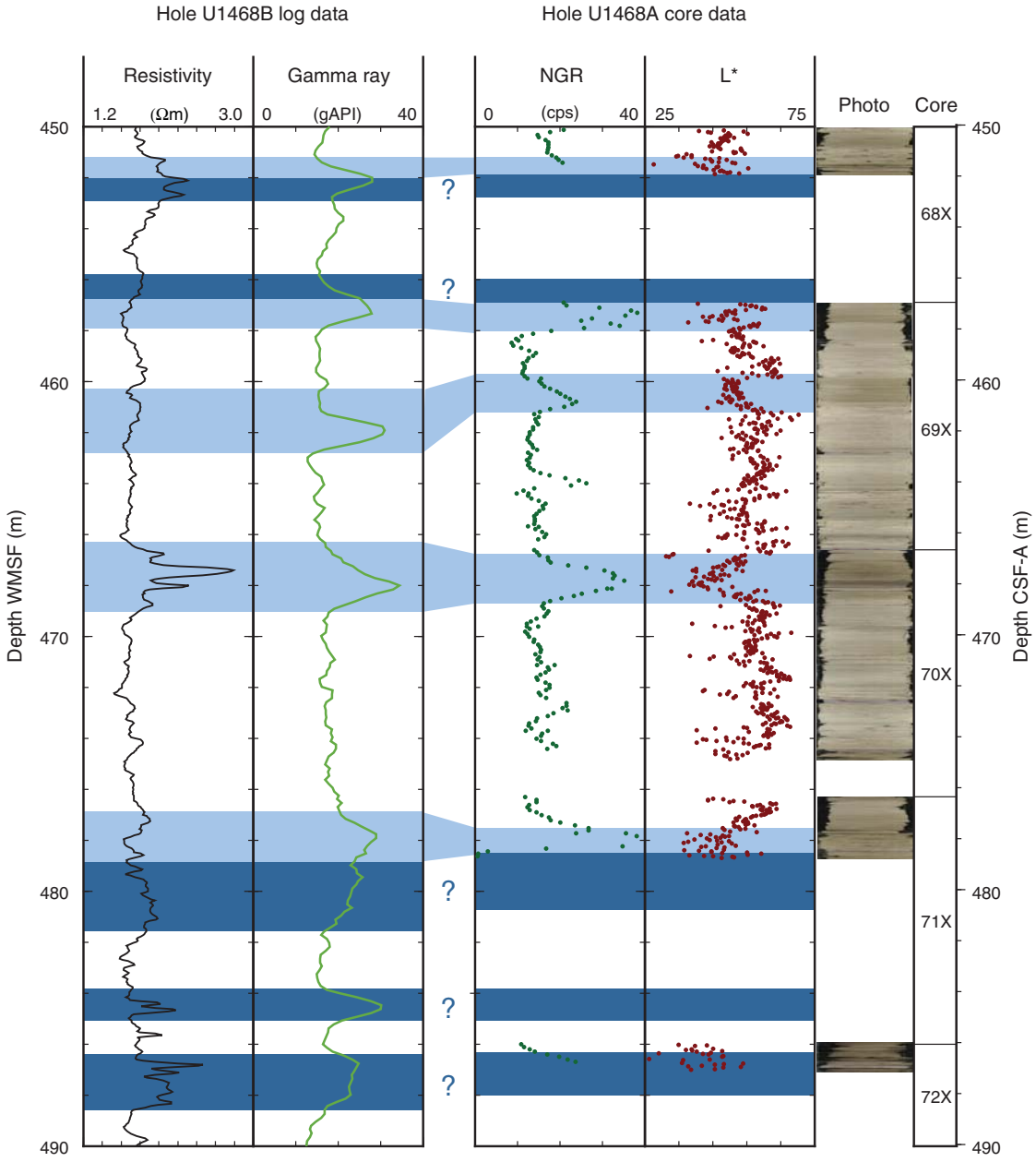

Seismic stratigraphy

Site U1468 is located northeast of the Goidhoo atoll in the Kardiva Channel, 4.9 km east of Site U1466 (Figure **F2**). Together with Sites U1465 and U1466, it represents the northern transect crossing the drowned Kardiva platform from the platform top into its distal foresets and the overlying postdrowning drift sequences onlapping the platform margin and slope. Site U1468 was drilled to the Oligocene/Miocene boundary and penetrated all overlying distal foresets of the platform sequences including their change in depositional style from aggradation to progradation (Figure **F49**; Table **T12**). The site is positioned at the depocenter of the oldest drift sequences (DS1 and DS2) mapped by Lüdmann et al. (2013). The younger sequences (DS3–DS8) are either truncated or condensed, but this is not clearly detectable because it is below the resolution of the seismic data.

Time-depth conversion

Because logging operations at Site U1468 had to be terminated after the first logging run, no vertical seismic profile or sonic log was acquired. The time-depth conversion therefore relies on fixed points provided by the cored formation. The target depth was the late Oligocene below a chalky interval with dark organic-rich layers encountered at the base of Hole U1466B (see **Lithostratigraphy** in

Figure F49. Seismic section of the distal part of the drowned Kardiva platform and onlap and burial by drift sequences, Site U1468. O/M = horizon interpreted by Belopolsky and Droxler (2004) as the Oligocene/Miocene boundary. DS1 (dark blue) marks the base of the current-controlled sedimentation in the Inner Sea.

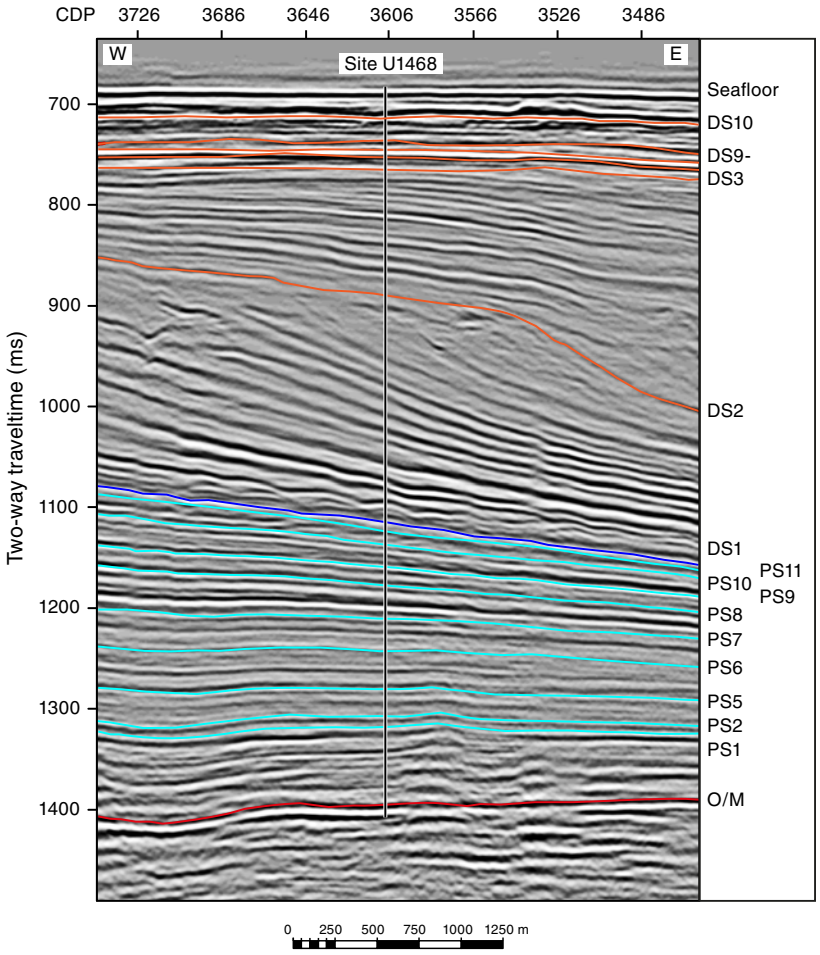

Table T12. Drift sequence and platform sequence boundaries and O/M seismic horizon, Site U1468. **Download table in .csv format.**

Sequence (bottom)	TWT (ms)	Depth (mbsf)
DS10	28	22.5
DS9	54	43
DS8–DS4	67	55
DS3	80	65
DS2	205.5	195.2
DS1	431	450
PS11	439	460
PS10	452	472
PS9	475	506.5
PS8	492.5	531
PS7	524.5	576
PS6	558	622
PS5	595.5	682
PS2	622	720
PS1	633	738
O/M	710.5	854.5

the Site U1466 chapter [Betzler et al, 2017d]) and located seismically above a high-amplitude reflection mapped by Betzler et al. (2013b) as the Oligocene/Miocene boundary (O/M reflection). At Site U1468, this reflection corresponds to the top of shallow-water carbonates recovered in Cores 359-U1468A-110X and 111X (see **Lithostratigraphy**). Deposits are dense and lithified (see **Physical properties**). Therefore, the impedance contrast between the hard limestone and the overlying wackestone-floatstone alternations produces the high-amplitude reflection seen on the seismic section at 1398 ms TWT (854.5 mbsf). As an additional control point, the top of another dense interval was used at 1199.56 ms TWT (540 mbsf). These anchor points were used to improve our velocity model for Site U1468 (Figure **F50**) and construct the time-depth conversion (Figure **F51**).

Seismic facies and geometries

The penetrated seismic section at Site U1468 displays four main seismic facies. At the bottom are near-horizontal seismic reflections with a distinct high-amplitude reflection at the base (O/M reflection). The Oligocene platform succession is overlain by a package of slightly inclined reflections of variable amplitudes. This interval between reflections O/M and platform sequence (PS) PS1 corresponds to the nannofossil chalk package with intercalations of organic-rich layers. The penetrated distal slope facies of early to middle Miocene prograding sequences PS1–PS11 are characterized by inclined, continuous medium- to low-amplitude reflections that conjugate basinward. Sections of alternating amplitude intensities

Figure F50. Correlation of seismic, core, and log data, Site U1468. Seismic line 65 (M74) is shown with the position of platform and drift sequences. HSGR = standard total natural gamma ray, RHOM = bulk density. Interval velocity = model for time-depth conversion.

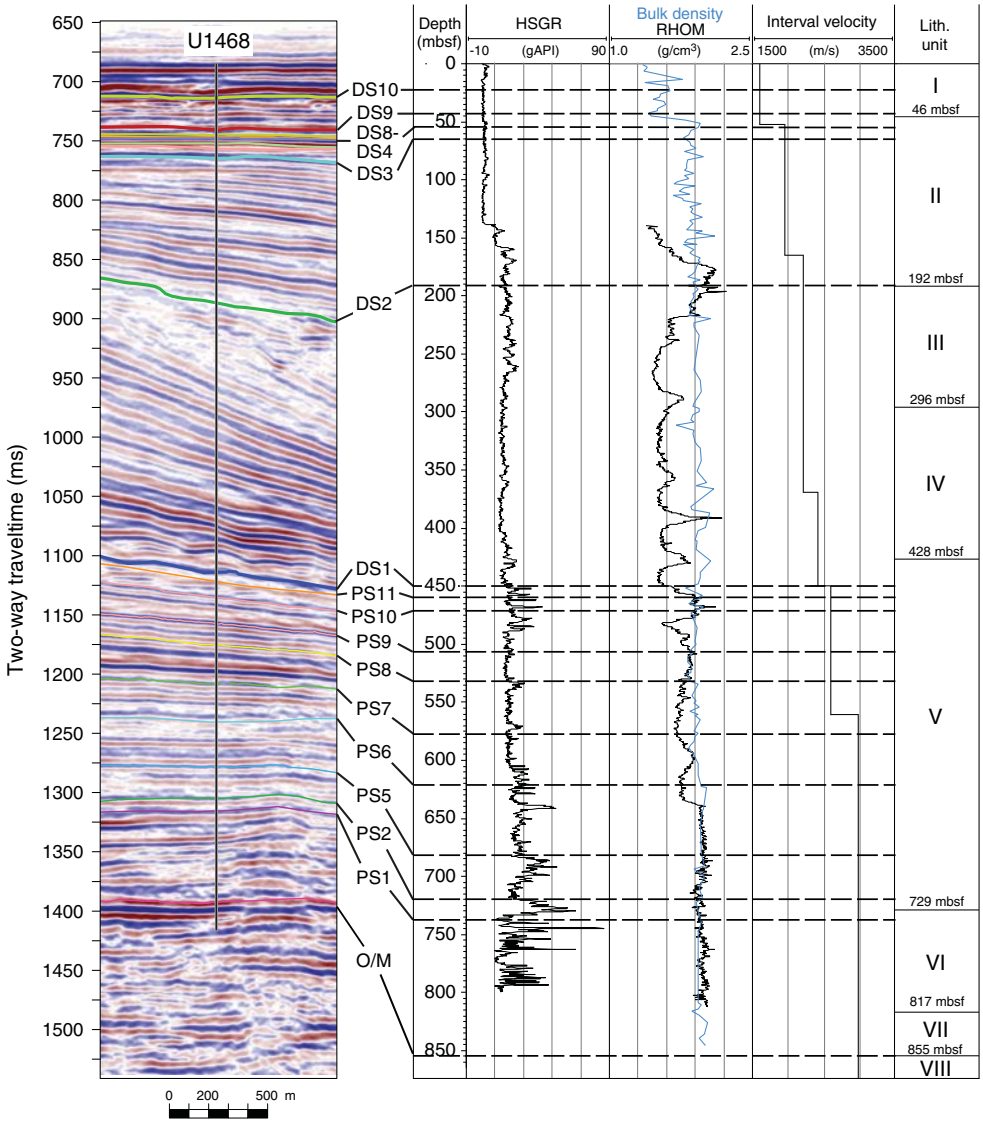

are likely caused by pulses of deposition and intermittent slow sedimentation and associated diagenesis (Anselmetti et al., 2000; Malone et al., 2001). The onset of the drift sequences lies at 434 mbsf and is indicated by wavy high-amplitude reflections. The waves have wavelengths of 250–450 m and a height of approximately 5 m. The waves migrate upslope and could either represent cyclic steps located at the break of slope or have formed as a result of an intensification of margin-parallel bottom currents (Lüdmann et al., 2013). They occur only at the base of DS1. Generally, DS1 has large mounded geometry with high-amplitude parallel reflections that conjugate basinward. Their inclination slightly increases from bottom to top, and in the upper third they have an overall sigmoidal shape.

DS2 unconformably overlies DS1, with reflections onlapping at the sequence boundary. Its facies is similar to DS1 but exhibits a higher reflection frequency that implies thinner bedding compared to DS1. At the top of DS2, reflections become nearly horizontal, marking the apex of the drift mound. At Site U1468, DS3–DS9 merge into two horizontal reflections separated by approximately 20 m. The position of the sequence boundaries in between is below the resolution of the seismic data. The uppermost drift sequences (DS9 and DS10) show undulating high-amplitude reflections.

Core-seismic correlation

The top of the Oligocene shallow-water carbonate platform (lithostratigraphic Unit VIII) is a lithified bioclastic floatstone in Core 359-U1468A-111X, which in the seismic section correlates to the O/M reflection defined by Belopolsky and Droxler (2004) as the Oligocene/Miocene boundary. Biostratigraphic analysis of calcareous nannoplankton and planktonic foraminifers (see **Biostratigraphy**), however, indicates that the Oligocene/Miocene boundary is located farther upsection between 769.74 and 779.36 mbsf (i.e., between the O/M horizon and PS1).

The 100 m thick Unit VI deposits consisting of white calcareous nannofossil chalk with intercalations of black organic-rich intervals are seismically marked by lower amplitude reflections. The near-

Figure F51. Time-depth conversion, Site U1468.

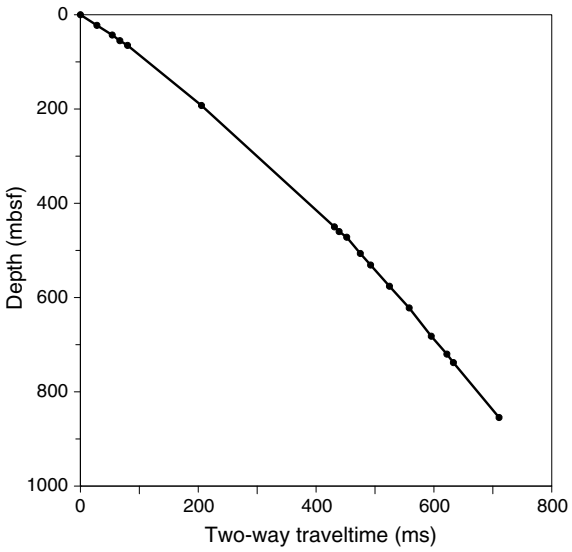

horizontal low-amplitude reflections above are the distal bottomsets of Kardiva platform sequences PS1–PS11 and correspond to lithostratigraphic Unit V, which is a planktonic foraminiferal wackestone to packstone succession with meter-thick alternations of darker and lighter bioturbated layers. These distal bottomsets lie at 427.7–724.56 mbsf (Sections 359-U1468A-66X-1 through 96X-CC). The age of these prograding sequences is middle Burdigalian to Langhian, approximately 21–12.7 Ma. These deposits show generally lower amplitudes than the underlying platform and chalk strata. With the turnaround from aggradation to progradation in PS7, the distal bottomsets display higher amplitudes at the top of each prograding sequence.

A high-amplitude reflection separates the platform and drift sequences. The lower part of DS1 corresponds to lithostratigraphic Unit IV, which consists of lithified bioclastic packstone to wackestone. DS1 reveals a characteristic high-amplitude facies that reflects the increase in grain size in the distal bottomset in lithostratigraphic Unit V and the occurrence of chert nodules. The upper third of DS1 is partially lithified bioclastic wackestone to packstone (lithostratigraphic Unit III) imaged by a decrease of the amplitude contrasts of the reflections. DS2 consists of high-amplitude slightly inclined seismic reflections and is lithologically composed of a series of unlithified to partially lithified coarsening-upward packages of large benthic foraminiferal grainstone to rudstone (Unit II) that continue into the base of DS9. DS9 and DS10 show high-amplitude reflections of high frequencies that coincide with alternating thin layers with different levels of lithification.

Log-seismic correlation

The gamma ray and bulk density logs are shown with the seismic section at Site U1468 in Figure **F50**. As a result of deteriorating hole conditions, the density log is of low quality above 440 mbsf. From bottom to top, gamma ray generally increases in intensity. Although individual peaks in the log do not, in most cases, match with sequence boundaries, the log characterizes the sequence stratigraphic evolution at this site. In particular, the different signatures of the sea level–controlled system and the current-controlled drift are clearly visible in the gamma ray log. In the bottomsets of the platform (PS1–PS11), the gamma ray log fluctuates around 60 gAPI, with breaks or changes coinciding with some sequence boundaries. With the onset of the drift (DS1), which is dated at approximately 12.8 Ma, the log shows low intensity and only minor fluctuations.

References

Anselmetti, F.S., Eberli, G.P., and Ding, Z.-D., 2000. From the Great Bahama Bank into the Straits of Florida: a margin architecture controlled by sea-level fluctuations and ocean currents. *Geological Society of America Bulletin,* 112(6):829–844. **http://dx.doi.org/10.1130/0016-7606(2000)112<0829:FTGBBI>2.3.CO;2**

Backman, J., Raffi, I., Rio, D., Fornaciari, E., and Pälike, H., 2012. Biozonation and biochronology of Miocene through Pleistocene calcareous nannofossils from low and middle latitudes. *Newsletters on Stratigraphy,* 45(3):221–244. **http://dx.doi.org/10.1127/0078-0421/2012/0022**

Belopolsky, A.V., and Droxler, A.W., 2004. Seismic expressions and interpretation of carbonate sequences: the Maldives platform, equatorial Indian Ocean. *AAPG Studies in Geology,* 49. **http://archives.datapages.com/data/specpubs/study49/images/st49.pdf**

Berggren, W.A., Kent, D.V., Swisher, C.C., III, and Aubry, M.-P., 1995. A revised Cenozoic geochronology and chronostratigraphy. *In* Berggren, W.A., Kent, D.V., Aubry, M.-P., and Hardenbol, J. (Eds.), *Geochronology, Time Scales and Global Stratigraphic Correlation.* Special Publication - SEPM (Society for Sedimentary Geology), 54:129–212. **http://dx.doi.org/10.2110/pec.95.04.0129**

Betzler, C., Eberli, G.P., Alvarez Zarikian, C.A., Alonso-García, M., Bialik, O.M., Blättler, C.L., Guo, J.A., Haffen, S., Horozal, S., Inoue, M., Jovane, L., Kroon, D., Lanci, L., Laya, J.C., Ling Hui Mee, A., Lüdmann, T., Nakakuni, M., Nath, B.N., Niino, K., Petruny, L.M., Pratiwi, S.D., Reijmer, J., Reolid, J., Slagle, A.L., Sloss, C.R., Su, X., Swart, P.K., Wright, J.D., Yao, Z., and Young, J.R., 2017a. Expedition 359 methods. *In* Betzler, C., Eberli, G.P., Alvarez Zarikian, C.A., and the Expedition 359 Scientists, *Maldives Monsoon and Sea Level.* Proceedings of the International Ocean Discovery Program, 359: College Station, TX (International Ocean Discovery Program). **http://dx.doi.org/10.14379/iodp.proc.359.102.2017**

Betzler, C., Eberli, G.P., Alvarez Zarikian, C.A., Alonso-García, M., Bialik, O.M., Blättler, C.L., Guo, J.A., Haffen, S., Horozal, S., Inoue, M., Jovane, L., Kroon, D., Lanci, L., Laya, J.C., Ling Hui Mee, A., Lüdmann, T., Nakakuni, M., Nath, B.N., Niino, K., Petruny, L.M., Pratiwi, S.D., Reijmer, J., Reolid, J., Slagle, A.L., Sloss, C.R., Su, X., Swart, P.K., Wright, J.D., Yao, Z., and Young, J.R., 2017b. Expedition 359 summary. *In* Betzler, C., Eberli, G.P., Alvarez Zarikian, C.A., and the Expedition 359 Scientists, *Maldives Monsoon and Sea Level.* Proceedings of the International Ocean Discovery Program, 359: College Station, TX (International Ocean Discovery Program). **http://dx.doi.org/10.14379/iodp.proc.359.101.2017**

Betzler, C., Eberli, G.P., Alvarez Zarikian, C.A., Alonso-García, M., Bialik, O.M., Blättler, C.L., Guo, J.A., Haffen, S., Horozal, S., Inoue, M., Jovane, L., Kroon, D., Lanci, L., Laya, J.C., Ling Hui Mee, A., Lüdmann, T., Nakakuni, M., Nath, B.N., Niino, K., Petruny, L.M., Pratiwi, S.D., Reijmer, J.J.G., Reolid, J., Slagle, A.L., Sloss, C.R., Su, X., Swart, P.K., Wright, J.D., Yao, Z., and Young, J.R., 2017c. Site U1465. *In* Betzler, C., Eberli, G.P., Alvarez Zarikian, C.A., and the Expedition 359 Scientists, *Maldives Monsoon and Sea Level.* Proceedings of the International Ocean Discovery Program, 359: College Station, TX (International Ocean Discovery Program). **http://dx.doi.org/10.14379/iodp.proc.359.103.2017**

Betzler, C., Eberli, G.P., Alvarez Zarikian, C.A., Alonso-García, M., Bialik, O.M., Blättler, C.L., Guo, J.A., Haffen, S., Horozal, S., Inoue, M., Jovane, L., Kroon, D., Lanci, L., Laya, J.C., Ling Hui Mee, A., Lüdmann, T., Nakakuni, M., Nath, B.N., Niino, K., Petruny, L.M., Pratiwi, S.D., Reijmer, J., Reolid, J., Slagle, A.L., Sloss, C.R., Su, X., Swart, P.K., Wright, J.D., Yao, Z., and Young, J.R., 2017d. Site U1466. *In* Betzler, C., Eberli, G.P., Alvarez Zarikian, C.A., and the Expedition 359 Scientists, *Maldives Monsoon and Sea Level.* Proceedings of the International Ocean Discovery Program, 359: College Station, TX (International Ocean Discovery Program). **http://dx.doi.org/10.14379/iodp.proc.359.104.2017**

Betzler, C., Eberli, G.P., Alvarez Zarikian, C.A., Alonso-García, M., Bialik, O.M., Blättler, C.L., Guo, J.A., Haffen, S., Horozal, S., Inoue, M., Jovane, L., Kroon, D., Lanci, L., Laya, J.C., Ling Hui Mee, A., Lüdmann, T., Nakakuni, M., Nath, B.N., Niino, K., Petruny, L.M., Pratiwi, S.D., Reijmer, J.J.G., Reolid, J., Slagle, A.L., Sloss, C.R., Su, X., Swart, P.K., Wright, J.D., Yao, Z., and Young, J.R., 2017e. Site U1467. *In* Betzler, C., Eberli, G.P., Alvarez Zarikian, C.A., and the Expedition 359 Scientists, *Maldives Monsoon and Sea Level.* Proceedings of the International Ocean Discovery Program, 359: College Station, TX (International Ocean Discovery Program). **http://dx.doi.org/10.14379/iodp.proc.359.105.2017**

Betzler, C., Fürstenau, J., Lüdmann, T., Hübscher, C., Lindhorst, S., Paul, A., Reijmer, J.J.G., and Droxler, A.W., 2013a. Sea-level and ocean-current control on carbonate-platform growth, Maldives, Indian Ocean. *Basin Research*, 25(2):172–196. **http://dx.doi.org/10.1111/j.1365-2117.2012.00554.x**

Betzler, C., Hübscher, C., Lindhorst, S., Reijmer, J.J.G., Römer, M., Droxler, A.W., Fürstenau, J., and Lüdmann, T., 2009. Monsoon-induced partial carbonate platform drowning (Maldives, Indian Ocean). *Geology,* 37(10):867–870. **http://dx.doi.org/10.1130/G25702A.1**

Betzler, C., Lindhorst, S., Lüdmann, T., Weiss, B., Wunsch, M., and Braga, J.C., 2015. The leaking bucket of a Maldives atoll: implications for the understanding of carbonate platform drowning. *Marine Geology,* 366:16–33. **http://dx.doi.org/10.1016/j.margeo.2015.04.009**

Betzler, C., Lüdmann, T., Hübscher, C., and Fürstenau, J., 2013b. Current and sea-level signals in periplatform ooze (Neogene, Maldives, Indian Ocean). *Sedimentary Geology*, 290:126–137. **http://dx.doi.org/10.1016/j.sedgeo.2013.03.011**

Boersma, A., and Mikkelsen, N., 1990. Miocene-age primary productivity episodes and oxygen minima in the central equatorial Indian Ocean. *In* Duncan, R.A., Backman, J., Peterson, L.C., et al., *Proceedings of the Ocean Drilling Program, Scientific Results,* 115: College Station, TX (Ocean Drilling Program), 589–609. **http://dx.doi.org/10.2973/odp.proc.sr.115.162.1990**

Dickens, G.R., and Owen, R.M., 1994. Late Miocene–early Pliocene manganese redirection in the central Indian Ocean: expansion of the intermediate water oxygen minimum zone. *Paleoceanography,* 9(1):169–181. **http://dx.doi.org/10.1029/93PA02699**

Douglas, R., and Heitman, H., 1979. Slope and basin benthic foraminifera of the California Borderland. *In* Doyle, L., and Pilkey, O. (Eds.), *Geology of the Continental Slopes.* Special Publication - Society of Economic Paleontologists and Mineralogists, 27:231–246. **http://sp.sepmonline.org/content/sepspgeo/1/SEC17.abstract**

Fisher, R.A., 1953. Dispersion on a sphere. *Proceedings of the Royal Society of London, Series A,* 217:295–305.

Fornaciari, E., and Agnini, C., 2009. Taxonomic note: *Sphenolithus pseudoheteromorphus,* a new Miocene calcareous nannofossil species from the equatorial Indian Ocean. *Journal of Nannoplankton Research,* 30(2):97–101. **http://ina.tmsoc.org/JNR/online/30/Fornaciari & Agnini 2009 JNR 30-2.pdf**

Fornaciari, E., Raffi, I., Rio, D., Villa, G., Backman, J., and Olafsson, G., 1990. Quantitative distribution patterns of Oligocene and Miocene calcareous nannofossils from the western equatorial Indian Ocean. *In* Duncan, R.A., Backman, J., Peterson, L.C., et al., *Proceedings of the Ocean Drilling Program, Scientific Results,* 115: College Station, TX (Ocean Drilling Program), 237–254. **http://dx.doi.org/10.2973/odp.proc.sr.115.153.1990**

Gradstein, F.M., Ogg, J.G., Schmitz, M.D., and Ogg, G.M. (Eds.), 2012. *The Geological Time Scale 2012:* Amsterdam (Elsevier).

Hilgen, F.J., Lourens, L.J., and Van Dam, J.A., 2012. The Neogene period. With contributions by A.G. Beu, A.F. Boyes, R.A. Cooper, W. Krijgsman, J.G. Ogg, W.E. Piller, and D.S. Wilson. *In* Gradstein, F.M., Ogg, J.G., Schmitz, M.D., and Ogg, G.M. (Eds.), *The Geologic Time Scale:* Oxford, United Kingdom (Elsevier), 923–978. **http://dx.doi.org/10.1016/B978-0-444-59425-9.00029-9**

Lourens, L., Hilgen, F., Shackleton, N.J., Laskar, J., and Wilson, D., 2004. The Neogene period. *In* Gradstein, F.M., Ogg, J.G., and Smith, A. (Eds.), *A Geologic Time Scale 2004:* Cambridge, United Kingdom (Cambridge University Press), 409–440. **http://dx.doi.org/10.1017/CBO9780511536045.022**

Lüdmann, T., Kalvelage, C., Betzler, C., Fürstenau, J., and Hübscher, C., 2013. The Maldives, a giant isolated carbonate platform dominated by bottom currents. *Marine and Petroleum Geology*, 43:326–340. **http://dx.doi.org/10.1016/j.marpetgeo.2013.01.004**

Malone, M.J., Slowey, N.C., and Henderson, G.M., 2001. Early diagenesis of shallow-water periplatform carbonate sediments, leeward margin, Great Bahama Bank (Ocean Drilling Program Leg 166) *Geological Society of America Bulletin,* 113(7):881–894. **http://dx.doi.org/10.1130/0016-7606(2001)113<0881:EDOSWP>2.0.CO;2**

Poag, C.W., and Low, D., 1985. Environmental trends among Neogene benthic foraminifers at Deep Sea Drilling Project Site 548, Irish continental margin. *In* de Graciansky, P.C., Poag, C.W., et al., *Initial Reports of the Deep Sea Drilling Project,* 80: Washington, DC (U.S. Government Printing Office), 489–503. **http://dx.doi.org/10.2973/dsdp.proc.80.112.1985**

Raffi, I., Backman, J., Fornaciari, E., Pälike, H., Rio, D., Lourens, L., and Hilgen, F., 2006. A review of calcareous nannofossil astrobiochronology encompassing the past 25 million years. *Quaternary Science Reviews,* 25(23–24):3113–3137. **http://dx.doi.org/10.1016/j.quascirev.2006.07.007**

Rio, D., Fornaciari, E., and Raffi, I., 1990. Late Oligocene through early Pleistocene calcareous nannofossils from western equatorial Indian Ocean (Leg 115). *In* Duncan, R.A., Backman, J., Peterson, L.C., et al., *Proceedings of the Ocean Drilling Program, Scientific Results,* 115: College Station, TX (Ocean Drilling Program), 175–235. **http://dx.doi.org/10.2973/odp.proc.sr.115.152.1990**

Renema, W., and Troelstra, S.R., 2001. Larger foraminifera distribution on a mesotrophic carbonate shelf in SW Sulawesi (Indonesia). *Palaeogeography, Palaeoclimatology, Palaeoecology,* 175(1–4):125–146. **http://dx.doi.org/10.1016/S0031-0182(01)00389-3**

Schrag, D.P., and DePaolo, D.J., 1993. Determination of $\delta^{18}O$ of seawater in the deep ocean during the Last Glacial Maximum. *Paleoceanography,* 8(1):1–6. **http://dx.doi.org/10.1029/92PA02796**

Sola, F., Braga, J.C., and Aguirre, J., 2013. Hooked and tubular coralline algae indicate seagrass beds associated to Mediterranean Messinian reefs (Poniente Basin, Almería, SE Spain). *Palaeogeography, Palaeoclimatology, Palaeoecology,* 374:218–229. **http://dx.doi.org/10.1016/j.palaeo.2013.01.020**

Thompson, P.R., Bé, A.W.H., Duplessy, J.-C., and Shackleton, N.J., 1979. Disappearance of pink-pigmented *Globigerinoides ruber* at 120,000 yr BP in the Indian and Pacific Oceans. *Nature,* 280(5723):554–558. **http://dx.doi.org/10.1038/280554a0**

Torsvik T.H., Van der Voo, R., Preeden, U., Mac Niocaill, C., Steinberger, B., Doubrovine, P.V., van Hinsbergen, D.J.J., Domeier, M., Gaina, C., Tohver, E., Meert, J.G., McCausland, P.J.A., and Cocks, L.R.M., 2012. Phanerozoic polar wander, palaeogeography and dynamics. *Earth-Science Reviews,* 114(3–4):325–368. **http://dx.doi.org/10.1016/j.earscirev.2012.06.007**

Young, J.R., 1998. Neogene. *In* Bown, P.R. (Ed.), *Calcareous Nannofossil Biostratigraphy:* Dordrecht, The Netherlands (Kluwer Academic Publishing), 225–265.